UMI Number: 9988209

UMI Microform 9988209

Bell & Howell Information and Learning Company
300 North Zeeb Road
P.O. Box 1346
Ann Arbor, MI 48106-1346

NUMERICAL INVESTIGATION OF THE PHYSICAL VAPOR DEPOSITION OF TITANIUM

A Dissertation
Presented to the Faculty of the Graduate School
of Cornell University
in Partial Fulfillment of the Requirements for the Degree of
Doctor of Philosophy

by
Jitendra Balakrishnan
January 2001

Biographical Sketch

Jitendra Balakrishnan was born in Bellampalli, India, and grew up in the southern, coastal city of Madras. He graduated from the Indian Institute of Technology in July 1995, with a Bachelors degree in Aerospace Engineering. His parents seemed more relieved than proud. He then crossed a big pond and started his Ph.D. in Mechanical Engineering at Cornell University, picking up a M.S. along the way. During his stay in warm and sunny Ithaca, he took some time off his busy schedule to meet his future wife and get married. His plans for the new millenium include research in fiber optics, and educating the average American about cricket and the real meaning of "football".

To Appa, Amma, Anant and Purnima,

for ... everything!

Acknowledgements

The work presented in this dissertation was funded by the Lawrence Livermore National Laboratories through Grant B336457. Computational resources were provided by the Cornell Theory Center and the Maui High Performance Computing Center.

As I write this to express my thanks, I know that there are many, many people who have left an impression on my life, and who may not find mention here. After all, I am supposed to keep this short. To every one of them who has touched my life, I would like to express my gratitude. I think I'll also use the clichéd, "you know who you are".

First, I'd like to thank my advisor, Iain Boyd, for making my Ph.D. a great experience. As far as advisors go, I got lucky. I'd also like to thank the other members of my committe, P.C.T. deBoer and Stephen Vavasis for all the help they have given me.

I would also like to thank Dave Braun and the other scientists at LLNL for providing the experimental data, useful discussions and an exposure to the world outside academia.

My stint had Cornell would have been shorter, but less enjoyable, if not for my loony officemates. Keith and Dan, you guys are largely responsible for the havoc I create with C, and for Angband... Doug, thanks for everything from Plasma Physics homework (ugh!) to our profound conversations. Bill, you were the balancing act in an otherwise crazy environment. And thanks Mike, for providing uncomplaining accomodation every time I visited Michigan.

The staff in Upson Hall are a wonderful group of people who have bailed me out of trouble innumerable times. I'd like to thank them for all their help - Karen, Sharon, Gail, Ginny, Brenda, Nanette, Judy, June, Polly, Laurie, Rick ... the list goes on.

Ithaca has given me many really good friends - Sujata, Sharon and Prashant, with whom I shared Cajun Fries and good times; Ravi, Nari, Mani, Subbu and Vatsa, with whom there was never a dull moment; Shami, the Talkies crew, Emia & Mike, Kate & Kraz, Rob & KeShil, and everyone else.

My family has always been a great source of support, love, direction, those-undefinable-thingys, etc., and I want to express my gratitude to them. To my parents-in-law and my grandparents, for being the great people they are. To my parents, for all they have given me, and for being really, really excited after my defence. Anant, you're the *bestest* brother in the whole world. And to my wife, Purnima -- I could say a lot, but don't want to get too sentimental here... :) And to the Powers That Cannot Be Thanked Enough, here's a feeble effort nevertheless.

Table of Contents

List of Tables

List of Figures

Chapter 1

Introduction

1.1 Overview of vapor deposition techniques

The needs of modern technology have led to rapid developments in materials processing techniques. The second half of the twentieth century saw the emergence of vapor phase manufacturing processes. While traditional techniques in materials processing involved solid and liquid phase manufacturing, the vapor phase processes offered a paradigm shift in this industry and contributed to the development of materials that solid and liquid phase manufacturing could not produce. These processes revolutionized the semiconductor industry with the next generation of electronic materials and have also enabled advances in aerospace technology.

The aerospace industry is developing Metal Matrix Composites (MMC) to meet the need for the next generation of aerospace materials. These composites consist of layers, matrices or other microstructural arrangements of different materials [6]. Common MMC's include alloys of titanium like $TiAl6V4$, $(Ti_2Al)_xNb_{(1-x)}$ and $Ti_xMo_{(1-x)}$ [90],[113],[119]. These materials are used in aircraft engine components, where they enable an increase in engine power and enhance aircraft performance. These composite materials also have high strength-to-weight ratios, thus offering an important advantage when used in aircraft structures. Such applications use materials like fiber reinforced composites, an example being SiC fibers coated with a titanium alloy. Vapor deposition has been the method of choice for the production of these MMC's. Another important application of advanced materials to aircraft engines is found in the development of Thermal Barrier Coatings (TBC) [92]. A ceramic layer of a material like TiN or TiC is vapor deposited on the turbine blades used in the post-combustion zone of an engine. This material provides an insulating layer to the turbine blade and reduces the temperature of the blade. In addition, TBC's protect the blade against oxidation from the hot, reactive gases in the engine, thus increasing the life of the engine. The microstructure of these applications is extremely important [85]. Vapor deposition processes provide the means to control the composition and microstructure of TBC's and MMC's, thus making them important materials processing tools in the aerospace industry.

Vapor deposition processes are used extensively in the semiconductor industry [56]. The manufacture of semiconductor devices often includes masking, etching and vapor deposition processes, which are combined to create features on a silicon chip. Vapor deposition techniques are used to deposit metal interconnection layers between semiconductor devices on a chip [134],[135],[136]. Vapor phase manufacturing also revolutionized the development of thin film transistors. These manufacturing techniques allowed the deposition of thin films of silicon on a substrate [105],[129],[130], which was not possible through older manufacturing processes. The kinetic energy of the adsorbed atoms and molecules plays an important role in improving the quality of the deposited layer in many applications, thus making vapor phase manufacturing attractive in these applications. Some vapor phase processing methods also offer non-line-of-sight deposition, which make these the method of choice in many applications. Vapor deposition processes are also used in many other industrial applications, like laser isotope separation [66] and the manufacture of wear resistant or optical coatings on a substrate.

Vapor deposition techniques have evolved considerably over time with the design requirements of new applications. The main classification of these methods separates them into physical vapor deposition (PVD) and chemical vapor deposition (CVD) techniques [41], with some amount of overlap between the two categories. CVD techniques often involve gas-phase reactions or reactions of molecules in the vapor at the substrate. Various ion implantation and plasma processing techniques have evolved primarily for use in semiconductor doping and manufacturing [86].

PVD techniques typically involve the creation of a vapor of an atomic or a molecular species, and its subsequent transport to a substrate. Adsorption and adatom diffusion at the substrate create the deposited layer. Early PVD methods like sputtering did not provide the material properties required in many advanced applications. PVD techniques like molecular beam epitaxy (MBE) [111] and vapor phase epitaxy (VPE) are used to grow thin films for semiconductor applications. In these methods, the material to be deposited impinges on a substrate in the form of a nearly collisionless beam of atoms and molecules. These processes are characterized by low growth rates, which are important for controlling the thin film deposition. Supersonic beams have also been used to facilitate thin film growth at low temperatures [48]. In this case, the adatoms use their high kinetic energies rather than thermal energy to overcome the activation barrier for their adsorption.

Electron beam evaporation techniques were developed to address many challenges in the applications of vapor deposition. The development of high vacuum environments led to a surge in electron beam evaporation technology, as the electrons require large mean free paths for the efficient heating of a material [118]. Higher chamber pressures lead to collisions between the electrons and vapor atoms, which dissipate the electron energy in the vapor rather than in the evaporating source. Low pressure environments thus help increase the efficiency of the electron beam heating. These techniques have gained in popularity due to the high deposition rates attained, the applicability of the technique to various metals, the efficiency of evaporation and the non-reactive nature of the evaporation [74]. This non-reactive nature is advantageous in the case of the evaporation of highly reactive metals like titanium and niobium, as the vapor source is unaffected by chemical reactions with the beam at the high temperatures of evaporation. The evaporation of multiple species enables the deposition of alloys on a substrate. The multi-species evaporation technique from a single crucible uses a source ingot composed of the alloy to be deposited [119]. However, the evaporation needs to be controlled carefully as different metals have different vapor pressures, and thus evaporate at different rates. The resulting vapor is often not uniform in the composition of the different species. Multiple beam sources have been used to evaporate different species from individual crucibles in some applications [60]. In this case, the deposition on the substrate is relatively uniform in species composition in regions where the vapor plumes from the different sources overlap.

One drawback of electron beam evaporation lies in the fact that the high vacuum conditions ensure only line-of-sight deposition. As collisions are not common in the expanding vapor, very few particles are scattered into shadow regions. This can lead to uneven surface coatings in some applications where the entire surface of the substrate is not exposed directly to the vapor source. Deposition in the trenches of semiconductor devices also require non-line-of-sight deposition to take place. This drawback has been overcome in certain variants of the evaporation process. The techniques of jet vapor deposition [68] and directed vapor deposition [67] use a carrier gas to transport the evaporating species from the source to the substrate, and have proved effective in obtaining non-line-of-sight coatings. The number density distribution of the evaporating vapor has been described in literature by a cosine distribution [43],[44],[88]:

$$N(\theta) = N_0 \cos^n \theta \tag{1.1}$$

where $N(\theta)$ is the number density in a direction θ degrees from the normal to the evaporating surface, N_0 is the number density along this normal direction and n is an exponent which has been reported to have a value of 2,3,4 or more. However, deviation from the cosine law is common due to the complexity of the problem. Electron beam scanning patterns rarely create point sources that produce these perfect cosine distributions of number density. The pressure in the chamber has been reported to affect this distribution [57]. Sometimes, collisions in the evaporating vapor create a virtual source which causes a deviation from the cosine distribution.

This study is part of an effort in the scientific community to understand the process of electron beam evaporation, and to add to the development of this process. The next section explores the motivation behind this study, as well as the specific objectives pursued in this work.

1.2 Motivation

Electron beam evaporation systems have been studied in the past by the scientific community through experimental, theoretical and computational efforts. Different methods have been used to model this process numerically. Continuum fluid dynamics using the Navier-Stokes equation has been applied to expansions in low density flows, but this approach has a drawback in the highly rarefied flow regimes found in EB-PVD systems. In high vacuum conditions, atoms have large mean free paths, which are on the order of the characteristic length of the system. Thus, the gradients in the Navier-Stokes equation break down at these low pressures, and a solution through this method becomes difficult. Direct simulations at the molecular level do not have this limitation and have been applied to the vapor deposition problem. The Direct Simulation Monte Carlo method has been used extensively to model various transition flows, and various simulations of electron beam evaporation systems have been reported in the literature [62],[63],[98],[100].

Though earlier modeling efforts have provided a good insight into the evaporation process, they fall short of capturing some physical effects that prove important in the flow. Experiments by Asano et al [5],[124] show that the mean atomic velocities in the electron beam evaporation of uranium, titanium and copper exceed the maximum flow speed of the gas under adiabatic expansion. Asano argues that the electronic states of the atoms in these vapors are thermally excited to higher levels, with this energy being converted to kinetic energy during expansion. The extra energy accounts for the increase in velocity, with uranium having the highest increase by virtue of its high degree of excitation. The increase in the case of titanium evaporation was significant, while the velocity increase for copper was quite low because of copper's low excitation. Experimental evidence of electronic excitation has also been reported by Nishimura et al [99], and acknowledged in other studies [61], [124]. However, very little work has been done on the inclusion the electronic mode of energy in numerical simulations. The consideration of this mode of energy is important in understanding the physics of electron beam evaporation, and this task is addressed in this dissertation.

Besides attempting to further the understanding of the evaporation process, a more practical aspect of the problem is considered here. In the materials processing industry, the development and refinement of the evaporation process as a manufacturing technique often requires a large number of experiments and/or simulations. The numerical modeling of the system under consideration is often a more cost-effective way of studying the evaporation, but the numerical simulations have the drawback of requiring large computation times. The intensity of the computation is often wasted in the nearly collisionless evaporation process. Hence, a more practical and elegant approach to the numerical modeling is developed in this study, with an emphasis on developing a method that produces accurate results while reducing the time of computation.

1.3 Description of the vapor deposition system

The work described in this dissertation constituted the numerical component of a joint study with the Lawrence Livermore National Laboratories (LLNL) on the physical vapor deposition of titanium. The experiments on the vapor deposition system were carried out in the Experimental Test Facility (ETF) at LLNL [40]. The ETF flow domain is described in this section with the schematic given in Figure 1.1. The adaptation of an unstructured computational grid to the geometry of the ETF is described in Chapter 4.

The ETF consists of an ultra-high vacuum chamber where the evaporation and deposition process take place. Like many other electron beam evaporation systems,

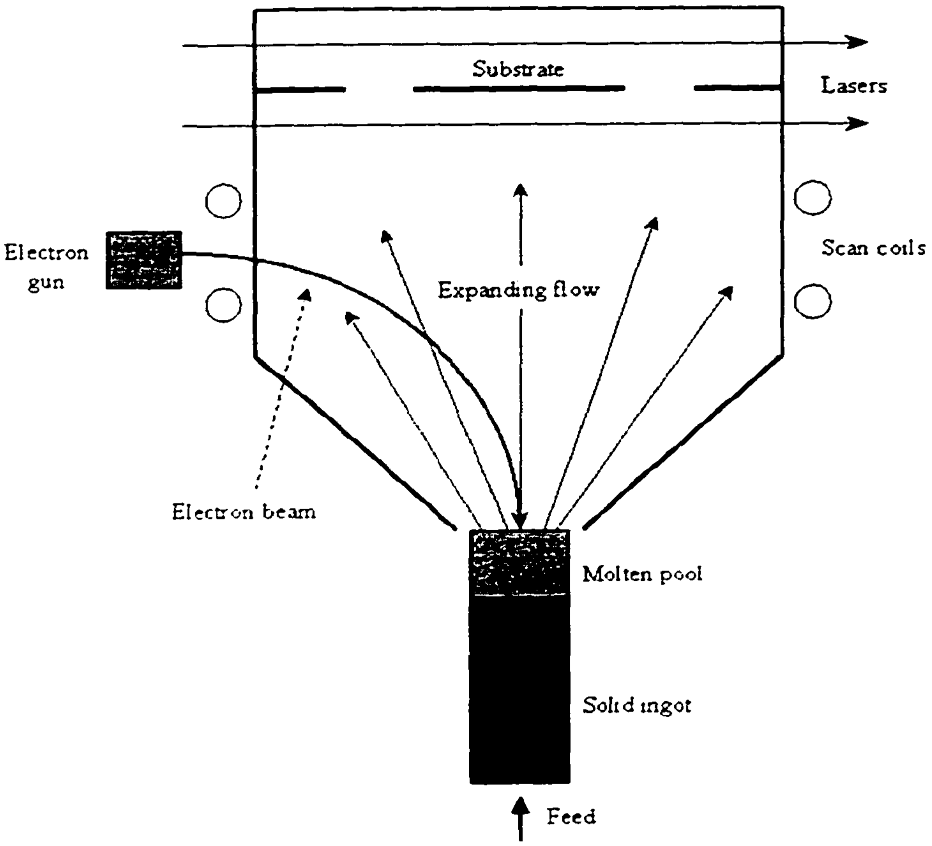

Figure 1.1. Schematic of the Experimental Test Facility (ETF)

the chamber pressures in the ETF are on the order of 10^{-3} *Torr* (10^{-1} *Pa*), which is nearly six orders of magnitude below atmospheric pressure. An electron gun generates a high-energy electron beam that causes the evaporation in the system. The electron beam is bent in the chamber by a magnetic field, which is generated by scan coils outside the chamber. The beam then strikes the surface of a metal ingot placed at the bottom of the chamber. Variations in the magnetic field, which are achieved by controlling the scan coils, alter the path of the electron beam through the chamber. The beam thus traverses the surface of the ingot in a circular pattern at very high frequencies, which are often on the order of a few kilohertz. The beam causes intense heating of the metal due to the energy transfer from the electrons. This creates a molten pool at the top of the solid ingot. Atoms evaporate from the surface of the pool into the chamber, where they undergo rapid expansion. The expanding vapor impinges on a substrate placed at the top of the chamber. The resulting adsorption deposits a film of the evaporant on the substrate. An immobile metal block plate is used as the substrate in the ETF in order to measure the deposition profile in the chamber. Manufacturing processes often use translating substrates to ensure uniformity of deposition on the substrate, as the deposition profile in the chamber is rarely uniform.

As the atoms evaporate off the surface of the molten pool, there is a reduction in the mass of the ingot. The surface of the pool is viewed through cameras from different angles. These cameras are used to monitor the height of the pool surface in relation to the rest of the chamber. A feedback mechanism is employed where the data from the cameras are used to control the feed rate of the ingot into the chamber, which keeps the surface of the pool at a constant level. The measurement of the feed rate thus provides the mass flux of the vapor into the chamber. The cameras often have a bleed of argon gas across the lens surface to prevent the deposition of the vapor atoms on the lens. This creates a low background pressure of argon in the chamber.

The thickness of the deposited film in the ETF is measured from the block plate. In addition to this data, other flow properties are also measured during the experimental run through laser absorption spectroscopy. In order to achieve this, laser beams are passed into the chamber through ports in its side. The lasers are tuned to the characteristic frequency of the atoms constituting the vapor. The data from these absorption scans provide the diagnostic information on the flow. Multiple lasers are used to measure different flow properties. Slits placed in the block plate collimate the flow, allowing the upper laser to measure the flow velocity and translational temperature along the direction of the laser.

1.4 Dissertation structure

This dissertation investigates physical vapor deposition of titanium, with an emphasis on improving the flow physics and the numerical efficiency of simulating the problem. A brief background of vapor deposition, its importance in the materials processing industry, the motivation behind this study and the specific details of the system under consideration are described in this chapter. Chapter 2 is devoted to a discussion of the computational technique used for a significant part of this study - the Direct Simulation Monte Carlo (DSMC) method [17]. This study includes the electronic mode of energy in the DSMC simulation. A case for the inclusion of this energy mode is made in Chapter 3. This is followed by a description of the model used for electronic energy in the DSMC method.

The results from the DSMC simulation of the vapor deposition of titanium are presented in Chapter 4. The effect of electronic energy on the simulated flow is quantified in this chapter. Comparisons are made between the simulation results and experimental measurements of the deposition thickness and flow properties. The phenomenon of backscattering of particles into the molten pool is also addressed in this chapter. Finally, various sensitivity studies are performed in order to provide an understanding of how variations in certain physical parameters affect the results of the simulation. Chapter 5 includes a discussion of the atomic absorption spectroscopy technique that is used to measure the flow properties in the domain. The absorption spectra computed from the DSMC simulations are compared with experimental scans in this chapter.

The later portion of this study is aimed at improving the numerical efficiency of the simulation for flow problems of this nature. With this objective, the Line Of Sight (LOS) method has been developed for near collisionless flows. Chapter 6 describes the motivation behind the development of the LOS method, its scope and possible variations in this technique. The structure of the LOS algorithm, the main routines involved and some computational issues are also discussed in this chapter. Chapter 7 is devoted to the results of simulations using the LOS method. This method is first validated through its comparison with a collisionless DSMC simulation. The flow in the ETF is then simulated with greater efficiency using a hybrid DSMC-LOS approach. The performances of the LOS and hybrid methods are compared with that of the DSMC method to demonstrate the efficiency attained by using the hybrid approach over the computationally intensive DSMC method. The dissertation is drawn to a close in Chapter 8 by summarizing the work done. Possible extensions to this study are also discussed here.

Chapter 2

Computational Modeling

The Direct Simulation Monte Carlo (DSMC) method forms the backbone of the analysis of the vapor deposition problem described in this work. This chapter is devoted to a description of the DSMC method, details of the physical modeling in the DSMC method, its appplication to the vapor deposition problem and the computational code used for the simulations.

2.1 The Direct Simulation Monte Carlo method

The DSMC method [14],[17] is finding increasing application to engineering problems in various fields. It has been extremely successful in extending the envelope of computational fluid mechanics by modeling non-equilibrium phenomena and transition flows. The DSMC method found early applications in modeling rarefied gas flows [20],[128] and shockwave structures [15],[18],[19]. Further work has been done in thermochemistry [32], spacecraft glow [78] and radiative emissions [42]. The method has also proved useful in modeling nozzle plumes and plume surface impingement [77]. The ability of the DSMC method to interface with the Particle In Cell method [27] has enabled the modeling of flows with electromagnetic effects and charged particle interactions. Examples include the modeling of electric propulsion devices [125] such as ion thrusters [126], Hall thrusters [79],[103],[104].

and arcjets [37],[71]. The DSMC method has also been used extensively to investigate materials science problems. The etching processes that are vital in the semiconductor industry can be modeled using the DSMC method [54], [65]. The hybrid DSMC–PIC approach has been used for modeling the charged particle flows in plasma etch reactors [53],[64].This method has also been used in modeling thin film growth [48],[46], chemical vapor deposition [50],[107], directed vapor deposition [67] and other applications in the microelectronics industry [10]. Of late, the DSMC method is also being used extensively to simulate flows at very small length scales, in applications such as micro-electro-mechanical-systems(MEMS) [96],[108],[110] and microchannel flows [59],[102].

The DSMC method is a particle method that is used to model dilute gases. The dilute gas condition can be defined by the relative magnitudes of the mean free path of the flow λ, the mean molecular seperation δ and the molecular diameter d. This condition is commonly expressed as:

$$\lambda \gg \delta \gg d \tag{2.1}$$

The mean free path of a flow is defined as the average distance that the atoms, molecules or particles in the flow travel before undergoing a collision with another particle. The large free path compared to the molecular diameter implies that binary collisions dominate in the flow, and tertiary collisions are extremely rare. The real atoms or molecules in a flow are modeled as computational particles, with each particle representing a large number of real atoms or molecules. The DSMC method uses the assumption that the time taken for a particle–particle interaction to occur, in the form of a collision, is negligible compared to the time taken for the particle's movement through one mean free path. The time step used in these simulations is also typically smaller than the mean collision time for a particle. Thus, a particle's motion can be decoupled from the collisions it undergoes. The fluid physics are modeled through these collisions and motions, which enable equilibriation and propagation of the flowfield properties respectively. The DSMC method is statistical in nature. The particle properties of mass, positions and velocities are averaged statistically to provide macroscopic properties and to model the mass, momentum and energy transport in a flow.

The DSMC method is applied to rarefied flows, often with the occurence of non-equilibrium phenomena and mostly in the transition regime between continuum and free molecular flows. The degree of rarefaction of a flow is represented by the Knudsen number given by:

$$Kn = \frac{\lambda}{L} \tag{2.2}$$

where L is the characteristic length of the flow. The properties of a particle in a flow change with every collision it undergoes, which implies that the macroscopic properties of a flow show gradients at the scale of the mean free path. Under continuum conditions, the mean free path is much smaller than the characteristic length and the flow properties show smooth gradients. Continuum flows have Knudsen numbers of the order of 10^{-3} or less and are usually modeled using finite difference schemes for a partial differential equation formulation. As the mean free path becomes comparable to the characteristic length, the flow enters the transition regime where flow properties no longer exhibit smooth gradients. Under these conditions, the differential Navier-Stokes equations used in continuum fluid dynamics break down, as the differential terms represent the gradients which may no longer be continuous. As the Knudsen number approaches unity, non-equilibrium effects may set in. Flows with $Kn > 10^1$ are considered to lie in the free molecular range. The DSMC method is often useful in cases where the flow changes in nature from a near continuum to the transition or free molecular regimes very rapidly.

The mathematical formulation behind the DSMC method is the Boltzmann equation. The Boltzmann equation for a monoatomic gas is expressed as:

$$\partial(nf)t + u_i\partial(nf)x_i + F_i\partial(nf)u_i = \int_{-\infty}^{\infty}\int_0^{4\pi} n^2(f_1'f_2' - f_1f_2)g\sigma d\Omega dU \qquad (2.3)$$

where $f(u_i, x_i, t)$ is the normalized distribution function, u_i is the molecular velocity, F_i is an external force per unit mass, g is the relative velocity of the colliding partners, σ is the differential cross section, $d\Omega$ is a solid angle element, dU is an element of velocity space, the subscripts 1 and 2 represent the two colliding partners and the prime denotes the post-collision distribution functions. The differential terms represent the transport properties and the integral term represents the collisions that alter the distribution function.

The Boltzmann equation has been analyzed using many different approaches, and some examples of these are provided by Vincenti and Kruger [127]. One approach is to analyze a simpler construct derived from the Boltzmann equation. Using this approach, Bhatnagar et al [12] created a collision model — called the BGK model – by replacing the collision integral in the Boltzmann equation by a simple relaxation model. Another approach is to consider small perturbations of the distribution function in the Boltzmann equation. The Chapman-Enskog expansion uses small deviations from local translational equilibrium to reduce the Boltzmann equation to a linearized form. The continuum assumptions may then be applied to this approach, where the viscous stress is proportional to the rate of strain and the heat flux is proportional to the temperature gradient, to yield the familiar set of continuum conservation equations called the Navier-Stokes equations. The third approach described in reference [127] assumes a functional form of the distribution function. This approach is useful over a wide range of physical parameters and is closest in spirit to the DSMC formulation.

When continuum breakdown occurs, it is still possible to obtain the flowfield properties by finding a solution to the Boltzmann equation. Analytical solutions are extremely difficult, if not impossible, as the equation describes a six-dimensional phase space of positions and velocities. Hence a statistical method is an attractive alternative. The DSMC method simulates the integral part of the Boltzmann equation though probablistic collisional interactions between particles while the differential part of the equation is modeled through particle motion. Early critics of the DSMC method contended that it provided an implicit solution to the Boltzmann equation, and that the randomness inherent in the DSMC method could lead to a distortion of the Boltzmann equation. However, Bird showed that the DSMC method can be directly related to the Boltzmann equation and is entirely consistent with it [21] .

The DSMC algorithm may be represented as follows:

1) All particles are moved through the computational domain through distances equal to the product of their instantaneous velocity components and the time step.

2) In each cell of the domain, particles are paired with one another at random.

3) The probablity of a collision occuring between the particles of a collision pair are evaluated and the particle properties are replaced by the post-collision values.

4) If sampling is required, the particle properties in each cell are summed to provide a large statistical sample.

The various aspects of the algorithm are explained in greater detail in the sections that follow.

2.1.1 The computational particle

Real flows have an extremely large number of atoms, molecules and constituent particles that interact with one another. It is impossible to model each of these atoms or molecules individually in a numerical simulation. Hence the flow is modeled using a number of computational particles, each of which represents a large number of real atoms or molecules. The properties of these computational particles model the real distribution function over the course of the simulation. The term "particle" is used often in this dissertation. It must be clarified that this term refers to the computational unit in the DSMC simulation which represents an aggregate of real atoms and molecules, rather than a physical entity in itself.

The computational particles have various properties associated with them. They are considered to be point masses with spherical potential fields, which ensures that collisions between particles do not have any stearic effects associated with them. The particles are assigned molecular masses and a molecular diameter for the calculations involved in the collision mechanics. Particles also have associated positions in space and velocities along three coordinate directions which change over the course of the simulation. They also have internal energies associated with them in the form of rotational, vibrational and electronic modes of energy. The particle velocities and internal energies change only during a collision. The positions, and the velocities in the case of axisymmetric flows, change during particle movement. The collisions are modeled using probabilities from kinetic theory, so as to preserve the theoretical macroscopic collision rate. Collisions between particles are explained in greater detail in Section 2.1.3.

2.1.2 Particle movement

The movement of a particle through the computational domain in a DSMC simulation is independent of its interaction with other particles. The particle trajectories are computed in each time step and the particle position is updated in the flow domain. External body forces are usually neglected in a pure DSMC simulation, thus giving the particles no acceleration during their motion. The particle trajectories are thus straight lines with the final position after the move given by:

$$x_{\vec{new}} = x_{\vec{old}} + \vec{V}\Delta t \tag{2.4}$$

where $\vec{x}$ and $\vec{V}$ are the position and velocity vectors of the particle respectively and Δt is the time step used for the move. When coupled with PIC models where electromagnetic fields affect charged particles, or when gravitational fields exist, particle motion has an acceleration that updates the velocity as well as the position.

Equation (2.4) is applicable for the movement of particles in the case of one, two and three dimensional simulations. However axisymmetric flows are treated in a special way [51] to reduce the effective dimensionality from 3 to 2, while still allowing velocities in all 3 dimensions to affect the movement of the particle. This leads to a more complex particle motion. The two dimensional plane of the simulation represents any angular plane around the axis of symmetry. The particles leave the simulation plane due to their azimuthal velocity and are rotated back into the simulation plane through a transformation of their positions and velocities. The resulting trajectory in the simulation plane is hyperbolic, with the axis of symmetry being the axis of the hyperbola. The simulations described in this study are all axisymmetric in nature.

Particle motion also allows the particle to encounter boundary conditions, which represent inflows, outflows, walls and axes of symmetry. A particle that crosses an inflow or an outflow boundary is removed from the simulation. When a particle strikes a wall, it can either be reflected or removed from the simulation through the use of a sticking condition. Reflections range from being fully specular to fully diffuse in nature through the use of a wall accommodation coefficient. In a specular collison with a wall, particles are reflected with the angle of incidence equalling the angle of reflection. On the other hand, a diffuse reflection causes the reflected particle to have its velocity components sampled from an equilibrium Maxwellian distribution function at the wall temperature, irrespective of the incoming velocity of the particle. Partial accommodation leads to a fraction of the collisions being specular in nature and the remainder being diffuse. The sticking conditions at the walls are modeled though a wall sticking coefficient, which allows the walls to fall in the range between being perfectly reflecting and perfectly sticking. Partial sticking conditions employ a procedure similar to partial accommodation, where a fraction of the particles are removed from the simulation.

2.1.3 Particle Collisions

Collisions in a real flow occur at the level of a mean free path, which is also the length scale for gradients in the flowfield. In order to model this closely, collisions in a DSMC simulation occur between particles that are separated by a distance less than one mean free path. This is achieved by dividing the computational domain into cells whose sizes are a fraction of the mean free path, this fraction usually being close to 1/3, and allowing collisions only between particles in the same cell. Due to the statistical nature of the DSMC method, particles in the same cell are paired with each other in a random manner to form a list of possible collision pairs.

An actual collision between a pair of particles is then dependent on an accept-reject scheme.

The collisions in the DSMC method are modeled to match the collision rate predicted by kinetic theory. Early schemes to model the collision mechanics included the Time Counter and the No Time Counter schemes [14]. Another scheme was developed by Baganoff and McDonald [7] to adapt the collision mechanics effectively on vector computer architectures. This scheme has been used to model collision probabilities in this study. The probability of collision between two particles using the Baganoff-McDonald scheme is given by:

$$P_{coll} = \frac{N_i N_j W_P \Delta t \sigma g}{SV(1 + \delta_{ij})} \left[\frac{2(2-\omega) R T_{ref}}{\mu g^2} \right]^{\omega} \tag{2.5}$$

where N_i and N_j are the number of particles of species i and j respectively, g is the relative velocity of the collision pair, μ is the reduced mass of the collision pair, S is the total number of collision pairs considered in a cell in a single time step and V is the volume of the cell. The delta function is included to avoid counting the same collision pair twice in a single species collision. W_P is the particle weight, which specifies the number of real atoms or molecules that are simulated by one computational particle, and Δt is the time step used in the simulation. The collision cross section σ and the viscous parameter ω are dependent on the collision model. The parameter ω is dependent on the force constant η from the inverse power law, which is expressed in equation (2.9). This relationship is written as:

$$\omega = \frac{2}{\eta - 1} \tag{2.6}$$

ω has a value of zero for the hard sphere model and ranges between 0 and 0.5 for the collision models used in the DSMC simulation.

Various collision models are used in DSMC simulations to model the collision mechanics. The Variable Hard Sphere (VHS) model [24], which has been used in this study, treats particles as solid spheres that undergo isotropic scattering. The collision cross sections of the particles are variable and are a function of the relative velocity of the colliding particles.

$$\sigma = \sigma_{ref} \left(\frac{g_{ref}}{g} \right)^{2\omega} \tag{2.7}$$

where ω is a parameter relating to the coefficient of viscosity of the fluid. Thus, the collision cross section decreases for high energy collisions. The scattering angle in a VHS collision obeys a cosine distribution given by:

$$\chi = 2\cos^{-1}(\frac{b}{d}) \tag{2.8}$$

where b is the impact parameter in the center of mass frame of reference.

Another collision model called the Variable Soft Sphere (VSS) model was proposed by Koura and Matsumoto [82], [83] to deal with certain problems with the VHS model. The VHS model correctly represents the repulsive intermolecular potential according to the inverse power law:

$$F = K/r^{\eta} \tag{2.9}$$

This leads to a collision cross section and collision rate consistent with the inverse power law. However, the predicted diffusion coefficient in the VHS model does not match that predicted by the inverse power law. The VSS model addresses this by varying the distribution of the scattering angle:

$$\chi = 2\cos^{-1}\left[\left(\frac{b}{d} \right)^{1/\alpha} \right] \tag{2.10}$$

This favors scattering at smaller deflection angles when compared to the isotropic VHS scattering. Various other models like the Generalized Hard Sphere (GHS) [72] model extend the scope of the VHS and VSS models.

Collisions in the DSMC method are considered in the center of mass frame of reference. Momentum and energy are conserved during a collision. The momentum conservation is achieved by keeping the velocity of the center of mass a constant during the collision. The collision energy is conserved, but it can be redistributed among the translational and internal energy modes. The energy transfer between the internal modes is modeled phenomenologically to match the macroscopic relaxation rates for the energy mode under consideration. In this study, only monoatomic species are considered. Thus, the only applicable mode of internal energy is the electronic mode, and the treatment of this mode is discussed in Chapter 3.

Though momentum and energy are conserved in a collision, the angular momentum is not. This occurs because the post-collision velocities are selected at random while satisfying the momentum and energy conservation criteria. The non-conservation of angular momentum in a collision has been the subject of controversy [91]. However, it ceases to be an issue when cells are scaled properly to the mean free path. In this case, the DSMC method has no difficulty in capturing extremely rotational phenomena, such as flows with vorticity [25].

Though exact trajectories and scattering angles can be determined from collision mechanics, the DSMC method does not follow this approach to avoid becoming computationally intensive while simulating large numbers of particles. Instead, the post-collision velocities of the scattering particle are chosen statistically to model the scattering angles and velocities predicted by the collision model. In this respect, the DSMC method differs from some other particle methods like the molecular dynamics method, which uses intermolecular potentials to compute the exact trajectories of the scattering particles.

2.1.4 Numerical issues

The DSMC method is a statistical method where microscopic properties of computational particles are changed during the simulation. Some form of averaging is needed to translate these microscopic properties to the more familiar macroscopic properties. The macroscopic flowfield density, velocity and temperature can be obtained from an equilibrium velocity distribution function using the zeroth, first and second moments, which represent the mass, momentum and energy of the distribution function. In a DSMC simulation, these moments are obtained by sampling and summing the particle properties in each cell over the course of the simulation. These sums are later averaged over the sample size to provide the macroscopic properties. Since the macroscopic properties are a stastistical average of the microscopic properties, they show a certain amount of statistical error. This error is proportional to the inverse square root of the sample size.

$$\epsilon \propto N^{-1/2} \tag{2.11}$$

Various studies have been performed on reducing the statistical error in the DSMC method [47],[58]. One issue in the statistical averaging is that the macroscopic temperature is obtained using an assumption of equilibrium, which may not hold in some cases. Under non-equilibrium, the temperature has no meaning. The results of the DSMC simulation must be analyzed for the breakdown of equilibrium, and the temperature calculated under such non-equilibrium conditions must be recognized as a numerical extrapolation of an equilibrium concept, rather than a physical property.

However, there is no real way to avoid this assumption, and the macroscopic flow properties must be put in the proper perspective when simulating non-equilibrium flows with the DSMC method.

DSMC simulations always have a transient phase where the computational system of particles propagates information through the computational domain before reaching a relatively steady condition. Sampling is usually done after the transient phase in the case of steady flows. Unsteady flows need shorter and more intensive sampling than steady flows to capture the time variant nature of these flows. In this case, ensemble averages may be used to reduce the statistical error. Ensemble averages are generally not used for steady flows, as an extended sampling period generates statistics that are just as accurate. This effect occurs due to the inherent randomness of the DSMC method, which does not allow the simulation to be reversed in time, unlike some other methods employing distribution functions.

2.1.5 Application of the DSMC method to vapor deposition

The DSMC method is well suited to study the vapor deposition process described in this work. The vaporization of titanium from the melt occurs at very low densities, which are of the order of $10^{22}\#/m^3$. This is followed by an extremely rapid expansion of the flow, which is dominated by collisions. Thus huge gradients exist in the flow near the melt. The expansion causes a decrease of 3 to 4 orders of magnitude in the density. This can be analysed quickly through a mass balance:

$$(Flux.Area)_{melt} = (Flux.Area)_{substrate} \tag{2.12}$$

At the melt, the flux is of the order of $10^{24}\#/m^2s$ and the diameter of the chamber is approximately $0.04m$. At the substrate, the diameter of the chamber is $0.4m$. Thus, the flux and the density must drop through two orders of magnitude at the substrate due to geometric effects alone. There is a further decrease in density due to the increase in velocity that occurs during expansion. Moreover, some of the vaporized titanium may be lost due to sticking conditions on the walls, which contributes further to the decrease in density. Overall, these effects could combine to cause a decrease in density that is greater than 3 orders of magnitude. These low densities and the rapid expansion that is observed cause the flow to fall in the transition and free molecular regimes. The nature of the flow thus makes it difficult to model using continuum methods, and makes the DSMC method an ideal choice for this study.

2.2 MONACO - An overview

2.2.1 Structure

MONACO is a DSMC software package that has been developed at Cornell University [51]. Today, the code is capable of performing DSMC simulations for two-dimensional, axisymmetric and three-dimensional flows, along with zero and one-dimensional simulations for testing physical models. It has been designed to run on a wide range of architectures, ranging from scalar workstation architectures (SGI, Sun, HP) to parallel machines with scalar architectures (IBM SP-2) and vector supercomputers (CRAY Y-MP/C90). The base code is powerful and flexible enough to be applied to a wide range of flow situations. Also, the implementation philosophy has catered to easy and efficient modifications of the code for the analysis of specific problems. This has been achieved through an object-oriented paradigm using the C programming language. A range of utilities have also been developed to interface with MONACO. These help evaluate macroscopic properties from sampled data and also aid in grid generation and translation of the grid format.

The object-oriented paradigm allows MONACO to be modular in nature. The various functions that are performed by the code have been separated into three libraries. The kernel library contains the heart of the DSMC algorithm and also performs tasks pertaining to coordination of various routines and memory management. When the code is run on a parallel platform, this library also coordinates communication and message passing among the different processors. The geometry library contains routines that initialize the grid and cell data structures. It also controls the generation of new particles at inflow boundaries and tracks the movement of particles in the computational domain. The library of physical routines includes models that capture the actual physics of the simulation. These routines sort collision pairs, perform the collision mechanics, allow translational and internal energy exchanges, handle boundary interactions and allow chemical reactions to be modeled in the flow. The modular nature of the code thus allows easy manipulation of individual routines, an example being the inclusion of electronic energy in the internal energy model. This is described in detail in Chapter 3.

2.2.2 Memory management

MONACO was developed primarily with scalar workstation architectures in mind. The memory management differs considerably from traditional DSMC implementations, which use cross-referenced arrays of cells and particles. Instead, MONACO uses the cells as a primary data structure, with particle data structures being assigned to and removed from the cell as the particles transit through the cell. This allows the code to make efficient use of the cache memory on workstations. Thus, the processor performs calculations on the data already loaded into memory while more data is being reloaded into the memory cache. This format shows significant advantages in performance when compared to traditional DSMC codes.

The organization of the cell and particle data structures necessitates dynamic memory allocation, as opposed to the use of static structures. This need is reflected in the choice of the C programming language, which has a further advantage in the inclusion of architecture–specific options during compilation of the code.

2.2.3 The Computational Grid

MONACO allows the use of unstructured grids in the DSMC simulations. Unstructured grids have many advantages over structured grids, such as adaptation to complex geometries and allowing easy refinement of the grid to the scale of the mean free path. The use of unstructured grids lends itself well to the localized data structures used in MONACO. The primary purpose of the grid in the DSMC simulation is to allocate collision pairs among the particles in the flow domain. Collisions are only allowed within a cell, which satisfies the physical requirements of a collision occuring within one mean free path. Hence the cell data structure is organized such that the cell is an independent enity within the flow domain, with only its properties and its connectivity to its neighbors being specified. This data structure allows the entire domain to be represented efficiently.

The format used for the representation of grids in MONACO was developed by the National Grid Project (NGP) [122]. This format is equally applicable to structured and unstructured meshes. In the NGP format, the nodes in a computational domain are specified. The cells and the edges are defined through connectivity between the consituent nodes. The NGP format also includes boundary definitions as part of the grid definition. This allows the code to handle a variety of flow problems and different boundary conditions without any recompilation or modification to its structure.

2.2.4 Physical Models

The physical models pertaining to various aspects of the flow physics are present in individual modules. This enables easy replacement or augmentation of a physical model. MONACO also allows zero–dimensional simulations, which are used to assess the effect of various physical models on the simulation. The collision mechanics employ models for the collision probability and the collision cross section. As described in Section 2.1.3, MONACO employs the Baganoff–McDonald scheme to calculate the probability of a collision occuring. The collision cross section is computed using the VHS model, with the scope for easy extension to the VSS model. Translational energy exchange takes place through a random sampling of post-collision velocities that conserves the collision energy. The rotational energy exchange employs a discrete rigid rotor model developed by Boyd [29]. Vibrational energy exchange is performed using the Borgnakke–Larsen model for a harmonic oscillator [28]. The mechanism of electronic energy exchange is explained in Chapter 3.

Chapter 3

Electronic Energy Modeling

The DSMC method, as described in Chapter 2, is an extremely powerful tool for simulating flows using computational particles, each of which represents an aggregate of molecules. In the traditional DSMC method, these particles are considered to possess three modes of energy - translational, rotational and vibrational. These energy modes of a particle are considered to be identical to those of the molecules represented by the particle. The translational energy of a molecule is representative of its velocity. The rotational energy arises as a result of the angular displacement of its component atoms about an axis that is fixed relative to the molecule. The vibrational energy of the molecule arises from the displacement of the component atoms relative to one another. Hence the rotational and vibrational energies arise only for polyatomic species.

In addition to the three traditional modes of energy, molecules can also undergo electronic excitation, where electrons in a certain atomic (or molecular) energy level can be transferred to a different energy level through an excitation process. This mode of energy is not usually considered in DSMC simulations. One reason for its exclusion from early research using the DSMC method is that the temperature regimes of interest were low enough to ignore electronic excitation. The reasoning that could have led to the exclusion of electronic energy from these calculations is that the nature of the species used may not have made excitation a significant phenomenon. Atomic and molecular species that have electronic states with low excitation energies can have a significant fraction of the population with electrons in the higher energy orbitals. An analysis of the electronic energy content of the system at the temperatures of interest, as described in Section 3.1, yields a clear picture as to whether electronic energy is important in the modeling or not. The consideration of the traditional three modes is sufficient to accurately model the flow physics in cases where excitation is negligible. In the EB-PVD process, the high energy of the electron beam causes the metal ingot to be heated to extremely high temperatures, often in excess of 2000 K. The resulting molten pool has atoms that vaporize off its surface at these high temperatures and electronic excitation could be significant in the vaporized atoms at these temperatures. Besides this, the vaporization of titanium results in a vapor comprising of a monoatomic species, where the only applicable energy modes of a particle are the translational and electronic modes. Thus, the transfer of energy between these modes could affect the simulated physics considerably when compared to a case where only the translational mode is modeled. It is thus considered important to assess the possible impact of including electronic energy in the simulations, and to follow it up by modeling this mode of energy if necessary.

Before proceeding further, it is necessary to consider the terminology used in this dissertation in the context of electronic energy. An atom or a molecule has many electrons present in various orbital shells around the nucleus or nuclei, with the electrons in each orbital shell possessing the quantized energy corresponding to the orbital shell. This is referred to as an energy state in the context of the physical state of the atom or molecule. Each orbital shell may possess energy states with slightly different energies and degeneracies. In section 3.3, it is explained how these states are combined into one "super-state" for computational purposes. This super-state is referred to as an energy level in the context of the computational particles in the simulations. Electrons in the physical atom or molecule can be transferred between two energy states with different energies through the process of excitation and de-excitation. The energy-state with the lowest energy is termed the ground state and electrons in this state can only be excited to higher energy states. The ground state is thus used as a reference for the energies of the higher states. The excitation energy to an energy state is hence numerically equal to the electronic energy content of that state. By this definition, the electronic energy of the ground state is zero. Some of these points are discussed in greater detail later in this chapter.

In this chapter, we first make a case for the inclusion of electronic energy in the vapor deposition modeling of titanium. This is done by considering the relative magnitudes of the translational and electronic modes and by considering a simplistic calculation of expansion of a titanium vapor with these energy modes. This is followed by the details of the selection of energy levels for inclusion in the DSMC simulation and the computational model for collisional electronic energy exchange in the DSMC method. Finally, the concept of the electronic temperature is introduced as a tool to analyze the importance of electronic energy in the simulations.

3.1 Quantifying the effect of electronic energy

Evaporation processes into low pressures, such as the vaporization of titanium from the molten pool, are normally characterized by rapid expansion from the vapor source. The temperature of the gas in such expansions falls rapidly, thus leading to a large variation in the temperature across the domain. In order to consider the inclusion of electronic energy in the DSMC simulations, it is necessary to evaluate the fraction of the flow energy present in the electronic mode over the temperature range of interest. Figure 3.1 shows a comparison between the average translational and electronic energy per particle of titanium in an ambient temperature range of 10 - 3000 K. The translational energy of the particle varies as $(3/2)k_BT$, from kinetic theory.

At equilibrium, the electronic energy of a particle can be analyzed using the Boltzmann distribution:

$$\frac{N_j}{N} = \frac{g_j e^{-\epsilon_j/k_BT}}{\sum\limits_j g_j e^{-\epsilon_j/k_BT}} \tag{3.1}$$

where N_j and N are the number of particles, or the population, of electronic level j and the whole system respectively. The degeneracy of level j is represented by g_j and its excitation energy, or electronic energy content, is represented by ϵ_j. This equation specifies the fractional population of each energy level in a system of particles in equilibrium at a temperature T and thus provides a measure of the excitation of this system. The total energy content of this system of N particles in equilibrium is thus $\sum_j \epsilon_j N_j$, where $\epsilon_j N_j$ is the energy content of each level. The average electronic energy per particle is thus given by $\sum_j \epsilon_j \frac{N_j}{N}$. When the electronic energy of titanium atoms is expressed in units of temperature, the first four energy levels lie at values of 0, 244.79, 556.65 and 9612.17 K above the ground state (Table 3.1). These values are obtained from an analysis of the experimentally measured excitation energies of titanium, as explained later in this chapter.

The low excitation energies of the first three levels cause a rapid excitation to these levels at low temperatures. In Figure 3.1, this explains the rapid increase

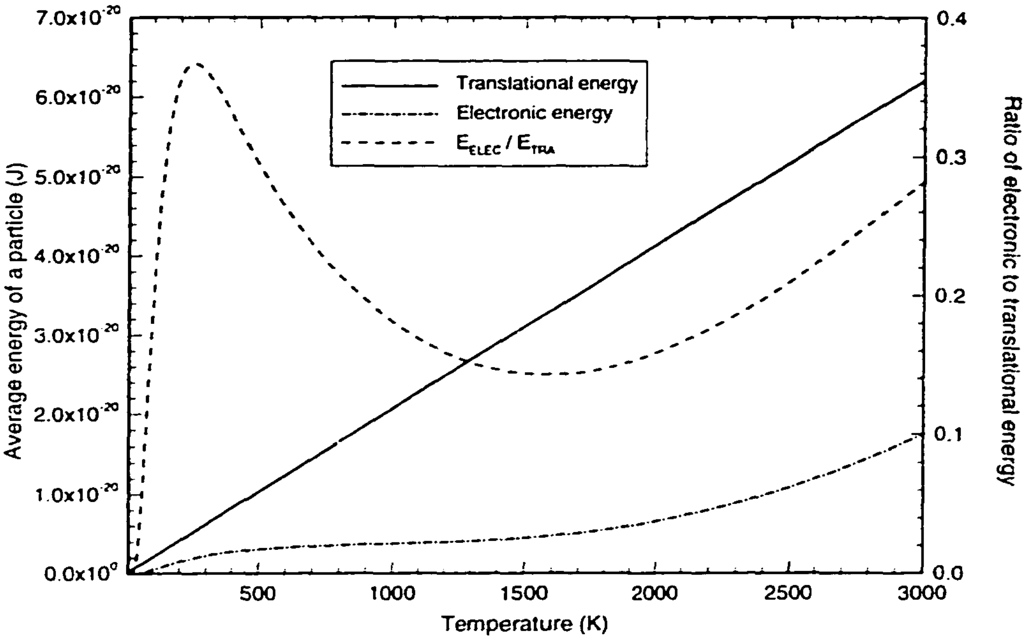

Figure 3.1. Average energy of a particle in the translational and electronic modes

in the electronic energy in the low temperature range (0 - 500 K). The higher levels have very small population fractions in this range, as a very small fraction of particles have energies high enough to excite electrons to these higher levels. At higher temperatures, excitation occurs more easily to the higher levels. Since the excitation to the higher levels occurs from the lower levels, the populations of the ground and the first two excited states drop accordingly (Figure 3.2), thus increasing the electronic energy content of the system. Thus the average electronic energy increases rapidly at temperatures above 2000 K.

The ratio of the electronic to the translational energy of a particle is significant (> 15 %) in the high temperature range, which is characteristic of the region above the melt surface. At a source temperature of 2500 K, a simulation that considers both translational and electronic energy will have 21% more energy than a corresponding simulation that considers only translational energy. At the lower temperatures (< 500 K), the ratio of the electronic to the translational energy is as high as 35 %. This low temperature range is characteristic of a large part of the flow domain, as the flow undergoes rapid expansion. The extra energy considered in a simulation with electronic energy could make a difference to the expansion of the vapor. Besides this, the high ratios throughout the flow domain indicate that the transfer of energy between the electronic and translational modes may be significant. Such a transfer of energy could affect the flow significantly by causing an increase in the macroscopic flow velocity and a change in the flux to the substrate, which is of primary importance in this study. Thus, the consideration of the electronic mode of energy in the DSMC method could be crucial for the accurate modeling of the flow.

3.2 Theoretical Analysis

Using the principle of energy conservation, it is possible to make an estimate of the change in flow properties when electronic energy is considered. This is done by considering the expansion of a vapor from the surface of the melt, where it has zero mean velocity. For simplicity, the vapor is allowed to expand until it attains a temperature of 0 K, which corresponds to perfect (or total) isentropic expansion. Hence the energy of the vapor at the melt surface is converted completely into kinetic energy. In this analysis, the temperature of the melt is taken to be 2500 K and the molecular weight of titanium is 47.9 kg/kmol. When electronic energy is not considered, the energy balance can be written as:

$$C_P T_0 = C_P T + \frac{v^2}{2} \tag{3.2}$$

where C_P is taken in units of J/kg-K. When the vapor is expanded to a temperature of 0 K, this reduces to :

$$v_{max} = \sqrt{2C_P T_0} \tag{3.3}$$

Substituting the above values, the maximum attainable velocity of the vapor without consideration of electronic energy is calculated to be 1473 m/s.

When electronic energy is considered, the energy equation can be written as:

$$C_P T_0 + (EE)_{T_0} = C_P T + (EE)_T + \frac{v^2}{2} \tag{3.4}$$

Since the atoms are completely de-excited at 0 K, the electronic energy content at this temperature, $(EE)_{T=0}$, is zero. The maximum attainable velocity in this case reduces to:

$$v_{max} = \sqrt{2(C_P T_0 + (EE)_{T_0})} \tag{3.5}$$

From Figure 3.1, the ratio of the electronic energy to the translational energy at 2500 K is calculated to be 0.21. Using this in Equation (3.5), the maximum attainable velocity is calculated to be 1620 m/s.

Thus the maximum attainable velocity is seen to increase by nearly 150 m/s when electronic energy is considered, representing an increase of 10 % over the value when only translational energy is considered. This difference is extremely important to resolve in the flow domain.

This analysis provides an idea of the change in flow velocity when electronic energy is included and excluded, under isentropic conditions. This behavior is unlikely to be true in the real flow due to various non-equilibrium effects and the variation in the temperature across the source. However, this can be used to obtain an estimate of the effect of inclusion of electronic energy, for subsequent comparison with the simulations.

Based on this analysis and the discussion in Section 3.1, it is concluded that the inclusion of electronic energy may affect the simulations significantly. It is thus important to obtain a computational model for the inclusion of electronic energy in the DSMC simulation. The details of this model are explained in detail in Section 3.4.

3.3 Selection of energy levels

In order to accurately model the electronic energy of an atom in the simulation, it is necessary to input an accurate representation of its electronic states to the simulation. The data for the electronic states of an atom are available in literature in the form of spectroscopic measurements. The spectroscopic data for titanium are presented in references [94] and [120], with the energy levels being measured by the number of spectroscopic lines per unit measure of length. These are converted to energy levels through a simple conversion factor of 8065.479 cm^{-1}/eV, or 1.4387 K/cm^{-1} for clarity of comparison. The data is presented as energy states grouped by electronic configuration, with each energy state having an associated total angular momentum quantum number J. The various energy states corresponding to a given electronic configuration can have very comparable energies. Hence, an approximation is carried out by averaging the energies of all the states to yield the excitation energy to that orbital shell configuration. The degeneracy of this configuration is obtained by summing the degeneracies of each state contained in it, where the degeneracy of each state is given by:

$$g = 2J + 1 \tag{3.6}$$

This reduced representation of the excited states of the atom may thus be translated to the computational model, with each computational electronic level corresponding to a reduced orbital shell configuration. The energy of the computational level equals the excitation energy corresponding to the reduced configuration. The degeneracy of the computational level equals the sum of all the degeneracies that contribute to the reduced configuration. This is done to conserve the total number of states in the physical atom.

The selection of energy levels depends on two criteria — the populations of the energy levels and the electronic energy contained in each energy level. This can be analyzed using Equation 3.1, to yield the equilibrium distribution of particles over the energy levels at various ambient temperatures. When the equilibrium distributions are plotted on a semi-log scale of the average population of the energy states in a level $(\frac{N_l/g_l}{N})$ *vs* the energy of the levels, they yield straight lines. The slopes of the distribution lines are inversely proportional to the temperatures of the distributions. The equilibrium distributions must be analyzed at temperatures that cover the range found in the flow field. This provides an idea of the levels of excitation that can be expected at different points in the flow field.

Since a DSMC simulation is statistical in nature, the error associated with sampling is proportional to the inverse square root of the population. Also, the chance that a level may be sampled at any given time is inversely proportional to its fractional excitation (or fractional population). For example, a simulation may have 10^6 particles at any time, with each particle having an average residence time of 100 time steps. If we have a sampling period of 10000 time steps, there would be total of $10^6 \times 10000/100$, or 10^8, individual sampled particles. Thus if an electronic level had a fractional population of 10^{-8}, one might expect to see

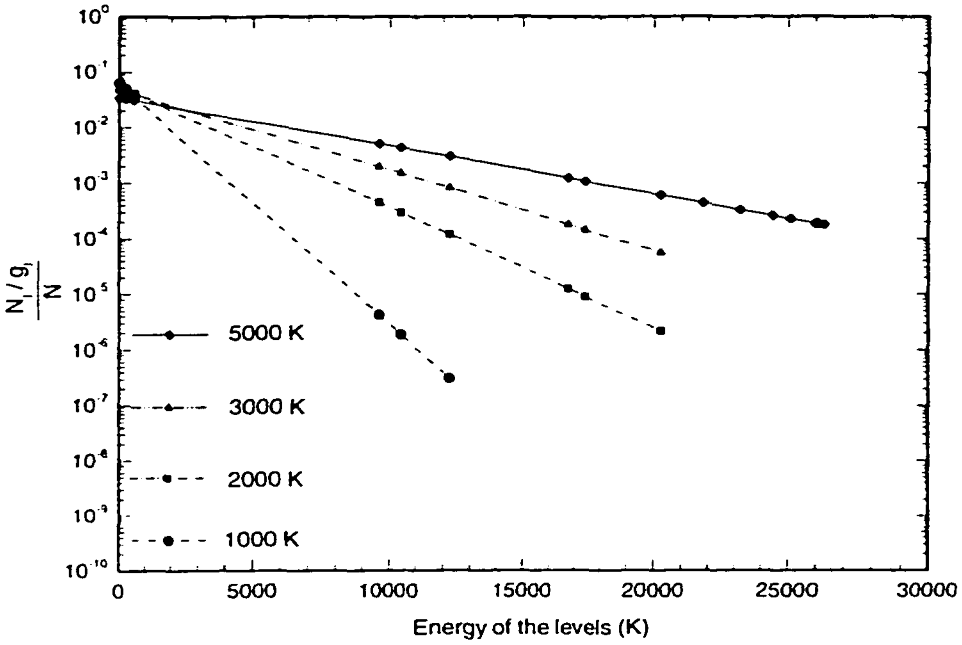

Figure 3.2. Boltzmann distribution of titanium at various temperatures

one particle excited to this level among the sampled data. The error associated with the sampling of this level is large and the resolution may in general be coarse for the higher energy levels with low fractional populations. Thus, the analysis of the fractional populations of the energy levels, as predicted by the Boltzmann distribution (Eq. 3.1) provides an idea as to which levels may be included in a simulation in a statistically significant manner.

Although the analysis of the fractional population of an energy level offers a good yardstick for its consideration, its energy plays an important role too. Some high energy levels with high excitation energies and/or high degeneracies may contain a significant fraction of the total energy of the system, despite their low fractional populations. In order to correctly represent the energy distribution across various levels, it is thus necessary to consider the electronic energy content

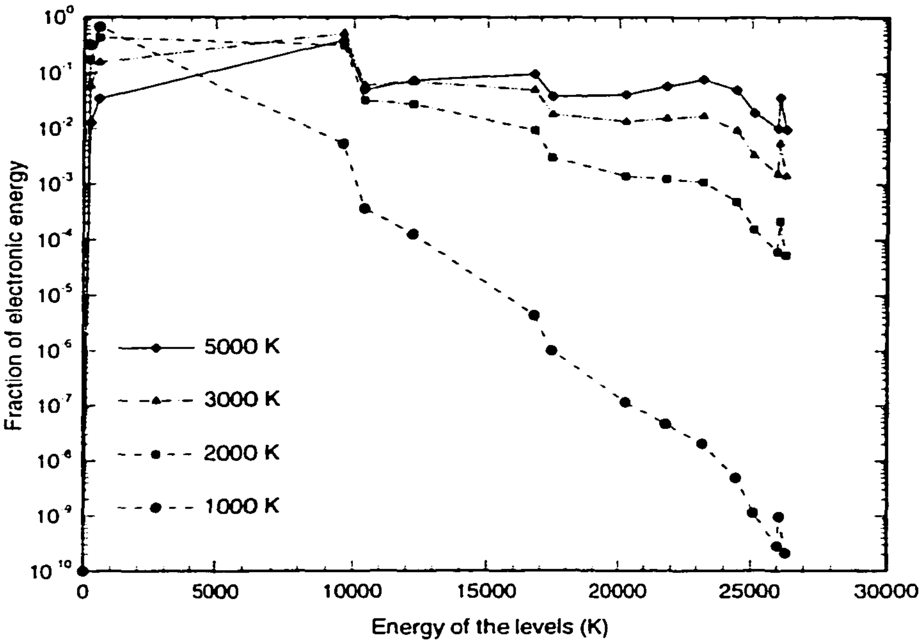

Figure 3.3. Electronic energy content in the Boltzmann distribution of titanium at various temperatures

of each level in addition to the fractional population. The electronic energy content in this case is simply the product of the population of the level and its excitation energy.

The reduced representation of the electronic levels of titanium are listed in Table 3.1. From (Eq. 3.1), the fraction of atoms in any energy level depends on the temperature, the energy and the degeneracy of the level. The ambient flow temperature of the system under consideration is low compared to the excitation energy of the higher energy levels, which are in excess of 10000 K in units of temperature. The temperature at the molten pool of titanium, which serves as an inflow to the simulation, varies between 2700 and 3000 K. Since the titanium vapor undergoes expansion, the temperature in the flow domain is always lower than the inflow temperature. The populations of the higher energy levels fall exponentially.

Table 3.1. The first 16 reduced energy levels of titanium

Energy Level	Energy (K)	Degeneracy
1	0.00	5
2	244.79	7
3	556.65	9
4	9612.170	35
5	10439.89	5
6	12245.26	9
7	16761.80	21
8	17436.53	9
9	20264.21	15
10	21815.48	27
11	23218.71	45
12	24444.45	35
13	25100.06	15
14	25996.48	9
15	26077.22	33
16	26313.02	9

This provides a rough estimate of the number of levels that need to be included in the analysis. In the case of the problem considered. 16 levels of titanium are taken into consideration, as listed in Table 3.1. The energy of the first level (the ground state) is zero by the convention used. while the highest level considered is on the order of 35000 K. The Boltzmann distribution for these 16 levels is then calculated at equilibrium temperatures of 1000, 2000, 3000 and 5000 K. This is done to get a fairly complete picture of the distributions at different temperatures that could be present in the flow. The distributions of the population fractions (Fig. 3.2) and the energy content of each level (Fig. 3.3) are plotted against the excitation energy of each level. The plots are then analyzed to select the energy levels to be included in the simulation. The population and energy distributions at an equilibrium temperature of 5000 K are considered conservatively as this value is a little higher than the expected upper bound of the range of temperature in the simulation. From Fig. 3.2, the population fraction of the seventh energy level is on the order of 10^{-3}, which can be resolved accurately by sampling a large enough number of particles. This level also has a larger degeneracy than its neighboring levels, which causes it to contain a larger fraction of the energy. The fraction of the total energy in the higher energy levels at this temperature is assumed to be negligible. Hence the first 7 levels are considered for the simulation.

3.4 Computational model

Every particle in the simulation is assigned a number of flow properties, including the velocities along the three axes and the electronic level. The electronic levels of a particle are quantized and are assigned as a property of the particle. The energy and the degeneracy of the particle's electronic level are thus implicitly defined using an input data file for these properties. When a particle undergoes a transition in its electronic level, its associated electronic energy is changed implicitly by a change in its electronic level property. However, the energy is explicitly used for collisions of the particle with other particles or walls.

3.4.1 Assumptions

Electronic excitation is a phenomenon that has been investigated extensively. However, considerable ambiguity exists regarding various physical parameters involving electronic excitation and collisions between particles in various excited states. These parameters have not been measured for all systems. The electronic energy model used in this work employs a few simplifying assumptions to clearly define the scope of electronic excitation and electronic energy transfer during collisions.

First, the underlying principle behind the excitation of particles is considered to be purely a process of local thermal equilibriation in accordance to the Boltzmann distribution (Eq. 3.1). Elaborating on this, whenever a particle is assigned an energy level, this property is obtained based on probabilities predicted by the Boltzmann distribution alone. There is no contribution to this process from any other factors. By this assumption, excitation from photons is effectively ignored in the simulation, as is the excitation caused by the electron beam used for the vaporization process. This is true of the excitation of particles generated through ambient or inflow conditions. Another phenomenon that is not considered is the spontaneous de-excitation of particles or energy loss through photons emitted by the particles undergoing de-excitation. Many excited states decay rapidly, with lifetimes of the order of 10^{-12} to 10^{-8} seconds. On the other hand, metastable states of an element have longer lifetimes, which are of the order of 10^{-3} seconds or higher [73]. The electronic levels considered are metastable states of titanium. Since the time step for movement and collisions used in the DSMC simulation is of the order of 10^{-7} seconds, the decaying of the excited states may be ignored in this time interval. This is consistent with the assumption allowing only the Boltzmann distribution to control the excitation of particles in the flow domain.

One parameter that is important in the collision mechanics calculations is the collision cross section. This parameter affects the probability of collision on the whole, and thus the energy exchanged between all energy modes of the particle. The current literature does not throw any light on the relations between the collision cross section of the ground state and those of various excited states of titanium atoms. Hence an assumption is made regarding this relationship. The collision cross sections of particles in any excited level is assumed to be the same as the ground state cross section. The hard sphere diameter of the titanium atom is taken to be 4 Å, which is very close to that of argon. This value is considered as the molecular weights of titanium and argon are very similar.

An analysis of the Saha equation (Eq. 3.7) leads to an assumption regarding the ionization in the flow domain. The Saha equation predicts the ionization fraction of a system at a certain temperature. This equation is represented as:

$$\frac{n_i}{n} = 2.4 \times 10^{21} \frac{T^{3/2}}{n_i} e^{-U_i/K_B T} \tag{3.7}$$

where n_i and n are the number densities of the ionized species and the total system. The ionization energy is represented by U_i. Assuming that $n_i \ll n$, this equation simplifies to:

$$n_i = \left[2.4 \times 10^{21} n T^{3/2} e^{-U_i/K_B T}\right]^{1/2} \tag{3.8}$$

For titanium, the ionization potential is $6.83eV$, which translates to $79228K$. Taking approximate values of n and T at the melt surface as $1 \times 10^{23}\#/m^3$ and $2000K$ respectively, we get:

$$n_i = 1.16 \times 10^{16}\#/m^3 = 1.16 \times 10^{-5}\% \tag{3.9}$$

Taking the values of n and Tat the substrate as $5 \times 10^{18}\#/m^3$ and $200K$ respectively, we get:

$$n_i = 1.46 \times 10^{13}\#/m^3 = 2.92 \times 10^{-4}\% \tag{3.10}$$

These ionization fractions are extremely low and are lower than the fractional excitation of many of the energy levels from Table 3.1 that are not considered in the simulation. This is entirely understandable as the highest energy level considered in Table 3.1 has an energy of approximately $35000K$ while the ionization potential is much higher. Thus, the ambient temperatures are too low to allow any of the electrons in the titanium atom to gain sufficient energy to escape from their orbits around the nucleus. On the basis of this analysis, it is assumed that ionization does not play any role in the flow physics in this case.

3.4.2 Ambient and inflow conditions

A particle can be introduced into a DSMC simulation in two ways. It can either be generated in the flow domain as a part of the ambient fluid or it can be generated at the inflow plane during the course of the simulation. In either case, the electronic level is assigned to the particle in the same way. When a particle is introduced into the simulation, it is assumed to be a part of an equilibrium distribution at the relevant temperature of the ambient or inflow condition. The partition function (given by the denominator of the Boltzmann relation) is calculated for this tem-

Table 3.2. Example of cumulative probabilities for electronic levels

Energy Level	0	1	2	3	4
Probability	0.1	0.3	0.2	0.3	0.1
Cumulative probability	0.1	0.4	0.6	0.9	1.0

perature and the value is stored, as it is a constant for the relevant flow condition. Further, the probability of occupation of every energy level is calculated. This is then converted to a cumulative probability table for each level j by summing the probabilities for levels 0 to j. For greater clarity, an illustrative example is presented in Table 3.2.

Next, a random number is generated and is checked against the table of cumulative probabilities to see which range it falls into. The energy level corresponding to that range is thus chosen and assigned as a particle property.

3.4.3 Wall collisions

Once a particle has been introduced into the simulation with an assigned electronic level and other flow properties, it can change its properties only through collisions. There are two kinds of collisions that a particle can undergo — wall collisions and particle-particle collisions. Collisions between particles are described in detail in Section 3.4.4.

When a particle collides with a wall, it may be reflected specularly or diffusely. Each wall has an accommodation coefficient in the range 0-1, that determines if the reflection of the wall is specular or diffuse. In the case of a specular reflection, the electronic energy of the particle is unchanged after reflection. In the case of a particle reflecting diffusely off a wall, the electronic mode of energy is assumed to equilibrate at the wall temperature. Hence the electronic levels can be assigned using exactly the same procedure used in the initialization of particles at the inflow or in an ambient condition. The electronic levels are assigned using the Boltzmann distribution at the wall temperature. Once the new level of the particle is assigned, the net energy transfer to the wall is calculated. The walls in the simulation can have a sticking coefficient in the range 0-1, which represents the probability of a particle sticking to the wall upon collision. When a particle sticks to the wall, it is removed from the simulation and the energy of the particle is added to the heat flux to the wall.

3.4.4 Collisional electronic energy exchange model

The Borgnakke–Larsen scheme [28] is a widely used approach for DSMC modeling of collisional transfer of energy between different modes. During every collision, the particles are assumed to be in local thermodynamic equilibrium and the particle properties are altered according to the probabilities from the appropriate Boltzmann distribution. The scheme employed here uses quantized energy levels to describe the electronic mode and follows the work of Bergemann and Boyd [11] on the quantized harmonic oscillator model of vibrational energy exchange. Other approaches include the work done by Anderson et al [3], where a method was developed for treating electronic and electronic–translational energy transfer.

The first step in generating an energy dependent probability is to convert the discrete Boltzmann distribution to a continuous one. This is achieved using the

Dirac Delta function. The Boltzmann relation can then be expressed as:

$$f_e \propto g_j e^{(-\epsilon_{e,j}/k_BT)}\delta(\epsilon_e - \epsilon_{e,j}) \tag{3.11}$$

During a collision, energy may be exchanged between the electronic mode of the colliding atoms, and the translational collision energy. The translational collision energy is weighted by the collision selection procedure, which in turn relies on the form of the intermolecular potential. Using the Variable Hard Sphere model of Bird [24], the collision-weighted equilibrium probability distribution for the translational energy of the pair of particles is:

$$f_t \propto \epsilon_t^{(3/2-\omega)} e^{(-\epsilon_t/k_BT)} \tag{3.12}$$

The probability distribution of the total energy is the product of the translational and electronic probability distributions.

$$f_c = f_t . f_e \tag{3.13}$$

Noting that the collision energy is the sum of the individual modes of energy :

$$\epsilon_c = \epsilon_t + \epsilon_e \tag{3.14}$$

Using Equations 3.11, 3.12 and 3.14 in Equation 3.13, we get:

$$f_c \propto g_j(\epsilon_c - \epsilon_e)^{(3/2-\omega)} e^{(-\epsilon_c/k_BT)}\delta(\epsilon_e - \epsilon_{e,j}) \tag{3.15}$$

For any particular collision, the temperature is taken to be constant for the distribution and hence the exponential term is a constant. The degeneracies of the levels act as a weighting function in the distribution. The easiest way to make the distribution dependent on only one variable — the electronic energy — is to consider the weighting separately. Hence the degeneracies of the energy levels are taken into account just before the acceptance-rejection procedure and a probability distribution can be defined based only on the electronic energy:

$$P = C(\epsilon_c - \epsilon_e)^{(3/2-\omega)}\delta(\epsilon_e - \epsilon_{e,j}) \tag{3.16}$$

Analyzing this, the magnitude of the probability depends only on the term $(\epsilon_c - \epsilon_e)^{(3/2-\omega)}$, which is a monotonically decreasing function of ϵ_e for the usual values of ω. Hence the probability is maximum when the particle is in its ground level. Taking $\epsilon_{e,j} = 0$, this maximum value is given by:

$$P_{max} = C\epsilon_c^{(3/2-\omega)} \tag{3.17}$$

Referring to this value of probability as P_{max} and normalizing, (Eq. 3.16) reduces to:

$$\frac{P}{P_{max}} = \left(1 - \frac{\epsilon_e}{\epsilon_c}\right)^{(3/2-\omega)} \delta(\epsilon_e - \epsilon_{e,j}) \tag{3.18}$$

This continuous distribution can then be converted easily to a discrete one by combining the delta function and the magnitude of the probability:

$$\frac{P}{P_{max}} = \left(1 - \frac{\epsilon_{e,j}}{\epsilon_c}\right)^{(3/2-\omega)} \tag{3.19}$$

The maximum permissible energy level is then determined by the truncation of the collision energy. The degeneracies are accounted for by selecting a state randomly from the total number of states included in the permissible energy levels. This provides the weighting that is required in the electronic energy distribution function. To achieve this, the number of allowed states for transition has to be calculated for the truncated collision energy. This is available from the number of allowed states stored for each electronic level during initialization. The values are simply the cumulative sums of the degeneracies for all levels up to the level under consideration. An example is presented in Table 3.3 for better clarity:

Table 3.3. Example of cumulative sum of degeneracies, as used in the modeling

Energy Level	0	1	2	3	4
Degeneracy	1	3	2	1	2
Allowed states	1	4	6	7	9

Since the maximum level for transition is known, the values of the allowed states can be normalized by the number of allowed states for the maximum level. This provides a range between 0 and 1 which is split into intervals corresponding to allowed levels. The width of the interval is directly dependent on the degeneracy of the corresponding level. Thus a random number is generated in the range [0,1] and the level corresponding to the chosen interval is selected for transition. The acceptance-rejection procedure is then applied to the selected state using the normalized probability obtained from (Eq. 3.19).

When a collision occurs, the particles are considered one at a time and their electronic transitions are handled sequentially. The first interaction considers the sum of the translational collision energy of the pair and the electronic energy of the first particle. As a result of this first interaction, the translational collision energy will change if the electronic energy of the first particle is changed. This updated value of the translational energy is then used together with the electronic energy of the second particle to determine the second interaction. For each interaction, the maximum permissible level for electronic transition is computed based on the total collision energy and a candidate post-collision energy is selected statistically. The acceptance-rejection procedure is applied to the probability of electronic transition for the selected level. If the transition is accepted, the collision energy is changed appropriately, taking into account the difference in the pre-collision and post-collision electronic energy of the first particle. A similar process is applied to the second particle. The resulting translational collision energy is then used for translational energy exchange. It may be noted that throughout these procedures, the total energy in the collision is conserved.

3.5 Electronic temperature

One important aspect of modeling electronic energy in the DSMC simulation is to provide a means to quantify its effect on the flow-field in a manner similar to other flow properties. Besides this, it is also important to compare the electronic and translational energy in the simulation in order to determine the mechanics of energy transfer between the two modes. In the DSMC simulation, the translational energy is represented by means of the translational temperature. Hence, an elegant solution to quantify electronic energy is to represent it using a temperature-like construct. This has the added advantage, as mentioned at the end of this section, of being an easy quantity to calculate from experimental measurements.

The macroscopic concept of temperature can be obtained from a microscopic viewpoint only when the system under consideration is in equilibrium. For example, the translational temperature of a gas is a measure of the spread of the Maxwellian distribution of velocities, and the Maxwellian distribution exists only in a system in equilibrium. However, the system may be in non-equilibrium in many cases, which makes the resolution of many macroscopic flow properties impossible. An engineering assumption of equilibrium is often made in DSMC simulations to resolve these properties, and a similar assumption is made in the case of electronic temperature.

For a system under equilibrium at an ambient temperature, the distribution of particles in various electronic levels follows the Boltzmann distribution (Eq. 3.1) at that temperature. Using the assumption of equilibrium, the Boltzmann distribution can then be used to provide a definition for electronic temperature. In the simulations, it is possible to calculate the fractional excitation to various electronic levels at any point in the flowfield. If we consider a hypothetical system in equilibrium at some temperature, it is again possible to calculate the fractional excitations to various levels in this theoretical system. If these fractional excitations in the theoretical system can be matched to their corresponding simulated values, then the local flowfield in the simulations may be considered to be represented by the theoretical system. In this case, the local electronic temperature of the flowfield is the ambient temperature of the theoretical equilibrium system. The electronic temperature of a simulated system is thus defined to be the value of the ambient temperature of an equivalent system in equilibrium that produces the same fractional excitation to various electronic levels as those calculated in the simulated system.

In order to obtain an analytical expression for electronic temperature, it is necessary to take some statistical issues into consideration. The Boltzmann distribution predicts that the fractional excitation of electronic states decays exponentially with the energy of the state. This is represented by a straight line with negative slope when the fractional excitation is plotted on a semi-log scale against the energy of the state, as seen in Figure 3.4. The simulated system undergoes statistical fluctuations as well as deviations from equilibrium. Under these con-

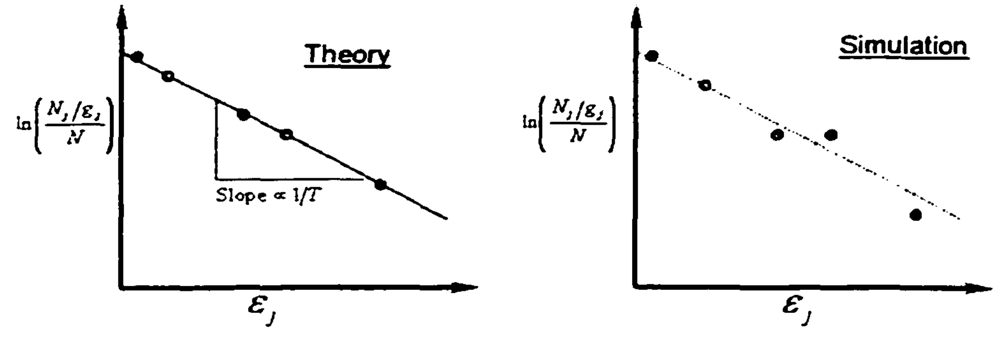

Figure 3.4. Examples of theoretical and simulated population level distributions of titanium

ditions, a corresponding plot of the fractional excitation of the simulated system may not fall on a straight line (Fig. 3.4). This makes it difficult to compare it to a theoretical distribution, as suggested in the definition of electronic temperature. It may be observed that the fractional excitation of the ground state is always the highest among the energy states, and that of the first excited state is lower than only this value. Hence, these two states are likely to be the most populated states in the statistical flowfield, thus making them the most accurate states statistically. Hence a straight line on the semi-log plot that includes the ground state and the first excited state may be considered for comparison with the theoretical system, as seen in Figure 3.4.

Considering the fractional excitation of the ground state by substituting $j = 0$ in the Boltzmann distribution (Eq. 3.1), we get:

$$\frac{N_0}{N} = \frac{g_0 e^{-\epsilon_0/k_B T}}{\sum_j g_j e^{-\epsilon_j/k_B T}} \tag{3.20}$$

Similarly, an expression may be obtained for the fractional excitation of the first excited state:

$$\frac{N_1}{N} = \frac{g_1 e^{-\epsilon_1/k_B T}}{\sum\limits_j g_j e^{-\epsilon_j/k_B T}} \tag{3.21}$$

Dividing Equation 3.20 by Equation 3.21, we get:

$$\frac{N_0}{N_1} = \frac{g_0}{g_1} e^{\epsilon_1/k_B T} \tag{3.22}$$

as ϵ_0 is zero by definition. This expression then simplifies to:

$$T_e = \frac{\epsilon_1/k_B}{\ln\left(\frac{g_1/N_1}{g_0/N_0}\right)} \tag{3.23}$$

This definition of electronic temperature is extremely sensitive to the populations of the ground level and the first excited level due to the logarithmic factor in the denominator. Thus extensive sampling of these two electronic levels needs to carried out in the simulation.

This definition of an electronic temperature is a very useful tool to compare the relative amounts of translational and electronic energy. However, it has its limitations due to the mathematical sensitivity and the assumption of equilibrium. Thus this definition is more of a tool for qualitative comparison than a quantitative one. It is also extremely useful for comparison with the laser absorption data from the experimental facility where the measured fractional excitations of the ground and first excited electronic levels allow the electronic temperature to be calculated in the same manner.

Chapter 4

Titanium Vapor Deposition Simulations

The numerical simulations of the Experimental Test Facility (ETF) constitute the computational part of a joint effort with Lawrence Livermore National Laboratories to study the process of vapor deposition. The computational work addresses various aspects of modeling the physical system. A primary area of focus was on the importance of electronic energy on the simulations. The first set of results presented in this chapter detail the comparisons between simulations where electronic energy is included among and excluded from the energy modes of a particle. The next section describes the phenomenon of backscattering of particles into the melt, and the importance of its modeling for accurate computational results. Further comparisons are made between computationally calculated and experimentally measured deposition profiles in order to link the computational and experimental aspects of the study. Finally, sensitivity analyses are performed on certain physical parameters used in the model to validate the assumption made in their regard.

4.1 Inflow profiles

The numerical simulations are carried out using a DSMC code called MONACO [51], which is discussed in Section 2.2. The simulations are performed on a R4400 processor and involve more than 200,000 particles, using a grid (Figure 4.1) with

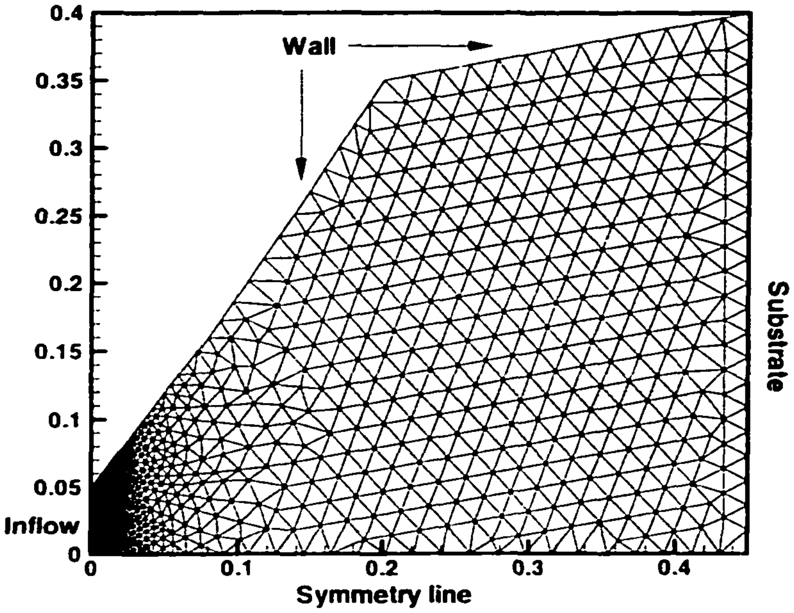

Figure 4.1. Grid used in simulations of the flow domain. All dimensions in m

nearly 2000 cells.

The flow domain is modeled using a refined, unstructured, triangulated grid, shown in Fig. 4.1. The mesh is generated using an algorithm called the Advancing Front Method (AFM) [95],[87],[109]. The cells in the grid are scaled to the order of the local mean free path of particles. The vaporization from the molten pool is modeled through multiple inflow conditions, as described later in this section.

In the real system, the vaporization of titanium atoms does not occur at a uniform rate across the surface of the molten pool. The evaporation profiles were obtained through a computational model developed at LLNL, in collaboration with the University of Washington [40]. This model used finite element methodology to model the evaporation from the molten pool. The modeling used a deformable mesh to determine the shape of the pool surface and the transport phenomena occurring within the melt. The results from this study were used as input to the

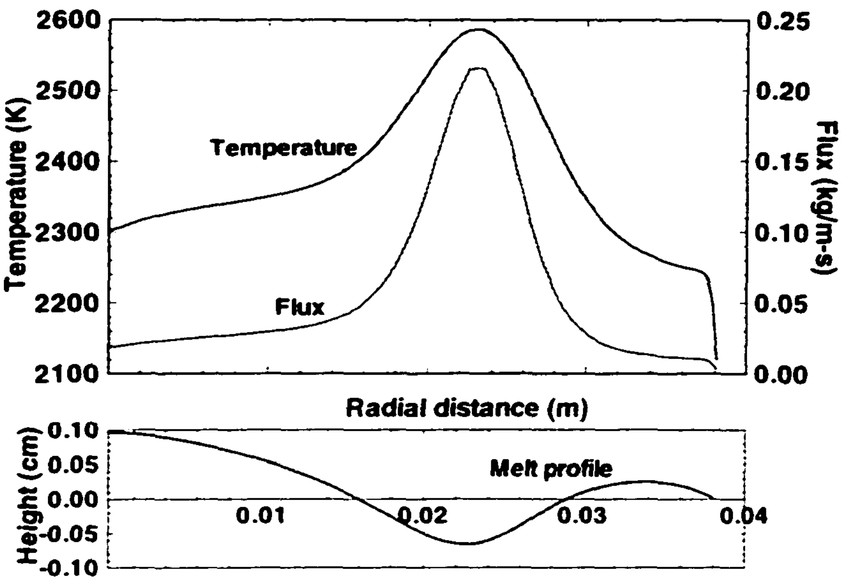

Figure 4.2. Inflow profiles of the temperature, flux and surface used in the DSMC simulation

DSMC simulations described in this chapter. The temperature and flux distributions across the melt surface, as well as the profile of the surface, are shown in Fig. 4.2.

The electron beam traverses the surface of the ingot in a circular path at a distance of 2.33 cm from the axis. This causes intense heating of the material at this point, as shown by the peak in the temperature profile. Various transport phenomena occur within the molten pool. The heat transfer within the liquid metal, primarily due to radiation and convection, creates the temperature profile shown. In the case of evaporating sources, the specific evaporation rate can be expressed [118] as function of temperature:

$$a_v = \alpha.4.4 \times 10^{-4} K_1 \left(\frac{M}{T_v}\right)^{1/2} e^{-K_2/T_v} \tag{4.1}$$

where a_v is the specific evaporation rate in $gcm^{-2}s_{-1}$, α is the evaporation coefficient, M is the molecular weight of the evaporant, T_v is the source temperature of the evaporant in degrees Kelvin, K_1 and K_2 are matter constants that define the relationship of the saturated vapor pressure to the temperature for the element in question. The vaporization is thus exponentially proportional to the source temperature. The resulting vapor source is spatially very peaked around the location where the electron beam strikes the ingot. The process of evaporation occurs through the breaking of the surface bonds between the evaporating particle and the melt pool. As the particles leave the melt surface, they impart momentum to the surface in the direction opposite to their motion. This momentum transfer results in a pressure and shear stress distribution across the melt surface due to the outgoing particles. The momentum transfer thus causes a deformation in the shape of the surface, with a depression forming at the point where the maximum momentum transfer occurs. Since this occurs at the points of highest vaporization, the depression occurs at the location where the beam hits the surface. Hence the electron beam acts as a medium of energy transfer to the metal. Since the mass of an electron is five orders of magnitude smaller than that of a titanium atom, momentum transfer between the electrons in the beam and the liquid metal is negligible. The temperature and flux profiles are shown in the upper half of Figure 4.2. The lower half of this figure shows an exaggerated view of the surface profile for visual clarity, and this can be noted by the difference in the scales on the axes.

This data is input to the DSMC simulation by the use of multiple inflow conditions. The surface shape is incorporated into the grid by sub-dividing the profile into piecewise linear components and using these linear segments as the inflow side in different grid cells, as seen in Figure 4.3. Each of these cells is assigned a different inflow condition so as to capture the flux and temperature profiles. In this study, the electron beam is modeled as a ring source, though in reality it traverses the

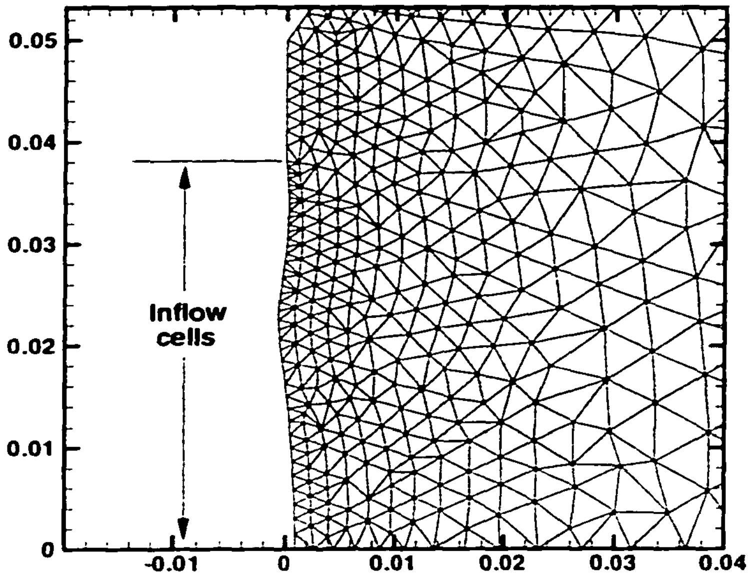

Figure 4.3. Detail of the inflow cells in the computational grid

surface at a frequency on the order of a few kilohertz. However, the primary effect of the electron beam is energy transfer, with the resulting temperature causing the vaporization and thus the surface shape, as described in the previous paragraph. Since the electron beam does not provide momentum transfer to affect the surface profile, and since significant heat transfer effects are likely to occur at a larger timescale than the scanning frequency of the electron beam, the energy transfer at a particular location on the path of the beam may be regarded as nearly constant. The temperature, flux and surface profiles shown in Figure 4.2 may thus be assumed to remain constant with time. The molten surface is thus considered to be an axisymmetric source. The flow domain is considered to be axisymmetric too. The walls of the ETF are assumed to be perfectly sticking for titanium atoms.

4.2 Comparison of Flowfield Properties

The results presented in this study are obtained from two simulations. Both simulations are carried out using titanium atoms as the lone species. One includes electronic energy, with the consideration of the first seven energy levels of titanium, given in Table 4.1. The other simulation includes only the ground state, which has an electronic energy of 0 K. Thus, there was no electronic energy contained in the flow domain in this simulation, eliminating any effects of this mode on the flow. It must be noted that the total energy content of the flow in these simulations is different. Figures 4.4, 4.6 and 4.9 show comparisons between the flowfield contours from the two simulations, thus illustrating the effect of electronic energy on the flow.

The flow in the ETF is characterized by extremely rapid expansion. Figure 4.4 shows a comparison between the number density contours in the cases with and without electronic energy. In both cases, the density drops through three orders of magnitude, from $O(10^{21})$ to $O(10^{18})$, due to expansion. For clarity, the number density in the two cases is plotted along the axis of symmetry in Figure 4.5. The flow shows a slightly higher degree of expansion when electronic energy is considered, as seen by the lower densities in the flow domain.

The higher degree of expansion is also seen in Figure 4.6. The contours shown here correspond to the absolute velocity. The collisions in the flow convert the thermal energy into macroscopic flow velocity, thus causing the acceleration seen in the absolute velocity contours. The off-axis velocity peaks in these contours are due to the off-axis source from which expansion occurs. These peaks are pronounced as the atoms vaporize off the melt surface with no directed velocity. Hence the

Table 4.1. Computational energy levels of titanium

Energy Level	Energy (K)	Degeneracy
1	0.00	5
2	244.79	7
3	556.65	9
4	9612.17	35
5	10439.89	5
6	12245.26	9
7	16761.80	21

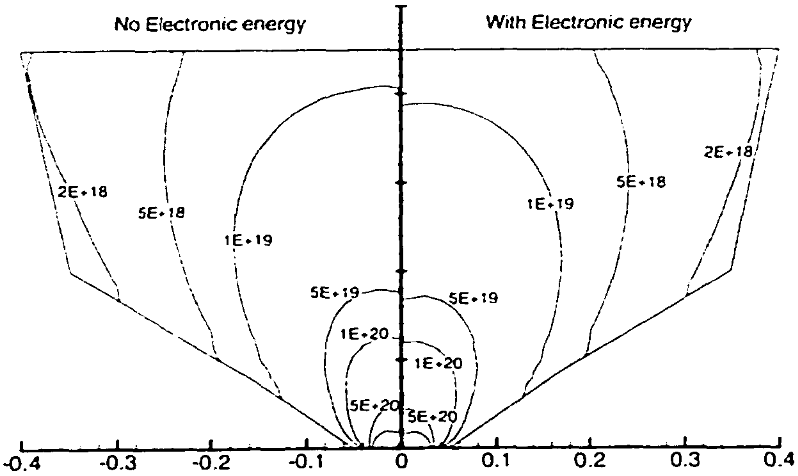

Figure 4.4. Contours of number density ($\#/m^3$) for simulations including (right) and excluding (left) electronic energy

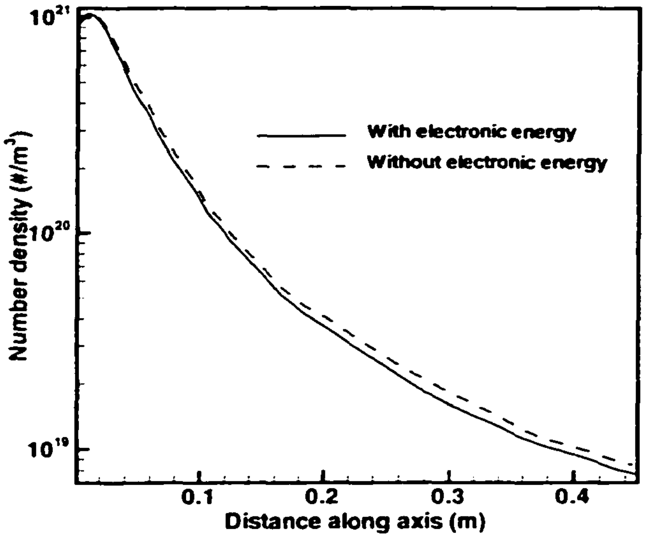

Figure 4.5. Number density along the axis of symmetry

axial and radial components increase at comparable rates causing the absolute velocity profiles shown in Fig. 4.6. The atoms vaporize off the surface and expand to velocities above 1300 m/s. The expansion is seen to occur to a higher degree when electronic energy is considered. In this case, the maximum velocity achieved is nearly 1400 m/s, which is an increase of 80 m/s (6%) over the corresponding value for the case without electronic energy.

The velocity profiles in both cases show a very sharp increase in the region just above the melt. This can be treated as a Knudsen layer that lies just above the source. Knight [81] has analyzed the Knudsen layer as a region where translational equilibrium is approached after evaporation from a source. This arises from the fact that the velocity of the evaporating particles normal to the source form a part of a distribution function that consists of a half-range Maxwellian with a zero mean velocity. The distribution functions of velocities tangential to the inflow surface consist of full-range Maxwellians with zero mean velocities. Immediately after a

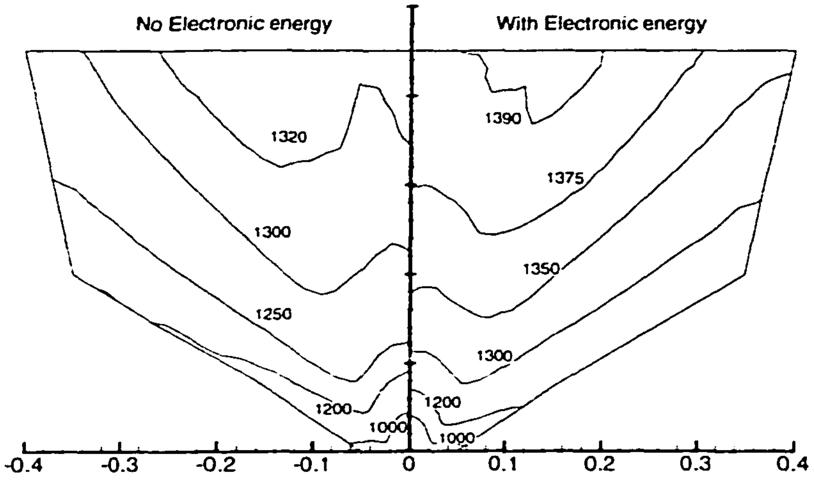

Figure 4.6. Contours of absolute velocity (m/s) for the two cases

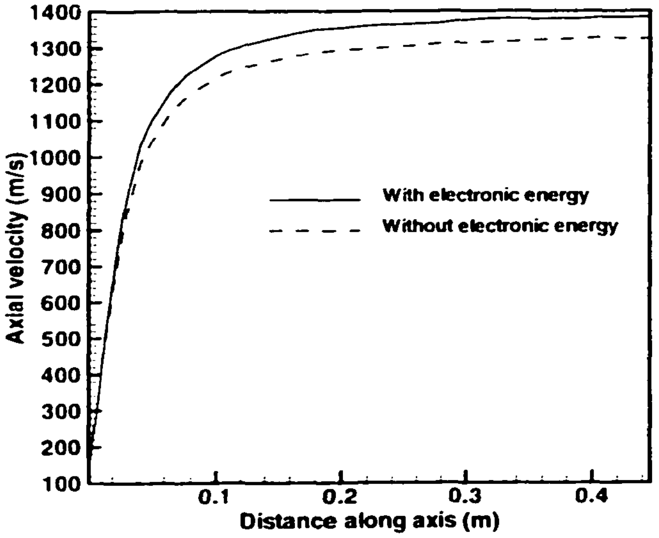

Figure 4.7. Axial velocity along the axis of symmetry

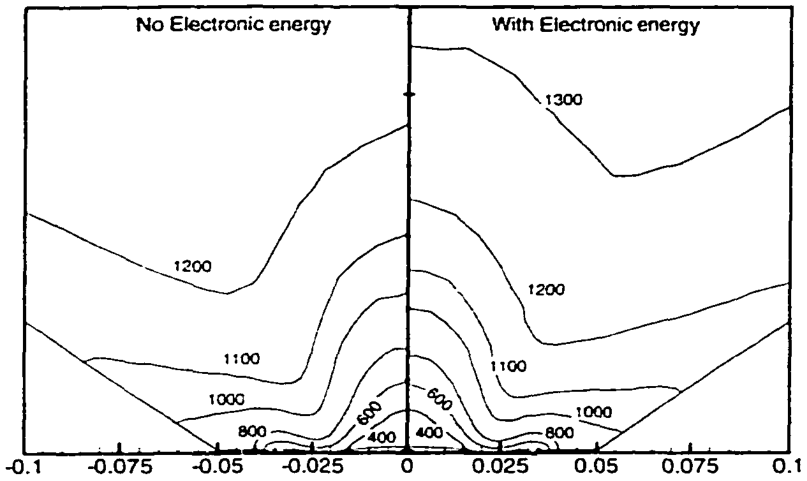

Figure 4.8. Absolute velocity in the Knudsen layer

particle leaves the melt surface, it undergoes collisions that tend to alter the distribution function towards translational equilibrium. This adjusts the distribution function of the normal velocity to a larger finite value, thus creating the Knudsen layer. In reference [80], the Knudsen layer is treated as a gas-dynamic discontinuity. A close-up view of the flow (Figure 4.8) above the melt surface shows that the velocity immediately above the melt is finite, which is consistent with Knight's prediction of a Knudsen layer.

As seen in Figure 4.7, the axial velocity along the axis of symmetry is higher when electronic energy is considered. After a sharp increase in velocity in the Knudsen layer, the profiles tend toward an asymptotic value in both cases. This occurs due to a lack of enough equilibrating collisions in the flowfield. The difference between the profiles is a measure of the electronic energy converted into kinetic energy. In the simulation, the maximum velocity attained is governed by the lack of collisions in the flow, rather than on the perfect isentropic expansion discussed in Section 3.2.

Analyzing the contours of translational temperature (Fig. 4.9), it is seen that the translational temperatures are higher in the flow domain when electronic energy is considered. This is an indicator of the higher energy content of the simulation with electronic energy. Figure 4.10 shows that the translational temperature along the axis seems to approach a constant value, or "freeze". Once again, this is due to the lack of enough collisions that allow the flow to expand further.

As expansion occurs, the translational temperature drops in both cases. When electronic energy is present, the electronic temperature also decreases as the expansion takes place. This is indicative of a higher proportion of the particles being in the lower excited states after expansion, or a reduction in the overall excitation of the flow. The total energy content in the electronic mode is thus reduced and there is a significant amount of energy transferred from the electronic to the translational mode. This is the mechanism through which the higher energy content manifests itself as higher translational temperatures in the simulation with electronic energy. This is also manifested in the velocity contours due to conversion of this energy into kinetic energy.

A comparison is made between results obtained from the simulation and experimental measurements. These measurements are taken using laser absorption spectra of the vapor in the ETF. A discussion of laser absorption spectroscopy and the measurement of flow properties from the measured spectra is presented in Chapter 5. Table 4.2 shows good agreement between the measured and computed values of the velocity of the vapor. The simulation including electronic energy shows better agreement with the experiment than the other case. How-

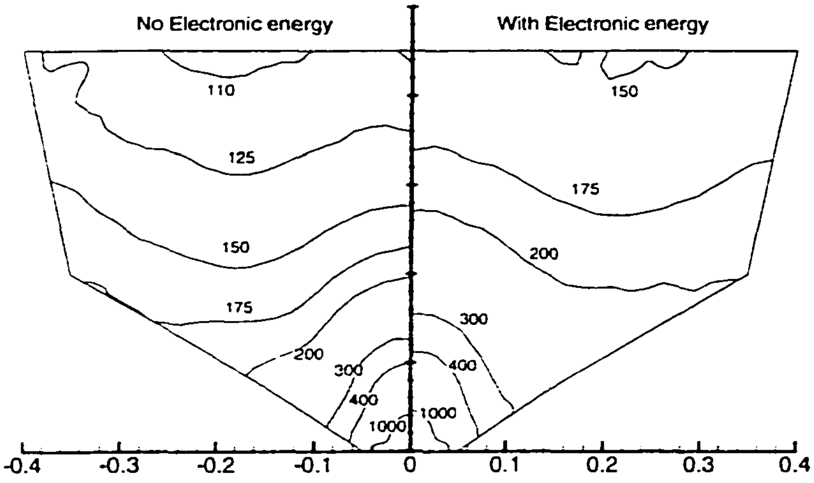

Figure 4.9. Contours of translational temperature (K) for the two cases

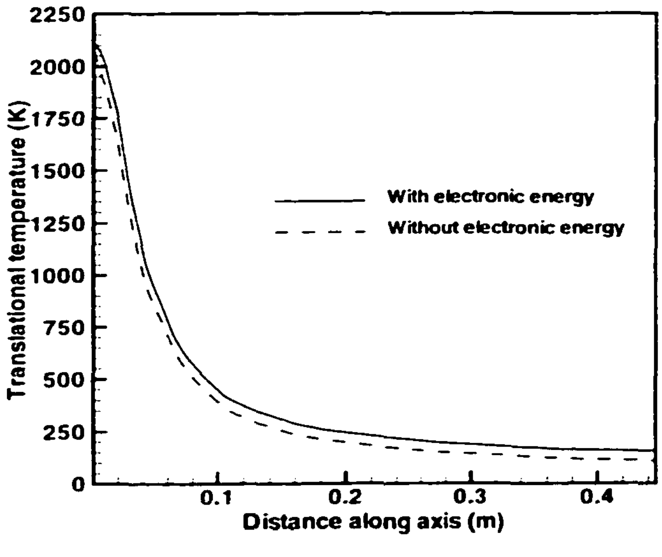

Figure 4.10. Translational temperature along the axis of symmetry

Table 4.2. Comparison between simulations and experimental measurements

Flowfield property	Experiment	Simulation With EE	Simulation Without EE
V (m/s)	1400 ± 10	1393	1326
$T_\perp$ (K)	160 ± 10	85	60
T_i (K)	190 ± 10	280	-

ever, both simulations compute values for the perpendicular temperature that are significantly lower than the experimental measurement. The simulation including electronic energy has the higher of these values because of the net transfer of energy from the electronic to the translational mode. In this case, the computed internal (i.e. electronic) temperature is higher than the measured value. This seems to indicate that the rate of transfer of energy between the two energy modes is not captured adequately in the simulations. This behavior is related to the collision rate and hence, the collision cross section, which could vary depending on the excited state of the atom. In this study, the cross sections for all electronic states are taken to be equal to the ground state cross section, for want of better data. This comparison indicates that the simulation including electronic energy gives a better prediction of the measured flow-properties than the corresponding case that excludes electronic energy.

The expanding flow shows a high degree of non-equilibrium. In order to demonstrate this, Fig. 4.11 shows a comparison of the electronic and translational temperatures in the flow domain. It must be noted that both contour plots in this figure are results from the simulation that includes electronic energy. The flow expands from a collisional regime near the molten pool to a near free molecular

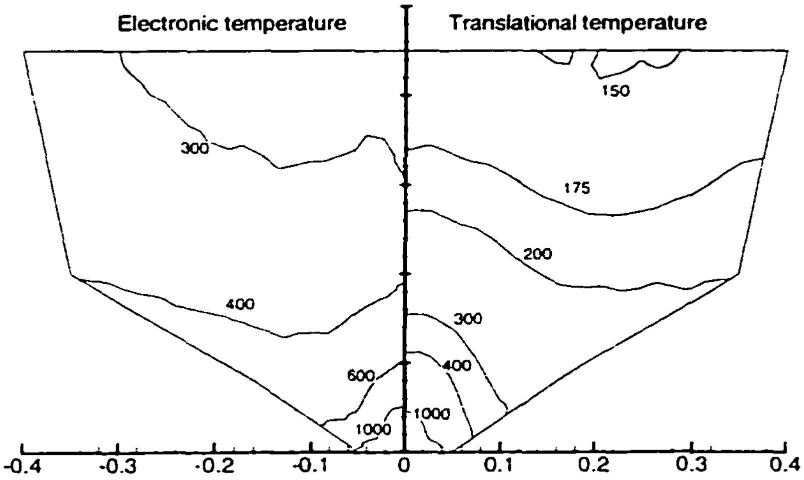

Figure 4.11. Non-equilibrium between the energy modes: Contours of T_e and $T_{\|}$

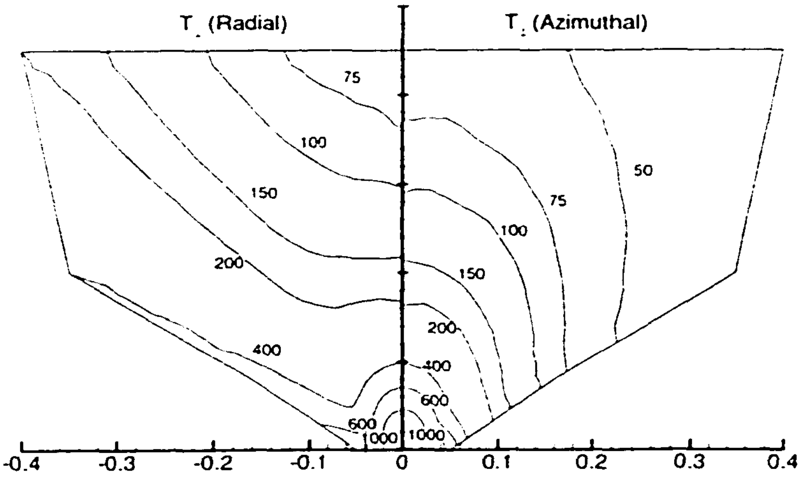

Figure 4.12. Non-equilibrium between the energy modes: Contours of radial and azimuthal components of translational temperature

region near the substrate. The corresponding Knudsen numbers based on chamber radius are 0.025 and 0.5 respectively. As the expansion takes place, there are fewer collisions, leading to non-equilibrium effects. The translational temperatures measured along the directions perpendicular and parallel to the axis are defined as $T_\perp$ and $T_\|$ respectively. It is the perpendicular component of the temperature that was measured by laser absorption spectroscopy. Under equilibrium, the Maxwellian distribution is spherically symmetric and the components of the translational temperature are equal in all the coordinate directions. In the absence of enough collisions, the velocity distribution may deviate from the equilibrium Maxwellian form. In this case, it is not possible to apply the equilibrium concept of a temperature. Fitting the sampled data in the simulations and the spectroscopic measurements to a Maxwellian distribution may lead to different values for the temperature in different coordinate directions. This is an indication of non-equilibrium conditions in the flow. In the flow, $T_\perp$ decreases due to the increasing area in the geometry of the flow domain. The equilibration of $T_\perp$ and $T_\|$ occurs through collisions. As the flow becomes increasingly free molecular, a degree of non-equilibrium arises between these two components of translational temperature (Fig. 4.12). The equilibration of the electronic energy to the translational energy also occurs through collisions and hence non-equilibrium is also seen between this mode and the translational mode.

Figures 4.13 and 4.14 show the variation of the three components of the translational temperature for the simulations that include and exclude electronic energy respectively. In both cases, the perpendicular temperature components are different from the parallel temperature, which is indicative of non-equilibrium. Near the melt, the parallel temperature is lower than the melt temperature due to the Knud-

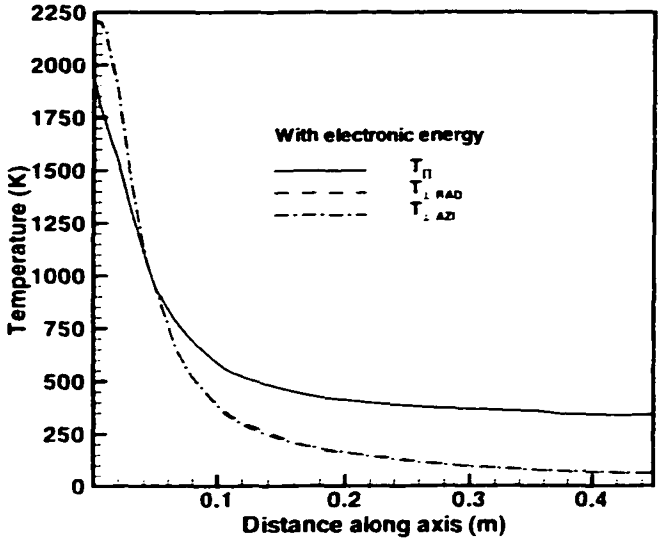

Figure 4.13. Translational non-equilibrium along the axis — Simulation with electronic energy

sen layer. The perpendicular mode quickly equilibrates with this mode through collisions. However, the flow is never really in translational equilibrium and this fits in very well with predictions made by Knight [81]. Knight notes that the evaporating flow is expected to be subsonic and should accelerate to supersonic speeds. The acceleration of the subsonic flow at the surface is accompanied by an increase in entropy, and hence the flow is generally not in translational equilibrium. The results from the simulation agree extremely well with Knight's theory.

An examination of Figures 4.6 and 4.9 shows that the vapor expands to a maximum velocity of 1326 m/s and a parallel temperature of 232 K in the case without electronic energy. For the case where electronic energy is included, the corresponding values are 1394 m/s and 311 K respectively. Assuming a source temperature of 2500 K and the final temperature after expansion as detailed above, the post-

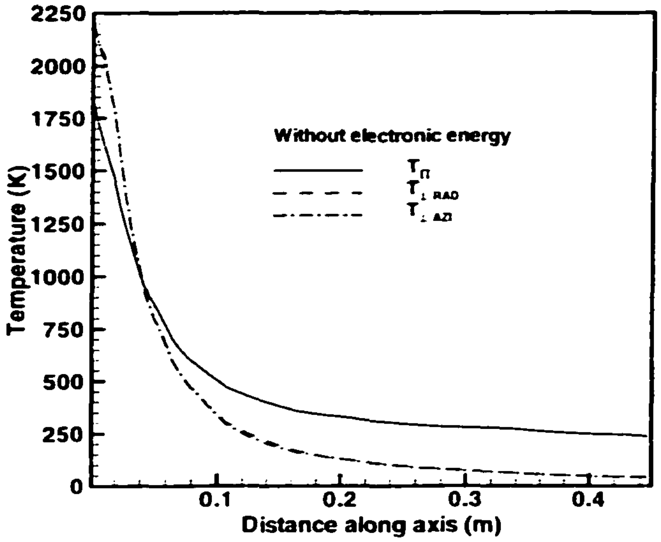

Figure 4.14. Translational non-equilibrium along the axis — Simulation without electronic energy

expansion velocities are calculated from isentropic theory to be 1402 and 1502 m/s for the cases excluding and including electronic energy, respectively. The lower values calculated in the simulations are indicative of a number of factors. First, the non-equilibrium nature of the flow does not allow for complete expansion as calculated by the isentropic theory. The flow expands from the near-continuum to the free molecular regime. Thus collisions between the particles become increasingly rare and this does not allow for expansion in the isentropic sense. Again, the difference between the theoretical values for the post-expansion velocities of the two cases is nearly 100 m/s whereas the corresponding difference from the simulations is approximately 80 m/s. This seems to indicate that the electronic energy in the simulations is not being converted into kinetic energy as much as theory predicts, which is a consequence of the non-equilibrium effect. This may also be a consequence of the fact that the actual collision cross section may be larger than the corresponding value with the consideration of only the translational mode. Also, the melt surface has a temperature profile associated with it where the temperatures vary by a few hundred degrees. The theoretically calculated values do not account for this. The actual source temperature required in these calculations is not obvious, thus making the calculations approximate. The order of magnitude of the velocities predicted in each case by theory and simulations is the same. This is also true of the difference between the velocities for the two cases, as predicted by theory and simulations. The comparison between theory and simulation thus shows reasonable agreement while emphasizing the importance of the simulations in capturing the physics of the flow.

4.3 The Backscatter Phenomenon

The backscattering of particles is a phenomenon that occurs in the highly collisional area above the evaporating surface. As indicated in Figure 4.15, after a collision, some particles attain velocity components that direct them back towards the melt. When the particles strike the melt surface, they are re-absorbed into the liquid pool. This causes a reduction in the net evaporating flux. In this study, it is assumed that all particles that are backscattered into the melt are reabsorbed into the liquid pool. This is in accordance with Williams' [133] claim that this is generally the case for metals with monoatomic vapor, as is the case here with titanium.

The calculation of the backscatter into the melt is an important issue in this study. In the experiment, the rate of vaporization of titanium into the ETF was

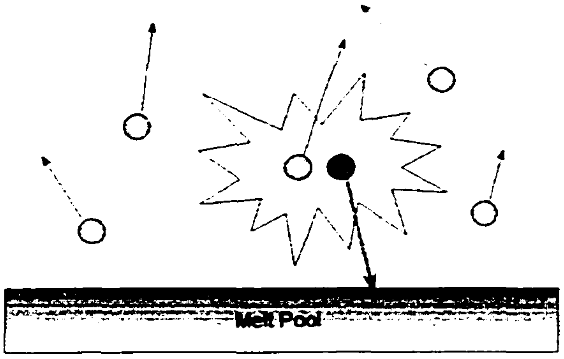

Figure 4.15. Schematic of the backscatter phenomenon

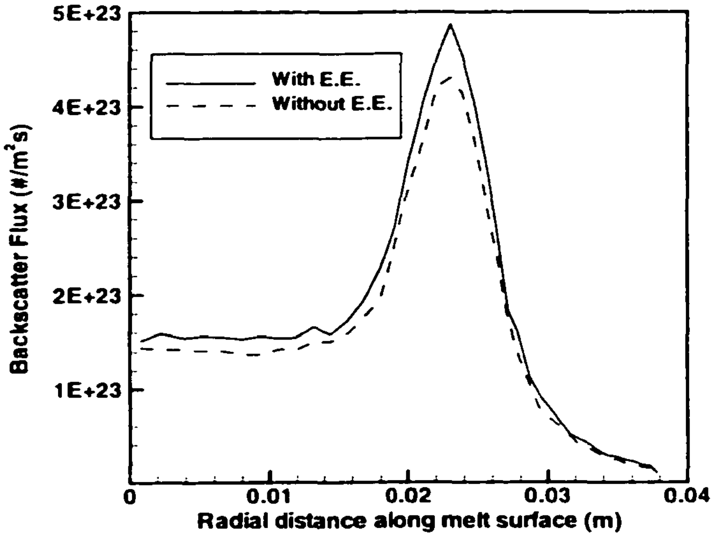

Figure 4.16. Backscatter flux to the melt

measured from the feed rate of the titanium ingot. The ingot itself was modeled in an independent study, as mentioned earlier [40]. The vaporization rate provided by that study matched the experimental value without considering any backscatter to the melt. The profiles computed from that study were input to the DSMC simulation, in which particles were scattered back to the melt. This caused a reduction in the net inflow rate, which did not match the experimental value. Hence the inflow profiles are corrected by the amount of backscatter flux to simulate the same conditions as the experiment. This information is also important for the modeling of the pool itself as the backscattering vapor transfers momentum and energy to the pool, thus changing its properties. Figure 4.16 shows the flux of particles scattering back into the melt. The profiles show that the backscatter fraction is a significant part of the inflow profile considered, which re-iterates the importance of modeling this phenomenon. The amount of backscatter flux is higher when electronic energy is considered, and the value is 17.40% of the inflow flux. In comparison, this value is only 15.98% when no electronic energy is considered. The difference in these two values can be explained by the fact that in the former case, the vapor has a higher energy content. Due to the collisional nature of this flow region, there is a transfer of energy between the electronic and translational modes. As expansion takes place, this results in a net transfer of energy into the translational mode. This causes more energy to be present in the translational mode as compared to the case without electronic energy. This is manifested as higher temperatures and velocities in the former case. The number of collisions in the region is proportional to the relative velocity between atoms, which is higher when the translational energy is higher. The fraction of particles scattered back in to the melt is dependent on the number of collisions in the flow region and

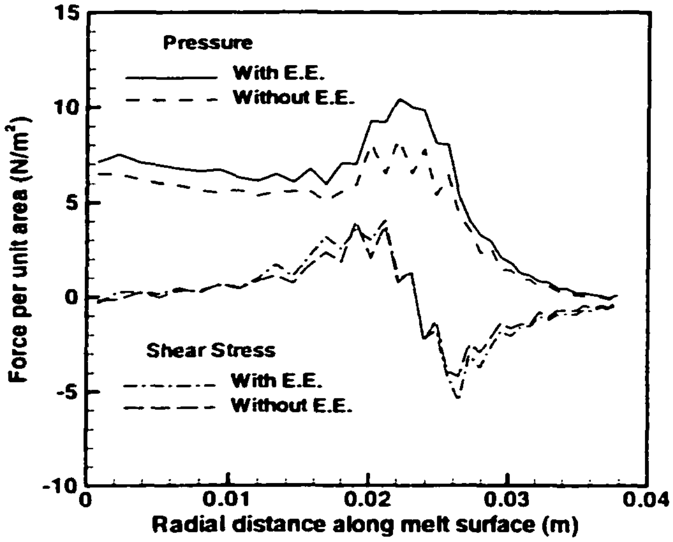

Figure 4.17. Pressure and shear stress exerted on the melt by backscattering particles

hence the case with electronic energy has a higher backscatter fraction than the corresponding case without electronic energy.

Figure 4.17 shows the pressure and the shear stress exerted by the backscattering particles on the melt surface. It is clear that the particles exert more pressure and shear stress on the surface when electronic energy is included in the simulation. The pressure is greatest at the location where the evaporating flux is the highest, since this is also where the highest backscatter flux is present. This would contribute further to the depression of the surface at this point. Figure 4.18 shows the energy flux carried by the backscattering particles into the liquid pool. The particles with electronic energy carry more energy back into the melt due to the higher backscatter fraction as well as the additional mode of energy considered in this case. This data would prove very useful to a comprehensive model of the

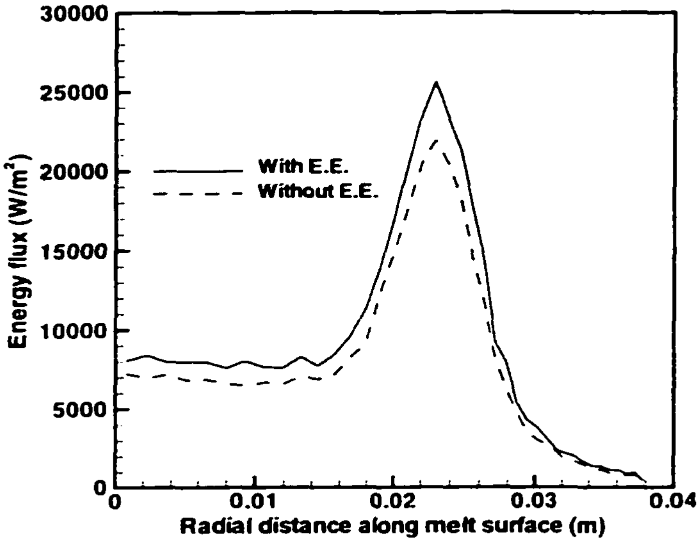

Figure 4.18. Energy flux carried to the melt by backscattering particles

liquid melt pool, such as the finite element model [40] that provided the inflow flux, temperature and surface shape profiles described in Figure 4.2.

4.4 Surface Deposition

The experiments at LLNL yielded measurements of the thickness of material deposited on the substrate and this was used for comparison with the results of the DSMC simulations (Fig. 4.19). The simulation results yield the vapor flux at the substrate. The time of operation of the ETF is known, and the deposition profile was measured during the experiment after an operating time of nearly two hours. The computational flux can thus be converted to a deposition thickness using the operating time, the molecular weight of titanium and the density of the deposited

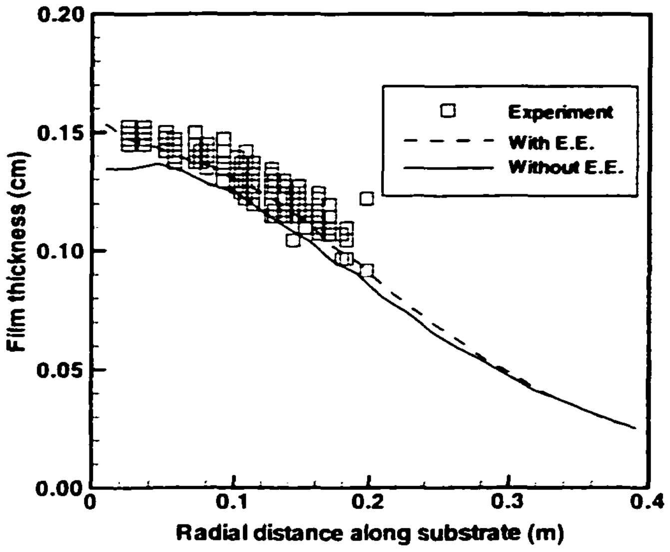

Figure 4.19. Deposition thickness on the substrate: Comparison between computed values and experimental measurements

material. The computed deposition profile shows very good agreement with the experimental measurements. The number density along the substrate (Fig. 4.20) is lower when electronic energy is considered due to the higher expansion in the flow. The greater degree of expansion also causes the flow velocity to be higher at the substrate (Fig. 4.21). The combined effect of the number density and the flow velocity the flux, and thus the computed deposition thickness. The thickness of the film deposited is lower when electronic energy is considered. This is explained by the fact that the translational temperature is higher, both along the substrate (Fig. 4.22) and in the flow domain for this case, leading to an increased amount of radial expansion. The higher flow energy content in the simulation with electronic energy causes a higher translational temperature at the substrate than the other case. As more of the translational energy is converted to kinetic energy, the axial

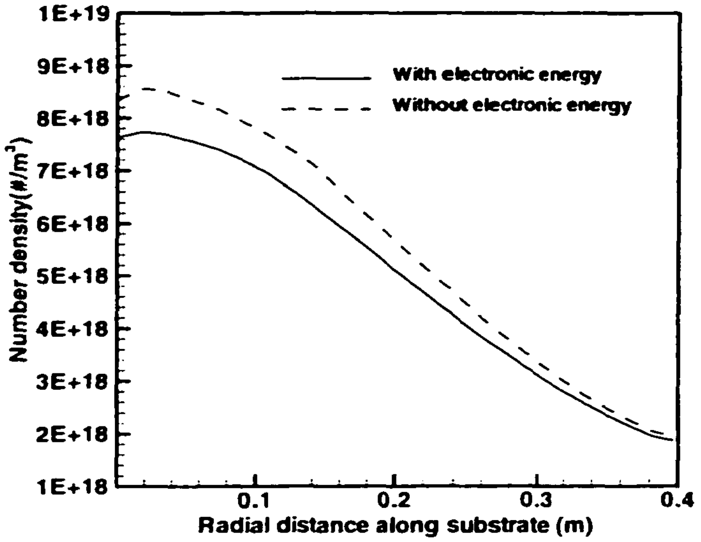

Figure 4.20. Number density along the substrate

and radial velocities at the substrate are higher when electronic energy is considered (Figures 4.23 and 4.24). As seen in Section 4.2, this is true of the entire flow domain. Since the radial expansion is greater when electronic energy is included, a greater part of the flow is directed towards the walls in this case. This is confirmed by looking at the flux to the walls of the flow domain (Fig. 4.25). For purposes of qualitative comparison, the thickness of the film deposited on the wall is plotted against the radial distance of the wall from the axis, with the shape of the wall being depicted for clarity. It is seen that the wall flux, which is proportional to the deposited film thickness, is greater when electronic energy is considered. This explains the lower deposition to the substrate in this case. The close agreement between the computed values and the experimental measurements also suggests that assuming a perfectly sticking substrate, with a sticking coefficient of 1, is reasonable.

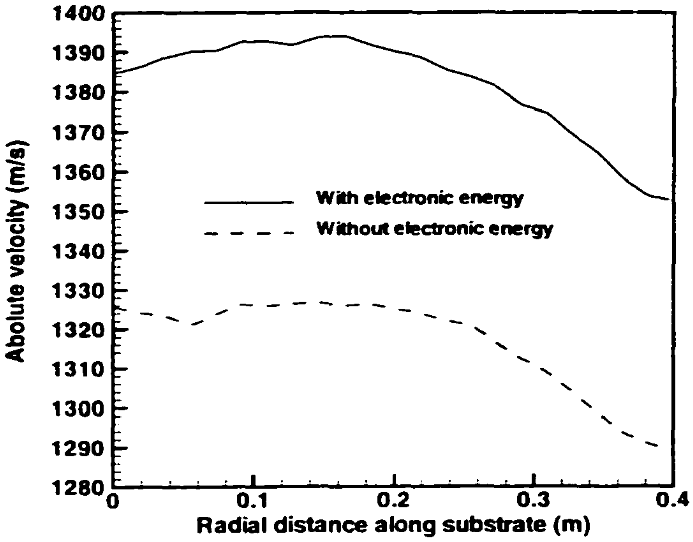

Figure 4.21. Absolute velocity along the substrate

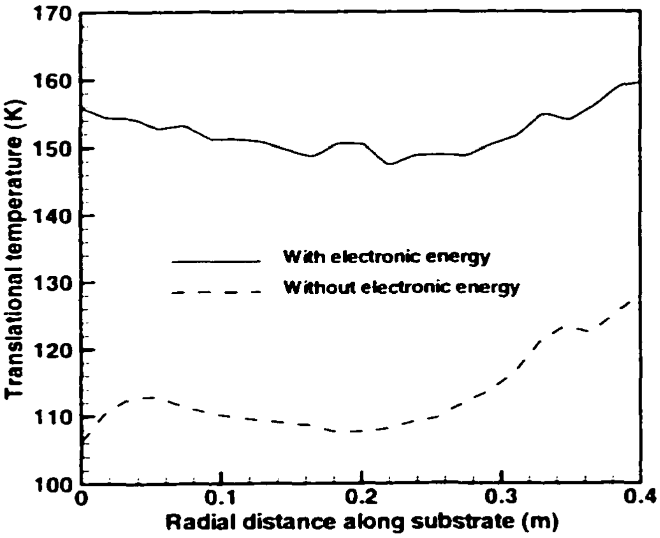

Figure 4.22. Translational temperature along the substrate

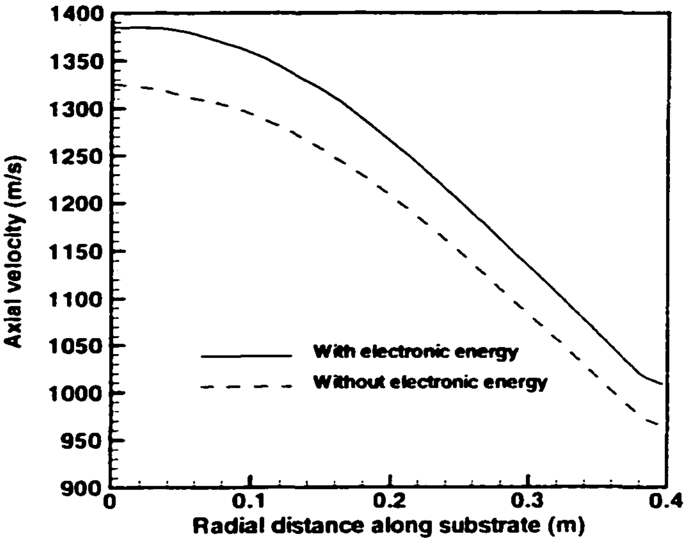

Figure 4.23. Axial velocity along the substrate

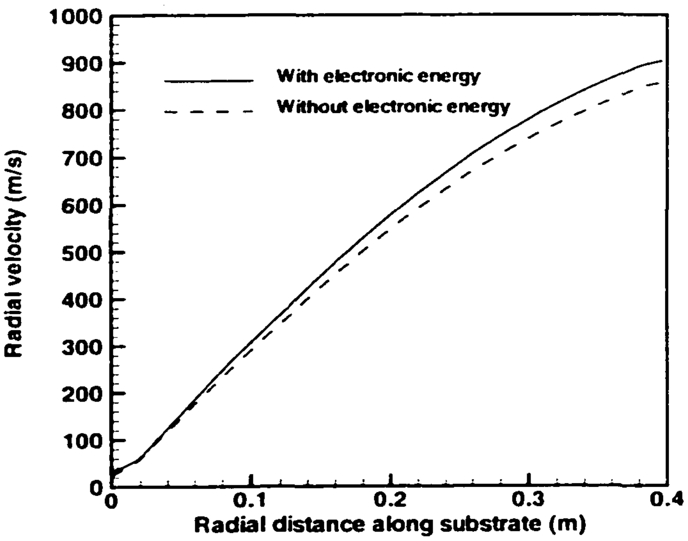

Figure 4.24. Radial velocity along the substrate

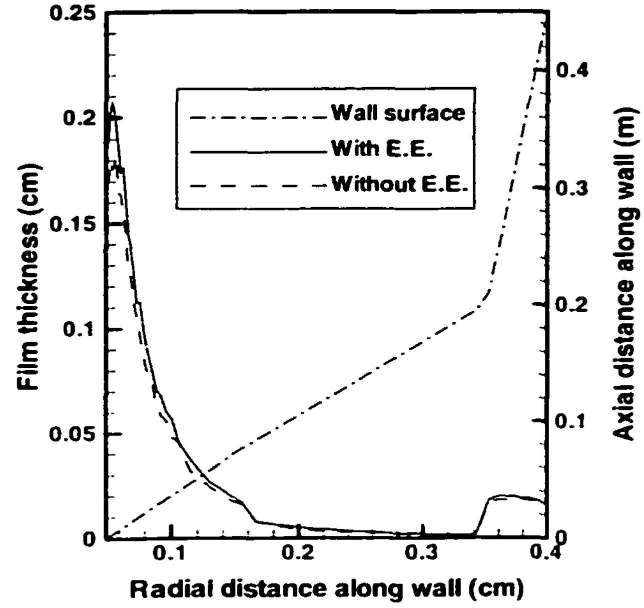

Figure 4.25. Deposition thickness on the walls of the ETF.

The pressure and shear stress distributions caused by the flow on the substrate are shown in Figure 4.26. The pressure distribution is caused by the particles striking the substrate and it shows a variation similar to the flux profile across the substrate. This is because the pressure distribution depends on both the number of particles striking the surface and the velocity normal to the surface which is the axial velocity in this case. The axial velocity profile (Fig. 4.23) shows that this component decreases with increasing radius, as expected. The shear stress across the substrate (Fig. 4.26) is obtained from the radial velocity and the flux. In this case, the flux decreases with increasing radius. The radial velocity, on the other hand, increases with increasing radius (Fig. 4.24). As a result, there is a peak in the shear stress away from the axis of symmetry. The pressure and shear stress values are almost identical for the cases with and without electronic energy. This may be explained by the fact that the flux is lower when electronic energy is considered while the velocities are higher. The net effect balances these opposite trends, thus creating nearly equal stresses on the substrate. The energy flux to the substrate is significantly higher when electronic energy is considered, despite the fact that the flux is lower. This is partly because the translational energy depends on the square of the velocity, which is higher in this case, and partly due to the additional mode of energy present. It is important to obtain the stresses and the heat flux to the substrate as they are often important data for the monitoring of manufacturing processes.

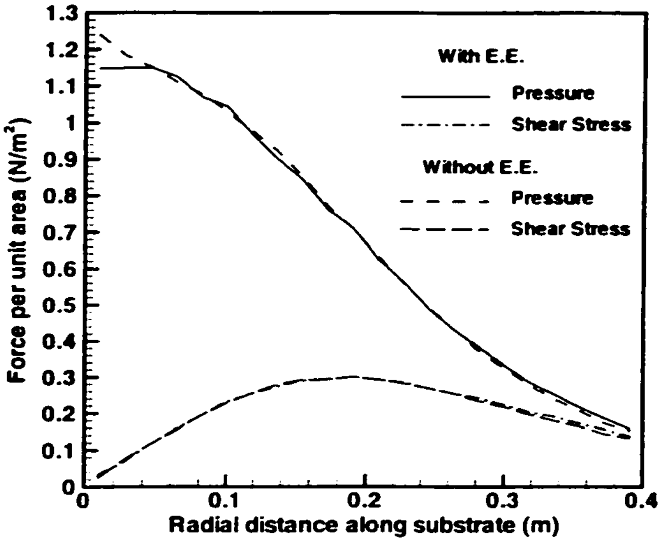

Figure 4.26. Pressure and shear stress exerted on the substrate

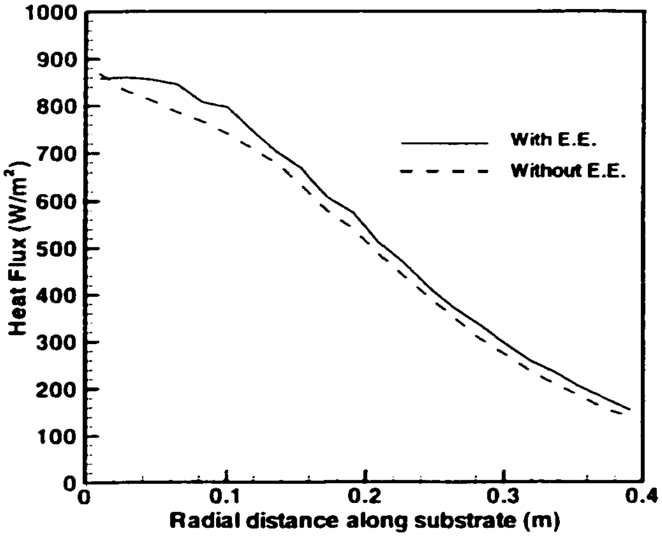

Figure 4.27. Energy flux to the substrate

4.5 Sensitivity Analysis

Sensitivity analyses are often performed on various systems for a wide range of purposes. A computational model of a system can become a powerful replacement for experimental and analytical techniques by changing various parameters in the computational model. This is usually cost-efficient and faster than the experimental counterpart. A sensitivity analysis performed on an ill-defined physical parameter can lead to effective phenomenological models of the parameter in question. This approach provides a solution that is hard to obtain using other methods. Another purpose of performing sensitivity analyses is to validate assumptions made in the computational model, as is done in this case.

Simulations of physical systems can depend on many physical parameters. Some of these parameters are difficult to determine, experimentally or otherwise. Assumptions often have to be made to accommodate these parameters in the simulation. The validity of the simulated result can be strengthened by performing a sensitivity analysis on these parameters. This is often done by comparing simulated results between cases where a single parameter is allowed to vary. This approach does not account for non-linear effects due to coupling of parameters, but it provides a good indicator of the sensitivity of the results to individual parameters.

In this section, three parameters are considered for the sensitivity studies. First, the effect of the collision cross section on the flow is studied. This provides an idea of how the deposition may be affected through the consideration of different values of the collision cross section for different excited states. Another assumption regarding the sticking coefficient is tested here by varying this parameter. In the absence of perfect sticking, particles may reflect off the walls of the chamber to affect the deposition of the substrate. Finally, the effect of the deformation of the molten pool is considered. The profile of the pool causes particles to evaporate in a direction that is locally normal to the surface, thus directing the particle velocities non-uniformly in the axial direction. The deposition on the substrate may thus be affected by the deformation in the evaporating surface.

4.5.1 Collision cross section

The modeling of the EB-PVD system under consideration involves several key assumptions involving a few parameters. One of these parameters is the collision cross section of titanium atoms. The atomic diameter of titanium has been assumed to be $4 \times 10^{-10}\ m$. It is assumed that this value is a reasonable one as it is close to that of argon, which has a molecular weight close to that of titanium. The cross section for collisions involving excited states is not known. The value of the collision cross section has been taken to be uniform for collisions between any two excited states. A sensitivity study was performed, comparing the base results with a case where the atomic diameter is $5.844 \times 10^{-10} m$, as predicted by Fan et al [60]. The results of this sensitivity analysis are presented in Figures 4.28–4.30.

The collision frequency for a system of particles may be expressed as an average of the product of the relative velocity of collision, g, and the collision cross section, σ:

$$\Theta = n < g\sigma > \tag{4.2}$$

where Θ is the collision frequency and n is the number density. The cross section in general can vary with the energy of the collision. When the VHS collision model is used, the variation in the cross section with the collision energy (i.e. the relative velocity of the collision) is given in Equation 2.7. The sensitivity study considers a

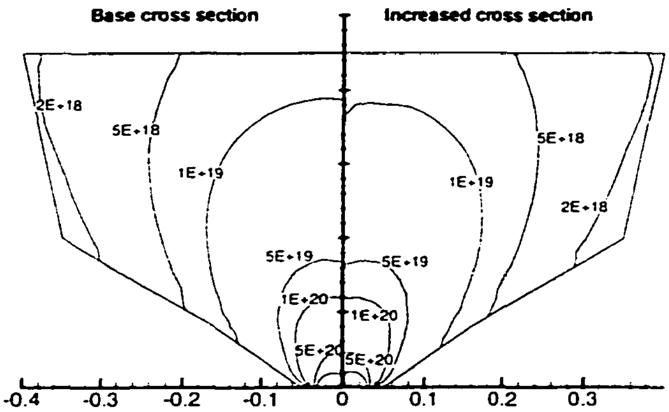

Figure 4.28. Number density contours ($\#/m^3$): Base case (left) and increased cross section (right)

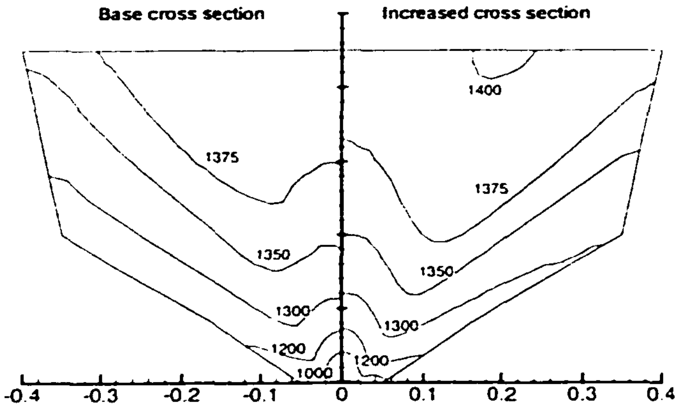

Figure 4.29. Absolute velocity contours (m/s): Base case (left) and increased cross section (right)

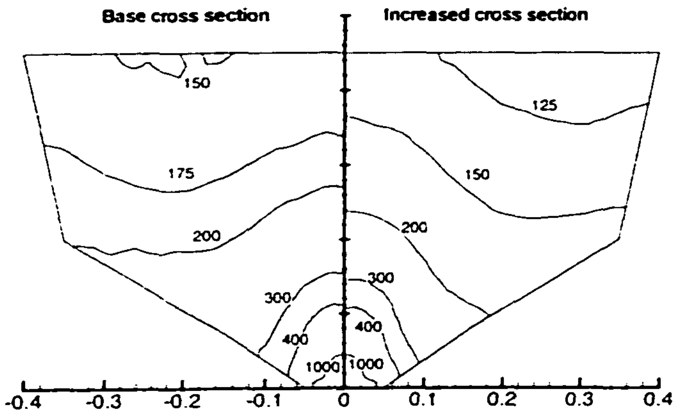

Figure 4.30. Translational temperature contours (K): Base case (left) and increased cross section (right)

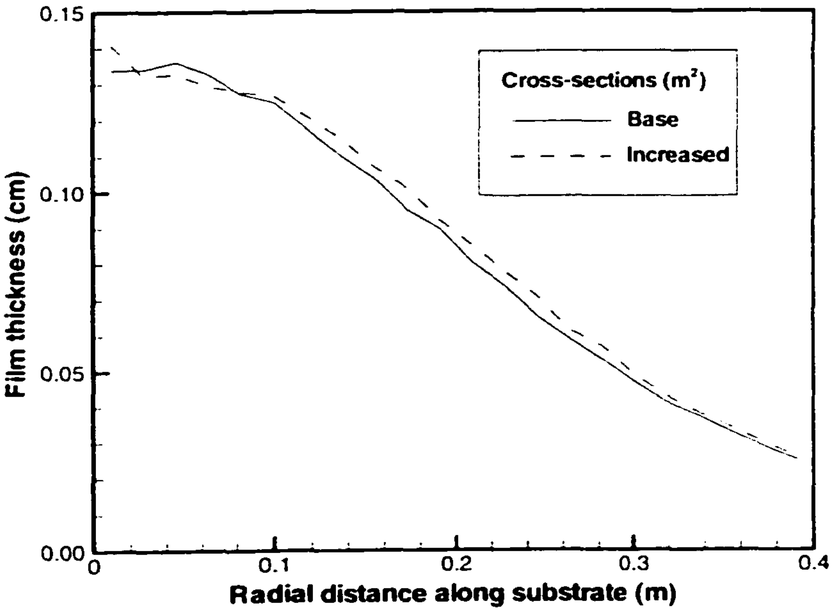

Figure 4.31. Deposition on the substrate: Comparison between the base case and increased cross section

VHS reference cross section that is 2.13 times larger than the base reference cross section.

The probability of a collision occurring in the DSMC algorithm is directly proportional to the collision cross section (Eq. 2.5). An increase in the collision cross section thus leads to an increase in the number of collisions in the flow. In this case, only the collision cross section is allowed to vary between the two cases. As a result of doubling the collision cross section in the test case, this simulation has roughly twice as many collisions as the base case. The higher number of collisions leads to greater redistribution of energy between the electronic and translational energy modes and also causes more thermal energy to be converted to kinetic energy. The collisional region is also larger in this case. This leads to a greater degree of expansion than the base case, as seen by the lower number density, higher velocity and lower temperature in the flow domain. The expansion is also increased in the radial direction with an increase in the collision cross section. This results in a significant change in the substrate flux profile, as seen in Figure 4.31. The deposition is lower than the base case near the axis and higher at larger radii. The difference is significant enough to suggest that the collision cross sections of the species under consideration play an important role in predicting the behavior of these flows. There is currently no data available on the cross sections for collisions involving different excited states. The availability and use of such data may considerably improve the accuracy of simulated results.

4.5.2 Sticking Coefficient

The sticking coefficient of vapor particles impinging on a surface may be expressed in terms of the fluxes (Γ) incident to and reflected from the surface:

$$s = 1 - \frac{\Gamma_{reflected}}{\Gamma_{incident}} \tag{4.3}$$

This parameter that is not known exactly is the sticking coefficient of titanium atoms on the walls of the vacuum chamber. This value is very close to 1. A small decrease in this value in the simulations would mean that some titanium atoms reflect diffusely off the walls, thus affecting the flowfield near the walls. The sensitivity analysis for this parameter involves the base case with a sticking coefficient of 1.0 and another with this value set to 0.95.

Figures 4.32 to 4.35 indicate that the flowfield properties are affected significantly when the sticking coefficient is changed from 1.0 to 0.95. The number density near the wall in the latter case is slightly higher than the corresponding value in the base case. This is because a small fraction of the atoms that strike the wall are reflected diffusely back into the flow domain. The increase in number density is most apparent immediately next to the wall, as this is the region where the reflected particles are mostly found. This reflection causes some particles to have velocities directed away from the wall, in a direction different from the bulk flow. Thus, the velocity distribution function is broadened in this region, leading to a reduction in the flow velocity and an increase in the translational temperature near the walls. These properties change significantly in the vicinity of the substrate. However, a comparison between the flux to the substrate in the two cases (Fig. 4.35) shows very little difference, which could easily fall within the range given by experimental measurements. Since only 5% of the flux incident on the

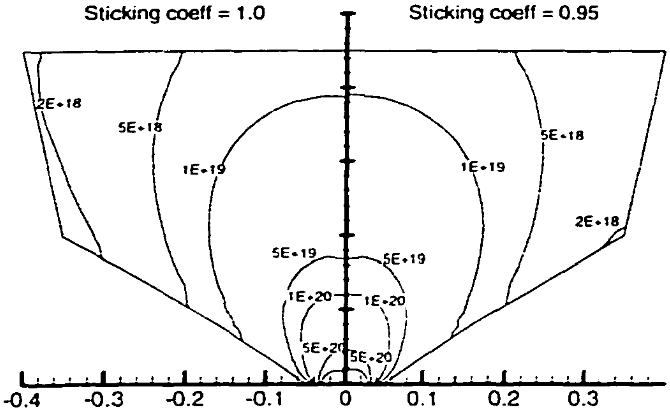

Figure 4.32. Number density contours ($\#/m^3$): Base case (left) and decreased sticking coefficient (right)

walls is reflected, the number of particles that are reflected onto the substrate is very low. Besides this, the wall temperature is low (300 K). The particles that reflect off the walls have low velocities as they are sampled from an equilibrium distribution with zero mean velocity at the wall temperature. Hence the flux of reflected particles to the substrate is too low to significantly affect the simulated deposition profile. Thus, the assumption of perfect sticking at the walls is justified in the simulation.

4.5.3 Shape of the molten pool surface

In EB-PVD processes, intense heating from an electron beam liquefies and vaporizes metal from an ingot. The momentum imparted by atoms vaporizing off the surface causes a deformation in the surface of the molten pool, as seen in Fig-

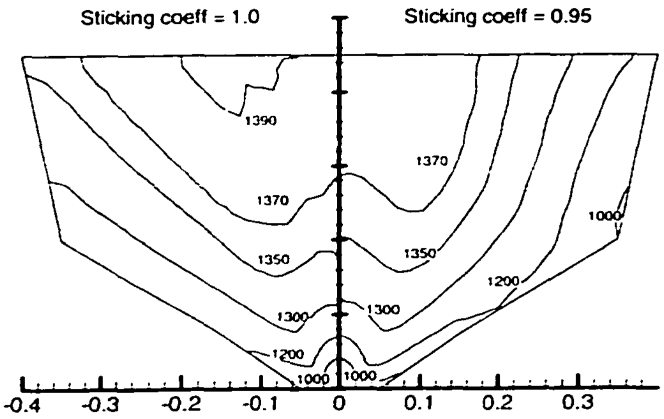

Figure 4.33. Absolute velocity contours (m/s): Base case (left) and decreased sticking coefficient (right)

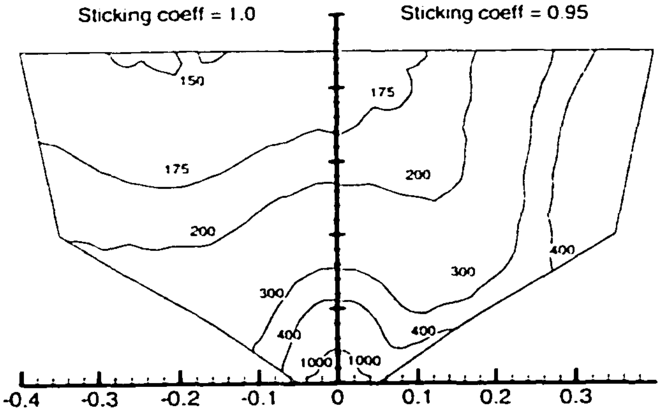

Figure 4.34. Translational temperature contours (K): Base case (left) and decreased sticking coefficient (right)

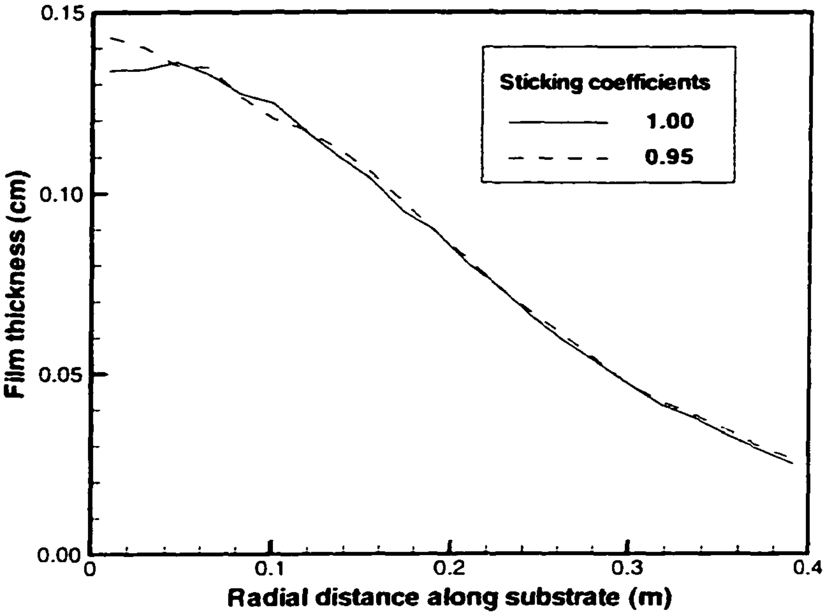

Figure 4.35. Deposition on the substrate: Comparison between the base case (sticking coefficient=1.0) and decreased sticking coefficient (0.95)

ure 4.2. In the simulations of such systems, this curvature may affect the flowfield properties as the evaporating particles have velocities that are normal to the evaporating surface. However, the deformation in such systems is usually very small. Approximating the surface of the pool to a flat profile may save computational effort and minimize the complexity of the problem, especially when such data is hard to obtain. Comparisons are thus made between cases where the melt pool surface is deformed and flat, in order to check the sensitivity of the results to the physical shape of the pool surface.

The flowfield contours show that the flow properties are not changed significantly when the deformation in the pool is approximated with a flat surface. The velocity contours show a slight variation, but this is on the order of a fraction of 1%. The substrate flux does not change significantly either. Only the deposition

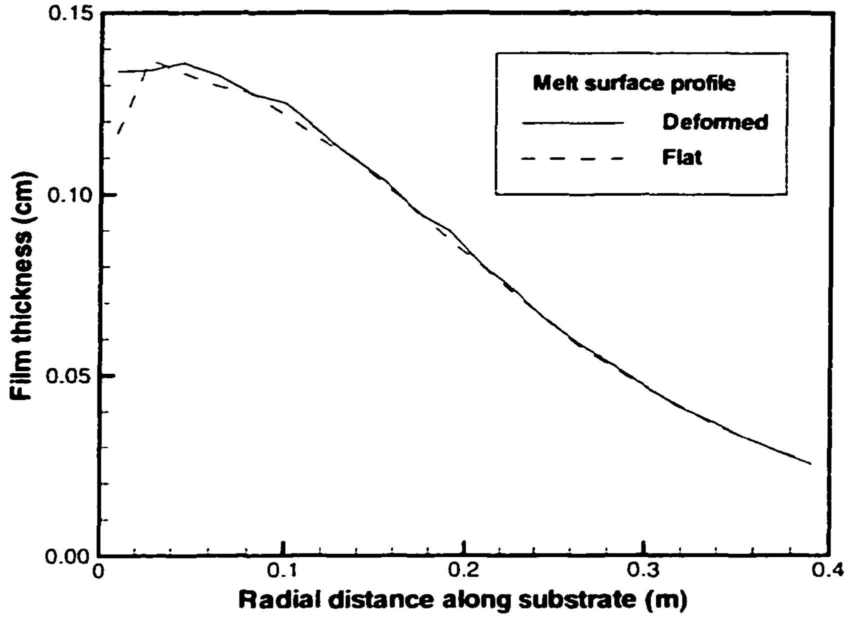

Figure 4.36. Deposition on the substrate: Comparison between the base case (deformed) and the flat melt pool shape

profiles are shown here in Figure 4.36. Since the deformation in the pool surface is very small, the velocities of the particles evaporating from a flat surface are directed in a direction that is not much different from a similar evaporation from a deformed surface. Also, the presence of the Knudsen layer and the collisional region above the evaporating surface ensure that the particles lose the small contribution to their velocities from the shape of the surface. As a result, the two cases provide nearly identical results. This indicates that applying the melt pool temperature and influx profiles to a flat surface yields accurate results without having to deal with the complexity of a deformed surface.

4.6 Conclusions

The physical vapor deposition of titanium on a substrate was modeled using the DSMC method. The effect of electronic energy on the simulations was studied. The high temperatures of the evaporating surface cause considerable excitation in the electronic states of the particles and the energy content in the electronic mode is significant when compared to the translational energy of the particles. The evaporating flow showed rapid expansion, with a rapid decrease in density, a rapid increase in velocity and a sharp decrease in temperature. The expansion occurred to a greater degree when electronic energy was included in the simulations, due to the extra energy content of the flow. The translational temperature was higher in this case due to the transfer of energy from the electronic to the translational mode. The velocities in the flowfield were also higher as more energy was available for conversion from thermal to kinetic energy. A comparison of the computed flowfield properties and experimental measurements showed excellent agreement when electronic energy was considered. This suggests that electronic energy is an important factor to include in the modeling of this process. These comparisons also suggest that the rate of transfer of energy from the electronic to the translational mode is lower than the actual flow, and better estimates of the collision cross section may be needed.

The flow considered was extremely rarefied and there was considerable non-equilibrium between the energy modes. Translational non-equilibrium was also seen and this originated in the Knudsen layer that was formed immediately above the evaporating source. The lack of enough collisions in the flowfield led to the non equilibrium behavior. The velocity and temperature showed a rapid change in the Knudsen layer and later showed very small changes, thus suggesting the freezing of these properties due to the lack of collisions.

An important factor to consider in modeling of flows of this nature is the backscatter to the molten pool, which reduces the net inflow rate in the simulation. The backscatter fractions were high — 17.40% when electronic energy was considered and 15.98% when only translational energy was considered in the simulations. The backscatter flux increased with the inclusion of electronic energy due to the greater number of collisions above the evaporating surface.

The deposition profiles obtained computationally showed good agreement with the experimentally measured values. The deposition was found to be lower with the inclusion of electronic energy in the simulation. This was caused by the higher translational temperatures in the domain leading to more radial expansion. A larger fraction of the flow was thus directed away from the substrate towards the walls of the domain.

A sensitivity study of the collision cross section showed that the deposition and the flowfield were significantly affected by changes in the cross section. Higher cross sections caused more collisions to occur in the flowfield, thus leading to greater expansion and more radial spreading. The deposition on the substrate did not change significantly when the sticking coefficient at the walls was changed from 1.0 to a value of 0.95. Though the flowfield properties were affected significantly, it was shown that the flux of particles reflected from the walls onto the substrate was negligible. The shape of the evaporating surface was shown to have nearly no effect on the flowfield properties and the deposition on the substrate. This was because the collisional area above the melt surface caused any directed velocity arising from the deformation of the surface to be equilibrated through collisions.

Chapter 5

Atomic Absorption Spectra

One of the challenges encountered in an experimental vapor deposition system is the measurement of the flow properties and the flux of the vapor plume. Atomic absorption spectroscopy is an important tool that is used extensively for this purpose. The absorption spectra generated through experimental measurements are an important means of comparing computational simulations of these systems with experiments. The means of making such comparisons are outlined below. The Monte Carlo simulations allow calculations of individual particle velocities and positions, which can be reduced to a distribution function. This in turn can be converted to an absorption scan for comparison with experimental measurements. In this chapter, the phenomenon of absorption is first introduced. Next, the method of obtaining computational absorption spectra is described. Finally, the computational results are compared to the experimental absorption spectra, and the effects of having baffle plates and an argon backpressure in the flow domain are examined.

5.1 The Absorption Phenomenon

Absorption spectroscopy is a tool that is used in many areas of research and industry [4],[93],[131]. This provides an accurate and non-intrusive method for identification of chemical structures, composition of substances, chemical reaction dynamics and quantitative analysis of atoms, vapor plumes and solutions. Many of the current applications of absorption spectroscopy have been made possible by the use of lasers. Laser light has special characteristics like coherence, directionality, high intensity, monochromaticity and wavelength tunability that make lasers a preferred source of radiation over conventional spectral lamps and black-body light sources.

Absorption spectroscopy is the study of attenuation of electromagnetic radiation by matter. The subject material is placed between the source of radiation and the spectrometer. Radiation of certain frequencies corresponds to the energy required for the transition of the subject atoms/molecules from one quantum state to another. Under these conditions, some amount of radiation is absorbed by the subject matter. The intensity of the radiation is reduced by the same amount through each path length of the beam. This is an exponential relationship known as Lambert's law:

$$I(x) = I_0 e^{-\alpha x} \tag{5.1}$$

where I_0 is the intensity of the incident light. I is the intensity of the beam after traversing a length x of the subject material and α is a constant known as the absorption coefficient. The attenuation of the beam intensity in the ETF is shown in Figure 5.1. The ordinate plotted represents the ratio of the intensity transmitted through the chamber to the original beam intensity, while the abscissa represents the Doppler frequency shift of the signal from an experimental reference frequency.

A particle that absorbs radiation undergoes a transition to a higher energy level of its energy modes. In the case of a molecule, this excitation can occur to a higher rotational, vibrational or electronic level, while in the case of atoms, it is restricted to electronic transitions alone. The frequencies at which electronic transitions occur in atoms usually correspond to the visible and ultra-violet ranges

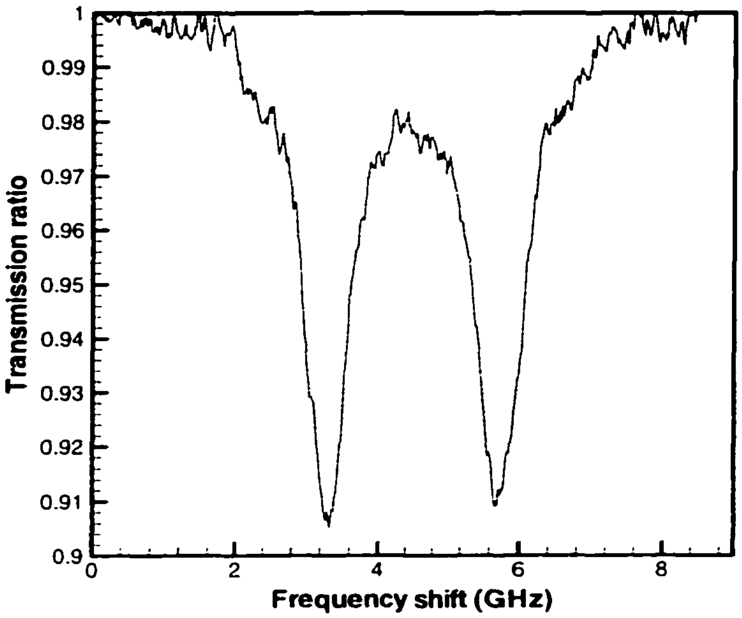

Figure 5.1. Transmission ratio of the laser in the ETF

of the spectrum. This process obeys the law of energy conservation:

$$h\nu = (E^{high} - E^{low})_{elec} + (E^{high} - E^{low})_{vib} + (E^{high} - E^{low})_{rot} \qquad (5.2)$$

These transitions occur in many different ways. However, the mechanisms of transition are beyond the scope of this study.

The absorption spectrum of a substance from a continuous source shows many peaks, corresponding to the frequencies absorbed by the substance. These peaks usually have a finite width due to broadening. At very low pressures ($< 10^{-2}$ Torr), Doppler effects contribute most to the broadening. This happens when a particle has a velocity in the direction of the beam. The frequency absorbed is slightly different from that absorbed by a stationary particle of the same species. When the particle velocities follow a Maxwellian distribution function, the broadening of the absorption peak is in the shape of a Gaussian. At higher pressures, collisions between particles can cause the broadening. Broadening can also occur due to the natural lifetime of excited states of the subject particles.

The Doppler line-shape function [115] is given by the Gaussian:

$$f(\nu) = \left(\frac{4ln2/\pi}{\gamma_D^2}\right)^{1/2} exp\left(-\frac{4ln2}{\gamma_D^2}(\nu - \nu_0)^2\right) \tag{5.3}$$

where ν_0 is the frequency absorbed by a stationary particle, ν is the frequency absorbed by the moving particle and γ_D is the full width at half maximum (FWHM) for the line-shape function. The FWHM, γ_D is given by:

$$\gamma_D = \frac{2}{\lambda}\sqrt{2\frac{k_B T}{m}ln2} \tag{5.4}$$

where λ is the wavelength of the radiation, T is the equilibrium temperature and m is the molecular weight of the particle. Using equation (5.4) in equation (5.3), we get an alternate form of the Doppler line shape function:

$$f(\nu) = \left(\frac{m\lambda^2}{2\pi k_B T}\right)^{1/2} exp\left(-\frac{m\lambda^2}{2k_B T}(\nu - \nu_0)^2\right) \tag{5.5}$$

In order to convert the results of a DSMC simulation into a form that is comparable to experimental absorption spectra, it is worth looking at the Maxwellian velocity distribution function:

$$f(v) = \left(\frac{m}{2\pi k_B T}\right)^{1/2} exp\left(-\frac{m}{2k_B T}(v - v_0)^2\right) \tag{5.6}$$

This is the distribution function in one dimension, which is the appropriate choice since the Doppler shift occurs only due to the velocity of a particle in the direction of the laser.

In equation (5.5), the term $(\nu - \nu_0)$ refers to the frequency shift due to the motion of a particle in the path of the laser. This motion is relative to a zero velocity in the direction of the laser. Hence the velocity v_0 in the Maxwellian distribution (Eq. 5.6) is zero. The Doppler shift of a frequency due to the motion of the source/observer is given by:

$$\nu - \nu_0 = v/\lambda \tag{5.7}$$

Hence the exponential terms in equations (5.5) and (5.6) are the same. This leads to the relation:

$$f(\nu) = \lambda f(v) \tag{5.8}$$

Equations (5.7) and (5.8) provide the means to convert a velocity distribution function into an absorption scan. Plotting $f(\nu)$ against $(\nu - \nu_0)$ yields the absorption scan. This can be converted to a plot of the absorptivity, which involves the scaling of $f(\nu)$ by a few constants. For the purposes of this work, the distribution function $f(\nu)$ is computed for comparison with experimental measurements.

5.2 Computation of absorption spectra

Absorption spectra can be calculated from the results of numerical simulations where the flowfield properties such as the velocities and temperatures are known along the coordinate directions. Simulations using the DSMC method involve the motion of individual particles. The properties of these particles can be used to compute an absorption scan directly from the simulation. However, this can be a complicated procedure. A simpler method can be used, which applies to any numerical method where the macroscopic flowfield properties are computed. This requires the assumption that the flow is in equilibrium in the vicinity of the laser's path. The idea of translational temperature and a Maxwellian velocity distribution apply only in these cases. However, non-equilibrium effects are often seen in flows.

When the DSMC method is used for these computations, the concepts of temperature and Maxwellian distributions functions are often applied, so as to provide some measure of understanding of the flow physics. Without these assumptions, there would be no way of quantifying the flow temperature. The same idea is used in the method described below.

The first step in the computation of the absorption spectra is to extract the flow properties along the path of the laser. If the direction of the laser does not correspond to one of the coordinate directions, then the velocity along the direction of the laser can be computed from the available data. The other flowfield properties needed are the translational temperature in this direction and the number density. This data can be extracted from contour plots by many data visualization software packages, using inbuilt functions.

The flow velocity and temperature are obtained in a DSMC simulation from the individual velocities of particles, with the computed temperature using the assumption of equilibrium. The individual particle velocities cause the Doppler broadening of the absorption spectrum, as described above. Hence it is necessary to obtain the distribution functions along the laser's path. This can be done by considering a Maxwellian distribution using the macroscopic velocity and translational temperature in the direction of the laser (Eq. 5.6). This must be done for velocities in the range of at least two standard deviations on either side of the macroscopic flow velocity. The distribution function provides only a fractional distribution of particles at a certain temperature and macroscopic velocity. This must be multiplied by the number density at the corresponding location in order to compute the absorption at a certain energy (or individual particle velocity). A summation of this quantity $nf(v)$ along the path of the laser provides the total absorption. This spectrum can then be normalized for comparison with experimental data.

5.3 Results

The Experimental Test Facility (ETF) at Lawrence Livermore National Laboratories has been used to study physical vapor deposition of titanium. The ETF is equipped with 2 laser ports, one of which is used to determine the flow velocity and temperature. The location of the ports is shown in Figure (5.2), where the domain has been rotated through 90° for computational purposes. The domain has baffle plates in place, with the upper plate having slits for the vapor to pass through. The substrate is placed at the location of the upper plate. The results here are obtained from the laser path at the location $x = 0.4826m$ in the flow domain depicted in Figure (5.2).

The flow contours are shown in figures (5.3)-(5.6). These figures show a comparison of the properties in a domain without the baffle plates and in a domain with the baffle plates in place. The flow expands through the lower part of the domain in a nearly identical manner in the two cases. As discussed in Chapter 4, the density drops through three orders of magnitude in the first $0.4m$ of expansion. The mean free path at this stage increases from around $0.001m$ to $1m$. The collision rate in the flow drops due to expansion and there are very few collisions in the vicinity of the slits. The absence of collisions prevents the flow from expanding around the sharp corners provided by the plates in the latter case. Since the walls are assumed to be perfectly sticking, the particles cannot reflect off the walls into the region behind the slits. Hence these regions have very few particles in them.

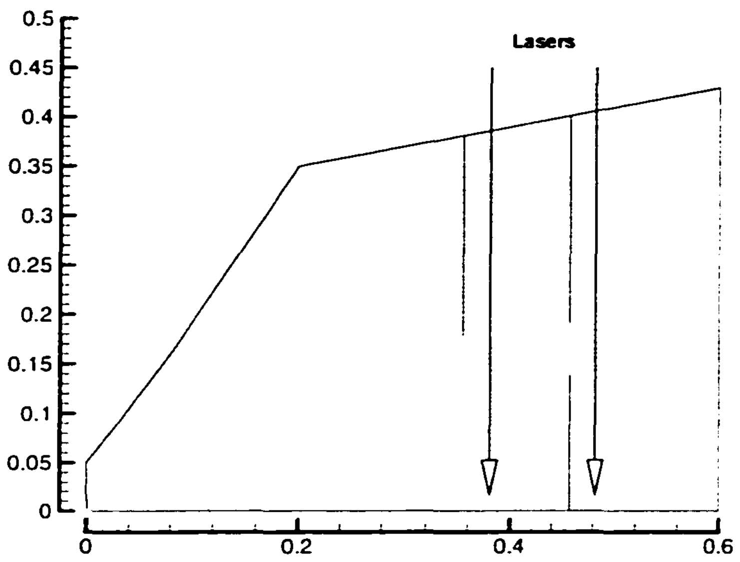

Figure 5.2. Boundaries of the flow domain. All dimensions in *m*

The number densities in these regions is more than 6 orders of magnitude lower than the source number density. When the flow passes through the slit in the upper plate, it is collimated into a nearly collisionless beam. The lack of collisions prevents particles from having a transverse velocity with respect to the beam, thus limiting the spreading of the beam. This is seen in the form of extremely large gradients in the number density at the edge of this beam beyond the upper slit. The velocity in the flow domain increases due to expansion from the few collisions that take place, while the translational and electronic temperatures drop. There is a large gradient in these properties at the edge of the beam due to the lack of collisions.

The upper laser is used to determine the properties of the vapor in the region above the upper slit. The bulk of the absorption is caused by the collimated beam as there is an extremely low density in the other parts of the domain that the

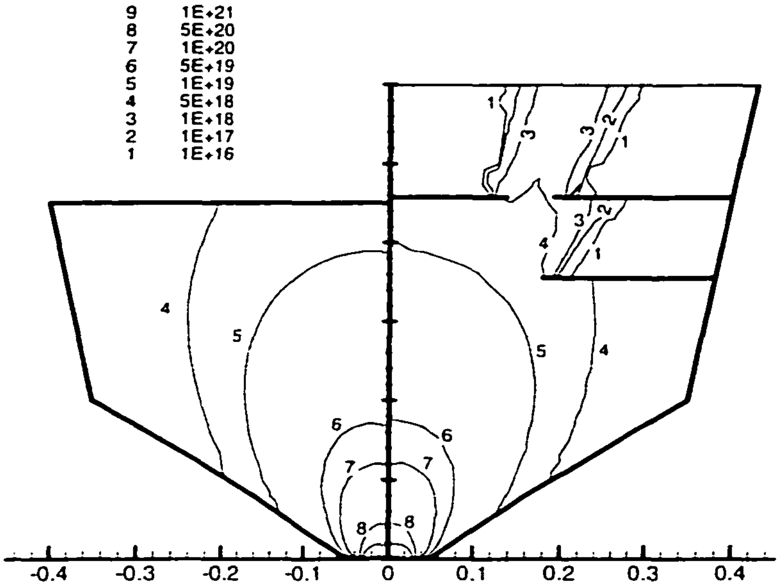

Figure 5.3. Number density contours ($\#/m^3$) in the domain with and without slits (right and left respectively)

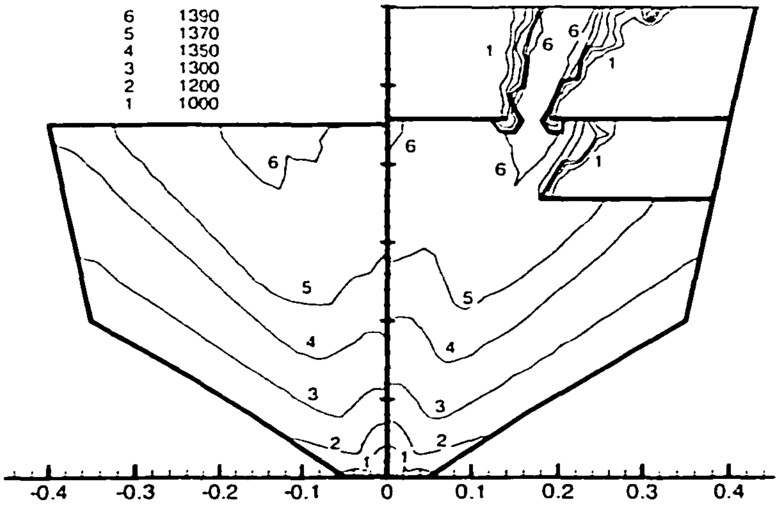

Figure 5.4. Absolute velocity contours (m/s) in the domain with and without slits (right and left respectively)

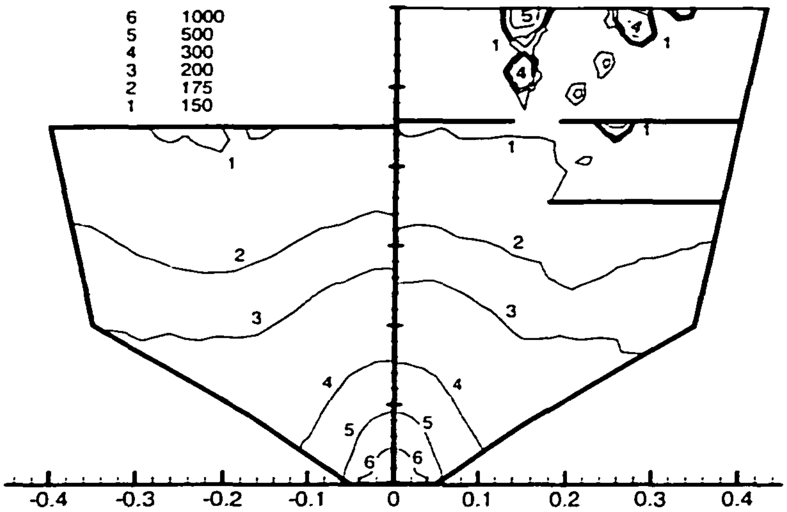

Figure 5.5. Translational temperature contours (K) in the domain with and without slits (right and left respectively)

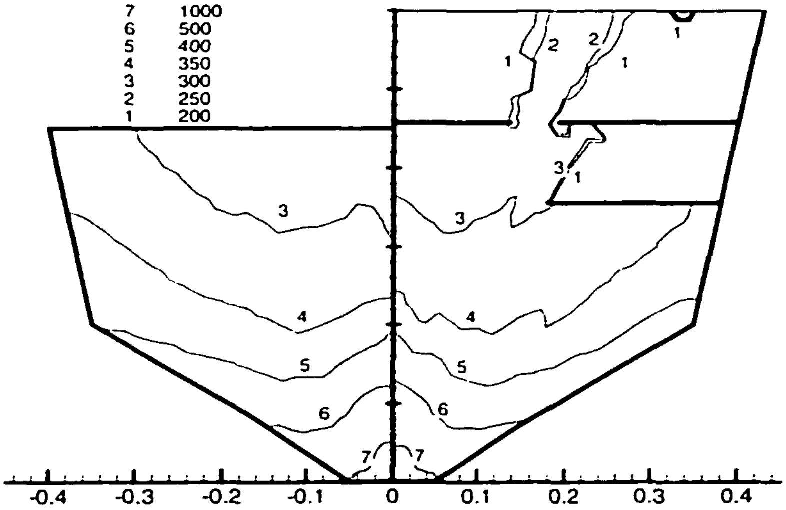

Figure 5.6. Electronic temperature contours (K) in the domain with and without slits (right and left respectively)

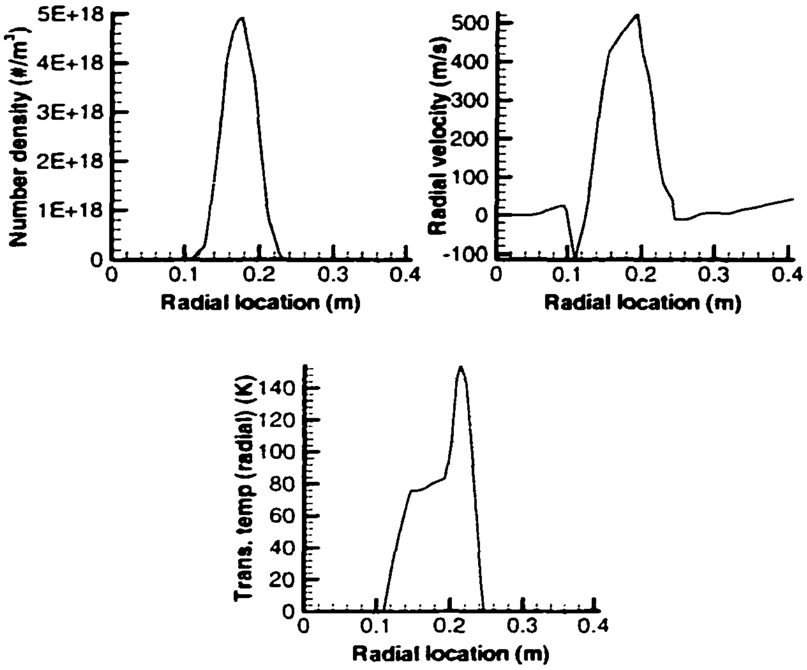

Figure 5.7. Flow properties along the laser's path, in the plane of the laser

laser passes through. The absorption spectrum obtained from the experiments was reduced to an analytical expression by fitting it with a Gaussian distribution. These distributions are available implicitly through the macroscopic flow velocity and translational temperature that define them. The experimental data presented in Figure (5.8) is the Gaussian profile associated with these fits of the absorption spectra, obtained from the flow velocity and temperature.

The profiles in Figure (5.8) plot the velocity distribution of particles in the path of the laser against the shift in the frequency of the laser caused by their motion. The x-axis can be superimposed on a larger range with the abscissa $x = 0$ coinciding with the laser frequency. Then the x-axis would represent the true frequency. For the purposes of this study, the frequency shift is used. This has no bearing on the results presented. The profiles show double Gaussian peaks as the particles escape through a slit placed a little distance away from the axis. This

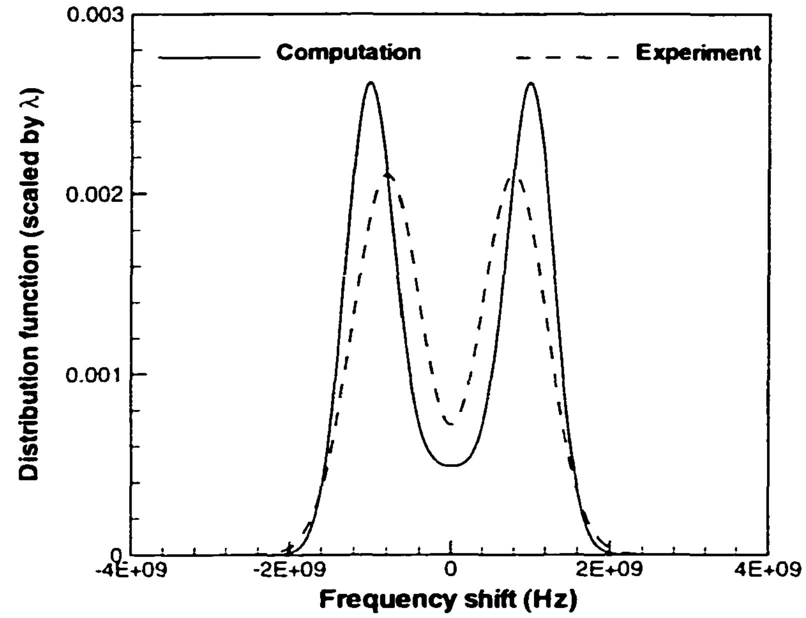

Figure 5.8. Absorption spectra in the ETF without a backpressure.

causes them to have a net radial velocity, causing the distributions to be centered around a non-zero frequency shift. The two peaks correspond to the openings on either side of the axis in the plane of the laser, where the radial flow velocities are equal and opposite in direction.

The experimental profile has a radial flow velocity of 356 m/s and a temperature of 207 K. In comparison, the computed profile shows a radial velocity of 460 m/s and a temperature of 74 K. This discrepancy is to be expected because of the details involved in the modeling of the ETF. In the experiment, an argon gas bleed was used in the vicinity of the laser. This caused the presence of a low velocity argon cloud, which was at room temperature. Collisions between the argon cloud and the titanium vapor scatter the particles in the radial direction, thus increasing the spread of the Maxwellian distribution. This could increase the temperature measured through the scan. In order to evaluate the effect of argon

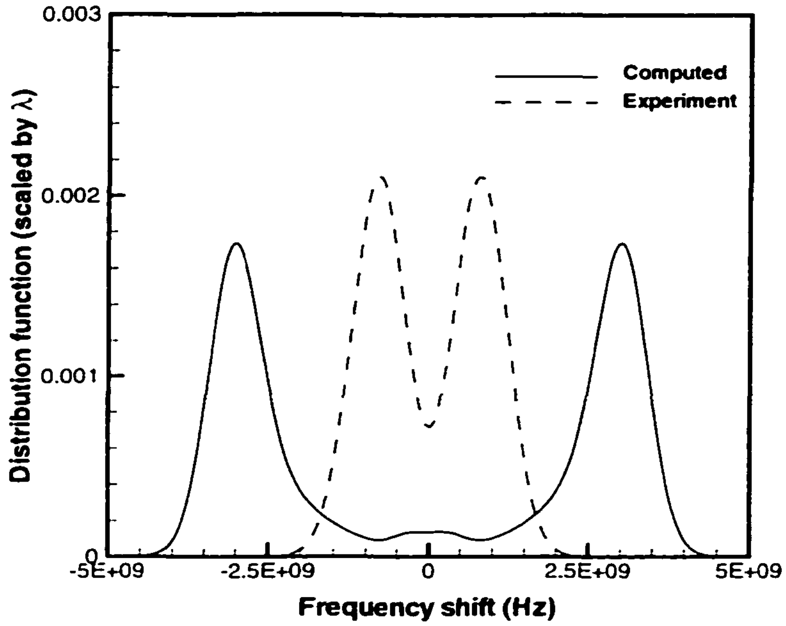

Figure 5.9. Absorption spectra in the ETF when an argon background is present.

in the system, a simulation is carried out with argon as a background gas, with a background density of $2 \times 10^{18}\#/m^3$. The resulting absorption scan from this simulation is shown in Figure 5.9. As seen in this figure, the absorption spectrum of the titanium vapor is very different from that shown in Figure 5.8. The radial velocity in this case, when argon is present, is $1207 m/s$, which is much larger than the experimental value, and the computed value in Figure 5.8. The increased radial spreading above the slit is seen in the number density and absolute velocity contours in Figures 5.10 and 5.11 respectively. The velocities in this region are higher when an argon back pressure is present, thus increasing the radial velocity computed in the absorption scan. The increased radial spreading above the slit is also seen in the higher translational temperature values (Figure 5.12) when argon is present in this region.

Although a discrepancy is seen between the measured and computed velocities

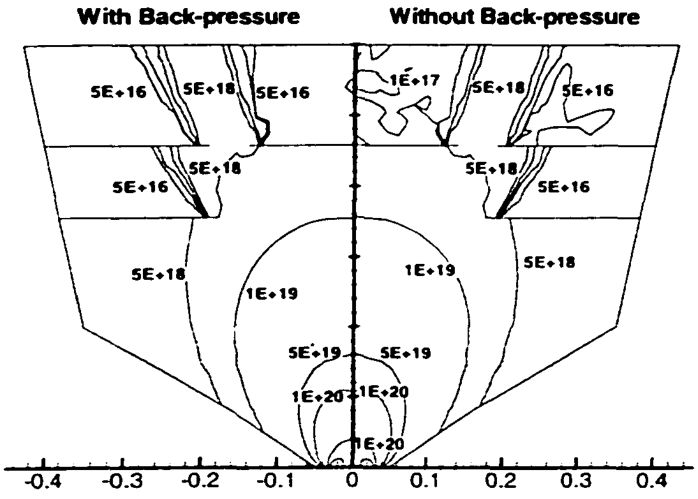

Figure 5.10. Number density contours in the ETF when an argon background is present.

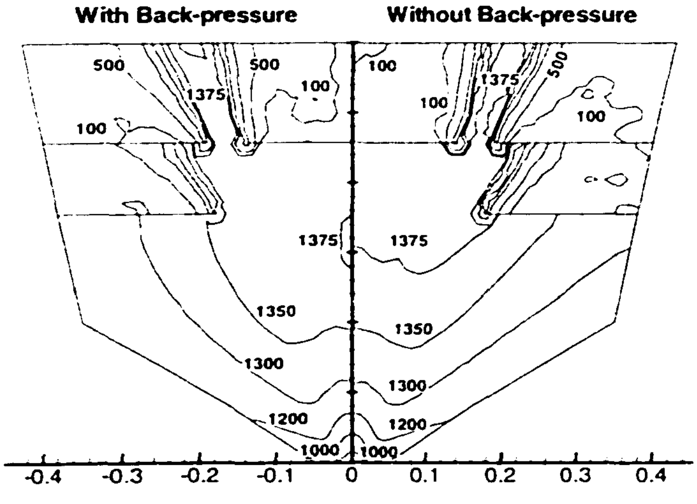

Figure 5.11. Absolute velocity contours in the ETF when an argon background is present.

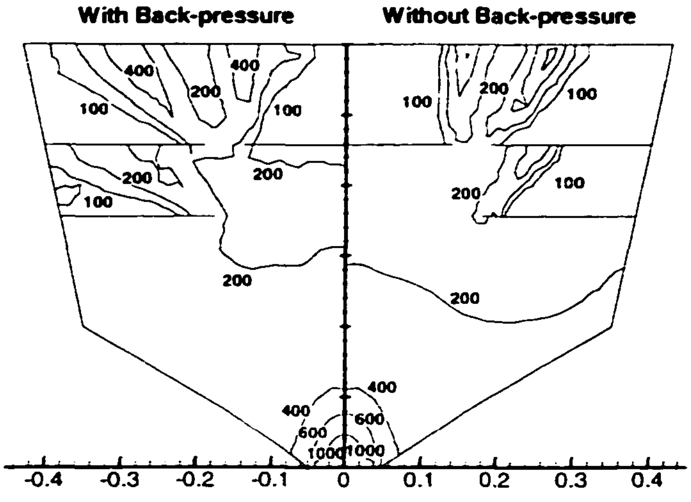

Figure 5.12. Translational temperature contours in the ETF when an argon background is present.

from the absorption scans, the temperature of the titanium vapor is calculated to be $232K$ when argon is present (Figure 5.9), which agrees very well with the experimental measurement. The discrepancy in the velocity arises from the uncertainty in the modeling of the argon background vapor. In the current set up, the argon background above the slit has no mean velocity. However, the experiment has the argon bleed from an orifice which is positioned on one side of the chamber. The background argon thus has a mean velocity in the radial direction, which could cause the titanium vapor to be scattered with a lower radial velocity. The modeling of this set up is difficult, but it can be seen that some of the discrepancy in the temperature can be explained by the presence of the background argon gas. The flow properties computed by the simulation are also sensitive to the collision cross section used. A higher value of the collision cross section would result in more collisions in the beam above the slit, thus creating a higher temperature profile.

5.4 Conclusions

The absorption profiles were computed for the configuration used in the experiment. The baffle plates used in the flow domain served to collimate the beam due to the lack of collisions in the flowfield. Large gradients were seen at the edges of the collimated beam because of this reason. The low collisionality of the beam passing through the upper slit causes a low temperature to be computed. The computed value of the flow velocity was higher than the experimental value, while the computed temperature was lower than the experimentally measured value. This discrepancy could be explained in part by the experimental set-up. The experiments included an argon gas bleed which could scatter the collimated vapor above the slit, thus causing a higher temperature to be measured. Absorption spectra computed with this condition in place could improve the agreement between the experimental and computational spectra.

Chapter 6

The Line Of Sight Method

Although the DSMC method is an extremely powerful tool used to solve engineering problems, it requires a lot of computing power and takes a long time to yield solutions to a flow problem. Many engineering processes require fast turn-around times for solutions, and may also require a number of simulations covering a range of values of a particular flow parameter. In such cases, it is advantageous to use a simpler method that can provide quick and inexpensive solutions to the problem at hand. The Line Of Sight (LOS) method has been developed with this objective, and is meant to serve as an alternative to the DSMC method for flows in the near-collisionless and free molecular regimes. This chapter introduces the LOS method, describes the LOS algorithm and explains a few procedures used in the algorithm in detail.

6.1 The need for the LOS method

Among its applications, the DSMC method is often used in simulations of flows that involve very few collisions in the flow domain. These flows are often characterized by Knudsen numbers close to 1. The flows may be entirely collisionless or may have the collisions being restricted to a few regions (e.g. rapidly expanding rarefied flows). The collisional phenomena may be largely irrelevant in the simulations of these flows. It must be noted that some of these flows may be near free-molecular in nature but the collisional phenomena may still be very important (e.g. charge exchange collisions in Hall thrusters [125]). Despite being well suited to handle collisionless and near-free-molecular flows, the DSMC method has the drawback of a huge computational requirement, both in terms of processor time and real time. The DSMC algorithm involves many steps that may become redundant in the case of a collisionless flow. The basic steps of the DSMC algorithm are:

1. Assign collision pairs among the particles in each cell of the domain

2. Calculate of the collision probability and loop through a conditional accept-reject routine for each selected collision pair

3. Move the particles through an incremental distance corresponding to the particle velocity and the time-step of the simulation.

While the collision dynamics involves a lot of computational effort, there is the additional burden of moving particles through very small distances. This is because the time-step has to be small enough to capture the physics accurately, which often results in particles residing in a single cell over multiple time-steps.

The simulation of a collisionless flow can thus be made faster by eliminating the first two steps listed above and by moving the particles through the domain without the constraint of the time-step. This is the basic structure of the Line-Of-Sight method, which addresses the need for accurate simulations of collisionless flows at a fraction of the computational cost of the DSMC method.

6.2 The scope of the LOS method

The LOS method is a tool that can be used in many ways. It is possible to have a stand-alone LOS simulation for a flow domain. Alternatively, a LOS simulation can take its input from a DSMC simulation, which would in effect divide the flow domain into collisional and collisionless regions with each being handled by a different algorithm. The way in which the LOS simulation is performed would depend on the nature of the flow. If the flow is collisionless, then a stand-alone LOS simulation would yield an accurate result. If however, the flow has regions that are collisional and collisionless, it is necessary to use the LOS simulation only in those regions where the collisional phenomena are unimportant. The latter case would involve running DSMC simulations on small parts of the flow domain and LOS simulations on the remainder of the domain. Each could conceivably take input from the results in other parts of the flow domain. For example, a rapidly expanding flow could have a DSMC simulation performed on its collisional regions, where the physics could be accurately captured. The resulting particle velocities and positions at the interface boundary of this simulation could be used as input to the LOS simulation of the other (collisionless) part of the flow domain. This could be advantageous in two ways. First, the overall simulation would be faster than an equivalent DSMC simulation. Also, the smaller DSMC simulation performed could be done with greater accuracy due to the reduced scale, and possibly due to more uniform length scales of the flow through the small domain.

6.3 Variations of the LOS method

The LOS method involves the movement of particles through a flow domain based on their velocities and initial positions. Since the motion of each particle is completely de-coupled from that of any other particle, the time-step is an irrelevant quantity in these simulations. Thus, the motion of particles can be handled sequentially by the processor, from the point of origin to the point of termination of the particles' paths in the flow domain. This simply uses the fact that the chronology of particle motion can be ignored. The computation of the path of each particle can be done based on its velocity and initial position, but this can be done in different ways for different purposes. The advantage with a grid-based simulation is the availability of information at every cell in the flow domain, which leads to a clear understanding of the flow-field in the domain. This is also a necessary for comparison with experimental absorption scans that are measured in the flowfield. On the other hand, a simulation which calculates only the end-point of the particle path on the domain boundary provides information on flux to the walls. This simulation can be performed at very high speeds and has low computational requirements. The LOS method can easily be adapted to fit either of these situations.

In a boundary based simulation, the savings in cost include the savings in generating a computational grid. Knowing the particle position and velocity will lead to a unique termination point on the boundary. The boundary will need to be divided into intervals to sample the particles at each location along the boundary. Also, in a steady flow, the flux of particles entering a flow domain is constant and equals the flux of particles incident on the boundary (as collisions do not change the path of the particles). Hence the flux along the boundaries can be determined easily and the computation is greatly simplified. A grid based simulation provides more detail on the flow-field. The path of each particle passes through a number of cells in the grid. If these cells are not of uniform size, then the residence time of a particle in each cell in its path is different. Since the data such as the number density in a cell are weighted according to the residence time of a particle in the cell, it is necessary to factor this in the calculations. Hence for each particle trajectory, it is necessary to determine the cells the particle passes through, the residence time in each of these cells and sample the data based on the particle properties and residence times. This calculation is more intensive than the boundary based simulation but it has the advantage of providing detailed information. The computation is faster than an equivalent DSMC simulation since it ignores collisions and does not rely on a time-step for the progress of the simulation.

The version of the LOS method that is described in this chapter is grid based. This method yields flowfield contours which are presented in Chapter 7.

6.4 The LOS algorithm

The LOS algorithm shares many aspects of the DSMC method. Both methods deal with the movement of particles through a computational grid, with macroscopic properties obtained through the sampling of particle properties. However, the two methods have a fundamental difference that leads to different structures in their algorithms. As explained in Chapter 2, the DSMC algorithm decouples particle movement from particle-particle collisions. The interaction between particles in the system ensures that every particle has to be treated as a part of a collective whole. The properties of a particle change at the same instant as those of every other particle in the system. Thus, the basic unit of forward propagation of the algorithm is the time step of the simulation. As the simulated time is incremented by the time step, the system evolves through its constituent particles.

On the other hand, the LOS algorithm is completely collisionless in nature. The lack of interaction between particles ensures that a particle's properties in a system are completely unaffected by anything else in the system (assuming the lack of body forces on the particles). This eliminates the need for a particle to be analyzed at the same instant as other particles in the system. Particles are thus regarded in the context of a collective whole only for the calculation of the macroscopic properties of the flowfield. The lack of time dependence in the system implies that particles may be analyzed one at a time, by evaluating their complete transit through the flow domain. Thus, the basic unit through which the LOS algorithm marches forward is the particle itself.

A schematic of the LOS algorithm is given in Figure 6.1. The first step in the algorithm is the initialization of the simulation. During initialization, the grid representing the flow domain is read and the grid dependencies between neighboring cells and boundary edges are determined. In addition, the physical parameters controlling the simulation are read from datafiles and various physical routines are initialized. Since the inflow fluxes are known, and the total number of particles considered in the simulation are known, it is possible to calculate how much time would be required in the real system for the specified number of particles to be introduced through the inflow surfaces. This parameter is important in particle generation as well as in sampling, and hence this time is calculated in the next step of the simulation. The algorithm then proceeds to handle the particles one by one.

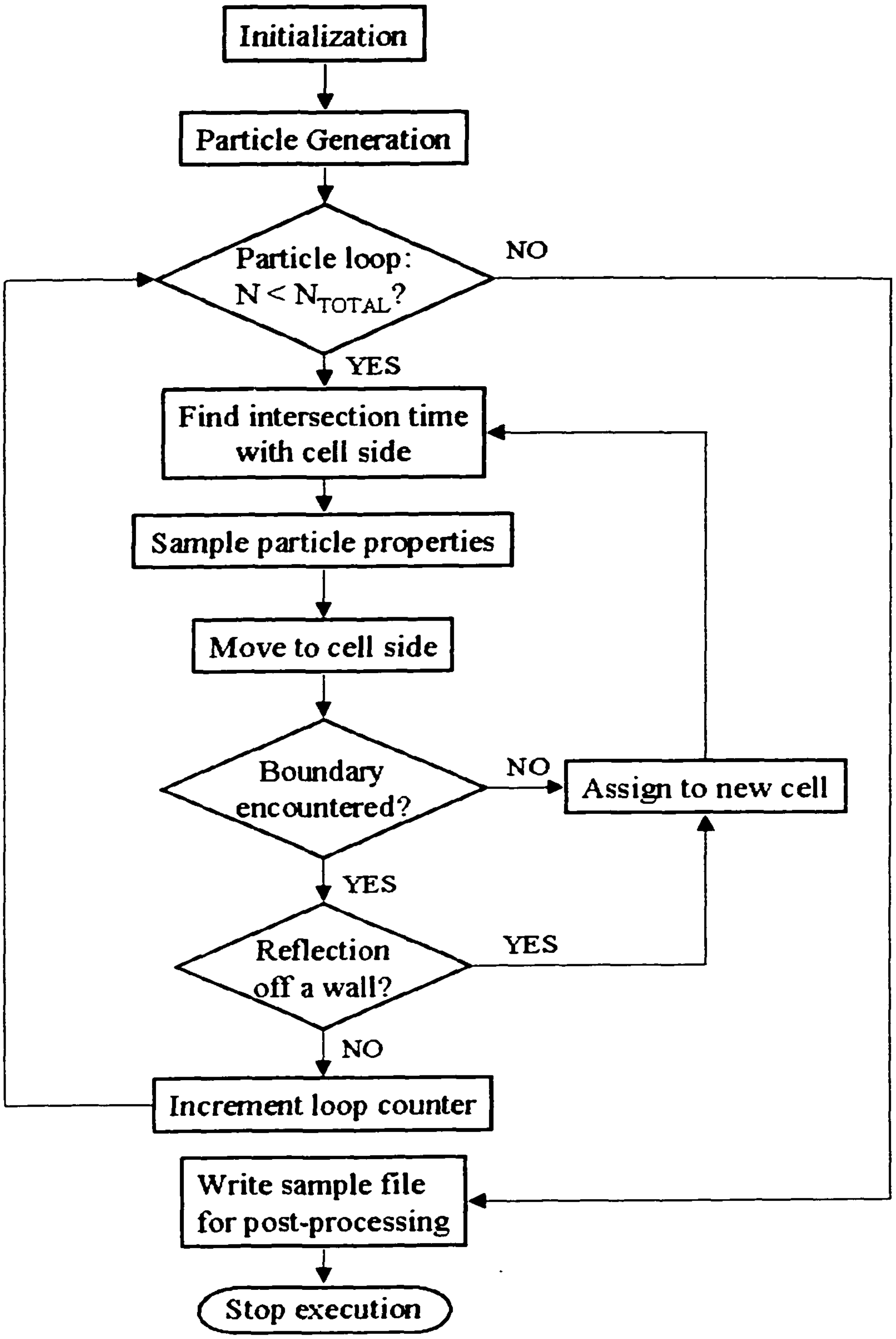

Figure 6.1. The Line Of Sight algorithm

As mentioned earlier, the particle loop controls the forward progress of the simulation. First, each particle is generated at the inflow boundary. The particle properties are determined in a manner similar to the DSMC algorithm. The particle position is determined at a random location along an inflow edge and its velocities along the coordinate directions are sampled from equilibrium distributions specified by the inflow conditions. The internal energies are also sampled from the appropriate equilibrium distributions. Once the particle has been generated, it is moved through the computational domain, one cell at a time. To do this, the intersection of the particle's trajectory is calculated with the sides of the cell it is present in. The time for the intersection is calculated along with the location along the cell side. The particle properties are then sampled for the cell, as explained later in Section 6.6. The particle properties are then updated to move it from its old location to the new one. At this point, the particle can either pass into another cell, or encounter a boundary edge. In the case of a reflection off a wall, the particle stays in the flow domain. All other boundary conditions result in the particle exiting the simulation. After a wall reflection or transit into another cell, the movement procedure is repeated until the particle exits the flow domain. The particle loop counter may then be incremented to handle the next particle.

Once the particle loop has been completed, the sampled information from all the cells is converted into macroscopic flow properties. Since the sampled data is collected in each cell of the flow domain, it is possible to generate flowfield contours for the simulation. In addition, all boundary interactions of the particles are sampled and these data can be converted into boundary fluxes, stresses and heat transfers.

6.5 Particle movement

The LOS method requires a fast and efficient means of computing a particle's trajectory through a flow domain. The motion itself can be reduced in a computational algorithm to a change in the particle's location after a time interval, rather than explicitly tracing the exact motion through the domain at all instants of time. The methods described below can be applied to both grid based and boundary based simulations, as a cell and the domain boundary are both simply closed areas surrounding the particle. The representation of axisymmetric flows using a two-dimensional computational domain makes the motion more complex than the relatively straightforward two-dimensional flow case. Hence, these cases are described separately in the subsections that follow.

6.5.1 Two-dimensional flows

When a particle is enclosed in a closed domain, its motion must lead it to intersect one, and only one of the boundary edges of the domain. It is then helpful to consider the intersection of the particle's trajectory with a line segment, as shown in Figure 6.2. Consider a line segment between points (x_0, y_0) and (x_1, y_1), and a particle at a location (x_p, y_p) with a velocity $\vec{V} = u\hat{\imath} + v\hat{\jmath}$. Its motion leads to an intersection with the line segment at a location (x'_p, y'_p). This intersection can be considered to lie at a fractional distance λ from (x_0, y_0), where $\lambda = 0$ at (x_0, y_0) and $\lambda = 1$ at (x_1, y_1). The intersection lies on the line segment if and only if:

$$0 \leq \lambda \leq 1 \tag{6.1}$$

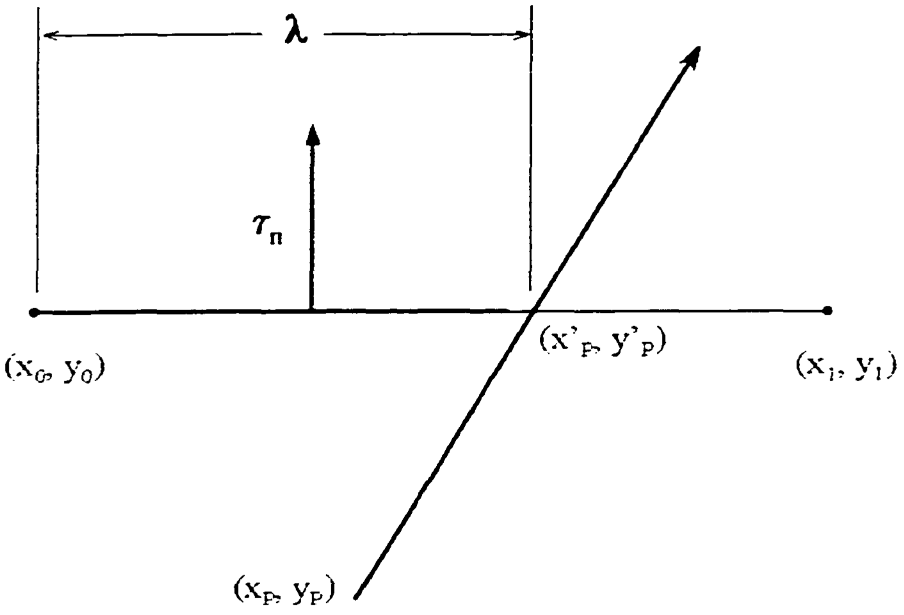

Figure 6.2. Intersection between a particle's trajectory and a line segment

From the principles of interpolation,

$$\frac{x_p - x_0}{x_1 - x_0} = \lambda = \frac{y_p - y_0}{y_1 - y_0} \tag{6.2}$$

Now, considering the time taken for the particle to move from (x_p, y_p) to (x'_p, y'_p) to be t,

$$x'_p = x_p + ut \tag{6.3}$$

$$y'_p = y_p + vt \tag{6.4}$$

Using Equations 6.3 and 6.4 in Equation 6.2, we get:

$$t = \frac{(x_0 - x_p) + \lambda(x_1 - x0)}{u} \tag{6.5}$$

$$t = \frac{(y_0 - y_p) + \lambda(y_1 - y0)}{v} \tag{6.6}$$

Equating these two expressions for t and solving for λ, we get:

$$\lambda = \frac{v(x_0 - x_p) - u(y_0 - y_p)}{u(y_1 - y_0) - v(x_1 - x_0)} \tag{6.7}$$

Applying the inequality in Equation 6.1 to Equation 6.7, we get

$$u(y_1 - y_0) - v(x_1 - x_0) < v(x_0 - x_p) - u(y_0 - y_p) < 0 \tag{6.8}$$

OR

$$u(y_1 - y_0) - v(x_1 - x_0) > v(x_0 - x_p) - u(y_0 - y_p) > 0 \tag{6.9}$$

Another condition needs to be applied to choose between these two options. An analysis of Figure 6.2 shows that the velocity vector must include an acute angle with the outward normal vector $\vec{r_n}$ to the cell side. Mathematically, this is expressed as:

$$\vec{r_n}.\vec{V} \geq 0 \tag{6.10}$$

where the outward normal is expressed as:

$$\vec{r_n} = \frac{(y_1 - y_0)\hat{\imath} - (x_1 - x_0)\hat{\jmath}}{\sqrt{(x_1 - x_0)^2 + (y_1 - y_0)^2}} \tag{6.11}$$

Equation 6.10 thus reduces to:

$$u(y_1 - y_0) - v(x_1 - x_0) > 0 \tag{6.12}$$

which validates the condition given by Equation 6.9.

This condition can be used with any cell or boundary side. Only one of the edges will satisfy this condition for a closed, convex domain. The intersection point on the edge can then be determined using Equation 6.2 and the time taken to intersect the side can be obtained through Equation 6.5

6.5.2 Axisymmetric flows

In an axisymmetric flow, the macroscopic properties do not vary in the azimuthal direction. A two-dimensional grid with an axis of symmetry is thus used to represent any azimuthal plane in the flow. A particle's movement in the azimuthal direction causes it to leave the plane represented by the grid. The computational grid is thus rotated to contain the azimuthal plane containing the particle's location after its motion. During the motion, the particle's distance from the axis changes as a result of its velocity components perpendicular to the axis. Considering the initial radial position to be y_p, the velocity components in the Y and Z directions to be v and w respectively, and the radial position after the rotation of the axis to be y'_p, we have:

$$y'_p = \sqrt{(y_p + vt)^2 + (wt)^2} \tag{6.13}$$

The direction of the particle's motion is then changed relative to the new azimuthal plane under consideration, which indicates that the velocity components

v and w change. The new velocity components v' and w' are given by:

$$v' = \frac{v(y_p + vt) + w^2 t}{\sqrt{(y_p + vt)^2 + (wt)^2}} \tag{6.14}$$

and

$$w' = \frac{w y_p}{\sqrt{(y_p + vt)^2 + (wt)^2}} \tag{6.15}$$

The axial coordinate and velocity are unaffected by the rotation. The new axial position is given by Equation 6.3. Repeating the analysis used in Section 6.5.1 for this case, Equation 6.2 expands to:

$$\frac{x_p + ut - x_0}{x_1 - x_0} = \lambda \tag{6.16}$$

$$\frac{[(y_p + vt)^2 + (wt)^2]^{1/2} - y_0}{y_1 - y_0} = \lambda \tag{6.17}$$

Using Equation 6.5 in Equation 6.16, we obtain a lengthy quadratic expression in λ, which is not represented here. The solution to this quadratic is discussed in detail by Dietrich and Boyd [51]. This procedure uses an efficient method for checking the intersection conditions with the cell sides, and for the calculation of the location and time of intersection.

6.6 The sampling procedure

The sampling of particle properties is necessary in the LOS algorithm in order to obtain the macroscopic flowfield properties from individual particle properties. The important macroscopic properties to resolve are the number density, the velocities along the coordinate directions and the temperature.

During sampling, each cell has an array of the sums of the particle properties. Particles contribute to these sums as they transit through the cell. The time taken for a particle to transit through the entire domain can be considered as a series of infinitesimal time intervals. The residence time of the particle in a given cell is thus composed of a number of such intervals. If the sampling was carried out once in every time interval, then the number of times the particle's properties are sampled in the property sums is proportional to its residence time in the cell. The residence time in this case is simply the time taken for the particle to transit from one edge of the cell to another, or the time of intersection detailed in Section 6.5.

The number density is calculated from a sum that counts the particle at every time interval. Thus, the value added to the sum is the time of intersection, t_{int}. The velocities in each direction are calculated from the mean value of the velocity distribution function. The sum in question counts the particle velocity at every time interval, and the value added to the property sum is the product of the particle velocity and t_{int}. The temperature is calculated from the spread of the distribution function. The spread is the average distance of the particle velocity from the mean value, and the values to be summed are the product of the square of the particle velocity and t_{int}, as well as the earlier sum used for the mean velocity.

In order to obtain the macroscopic properties, the property sums must then be averaged by an appropriate quantity. The number density in a cell is simply an average of the number of particles counted in the cell at every infinitesimal time interval. Since the sums are carried out for the duration of the simulation, they must be averaged by the total time taken for all the particles to be introduced at the given fluxes. This quantity is calculated before the particle movement routine, as mentioned in Section 6.4. The number density in a cell is thus expressed through the proportionality relation:

$$n \propto \frac{\Sigma t_{int}}{t_{total}} \tag{6.18}$$

The velocity and temperature arise from the velocity distribution function. Each particle contributes once to the distribution function and hence the relevant sums must be averaged by the residence time for the particle in the cell. The velocity is obtained using:

$$< v > \propto \frac{\Sigma v t_{int}}{\Sigma t_{int}} \tag{6.19}$$

The temperature is obtained from the spread of the distribution function:

$$T \propto \frac{\Sigma v^2 t_{int}}{\Sigma t_{int}} - \left(\frac{\Sigma v t_{int}}{\Sigma t_{int}}\right)^2 \tag{6.20}$$

The sampling must be done carefully in the case of an axisymmetric simulation. Since the particles do not follow straight-line trajectories in the computational domain, the velocities perpendicular to the axis of symmetry change during the particles transit through the cell. Hence the average velocities in these directions during the transit through the cell must be the values sampled for the property sums.

Boundary sums are straightforward to sample. The boundary flux is obtained directly from the number of particles N incident on a boundary edge through the whole simulation:

$$flux = \frac{N W_p}{A t_{total}} \tag{6.21}$$

where W_p is the particle weight and A is the area of the boundary edge. The pressure, shear stress and heat flux are obtained through similar expressions for the momentum and energy transfer at the wall.

Chapter 7

Simulations Using the Line Of Sight Method

This chapter describes the application of the LOS method to the flow in the Experimental Test Facility. The results described here were obtained from a grid based LOS algorithm, which is described in Chapter 6. An emphasis was placed on using the LOS method in conjunction with the DSMC method to improve the efficiency of solutions to the flow problem. The first set of results presented in this chapter pertain to the validation of the LOS algorithm through comparisons with non-collisional DSMC simulations. The next section describes results for the flow in the ETF, which illustrate how the LOS and DSMC methods can be combined to provide an effective solution. Finally, the issues of performance and savings in computational effort are discussed.

7.1 Code validation

A task to be addressed before using the LOS method is the validation of the algorithm. This is achieved by comparing a LOS simulation of a flow problem with an equivalent DSMC simulation where collisions between particles have been disallowed. The resulting DSMC simulation does not include interactions between par-

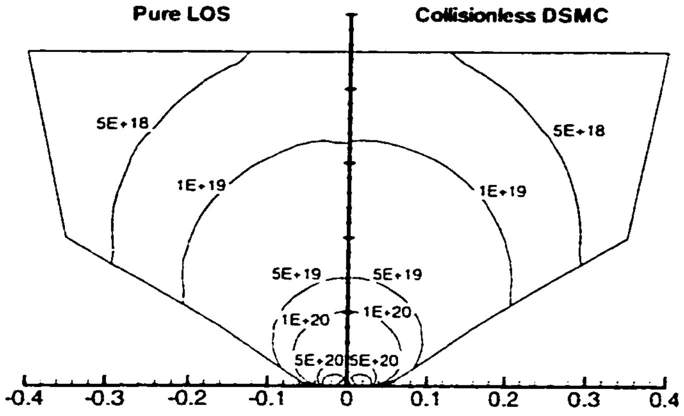

Figure 7.1. Code validation: Number density comparisons ($\#/m^3$)

ticles and performs only the particle movement routine described in Section 2.1.2. A DSMC simulation is appropriate for use as a benchmark in this case, as it has been extensively validated for many flow conditions (references in Chapter 2).

The comparisons detailed in this section pertain to simulations of the ETF domain using the LOS and collisionless DSMC methods. These results are presented in Figures 7.1 - 7.5. Figures 7.1 - 7.4 show the flow contours of the LOS simulation on the left and the collisionless DSMC simulation on the right. The contours of number density for these two methods (Figure 7.1) show very good agreement with one another, and the expansion occurs at the same rate in the two simulations. An analysis of the absolute velocity contours shows only minor differences between the two simulations. The initial expansion proceeds at the same rate. The flow contours show statistical fluctuations in the two cases, which are related to lower particle counts in the expanding domain. The magnitudes of the velocity are very comparable in the domain and the variation between the values in the two cases is less than 0.5%, which is acceptable for a margin of error.

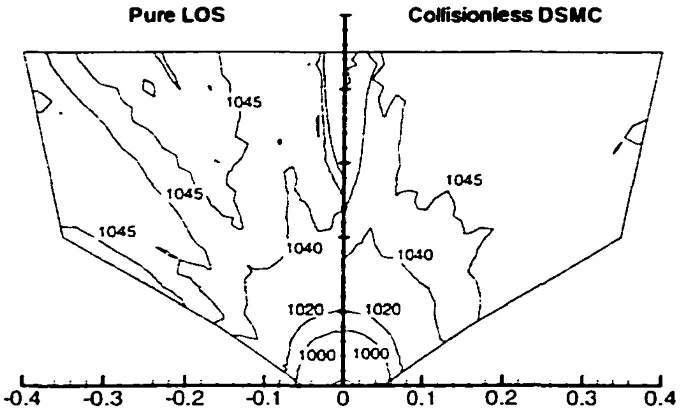

Figure 7.2. Code validation: Absolute velocity comparisons (m/s)

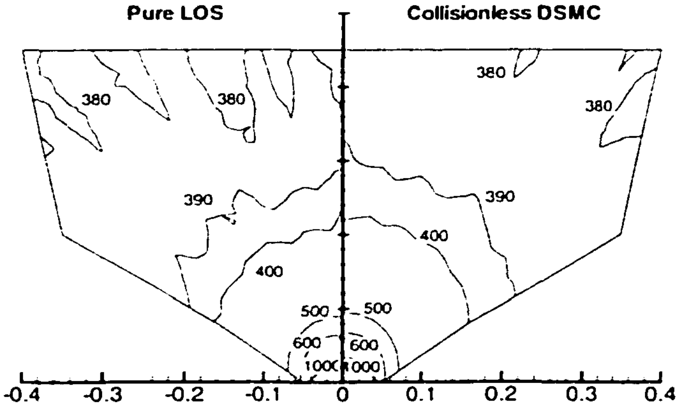

Figure 7.3. Code validation: Translational temperature comparisons (K)

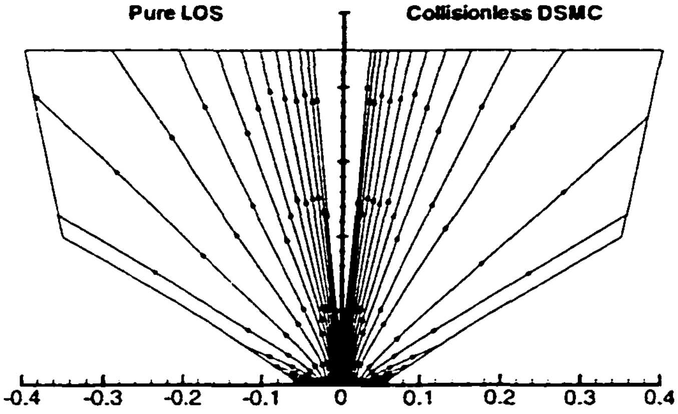

Figure 7.4. Code validation: Streamlines in the domain

The translational temperature contours (Figure 7.3) show very good agreement too. The translational temperature value decreases at the same rate in the two simulations. There are minor fluctuations in both the simulations. However, as in the case of the velocity contours, these values of the translational temperature in the flow domain are close enough to be acceptable. An analysis of the streamlines in the flow (Figure 7.4) show the expansion taking place with very similar streamline patterns. The streamlines close to the evaporating source show the curvature of the particle trajectories in the axisymmetric model. Finally, Figure 7.5 shows excellent agreement in the flux to the substrate in the two simulations.

The above discussion confirms that the LOS and collisionless DSMC model produce very similar results for the flowfield properties. Further, the computed substrate flux from a collisionless DSMC model is matched by that from the LOS method, which is much less expensive. These results validate the LOS method and prove it to be an acceptable alternative to the DSMC method in collisionless regimes.

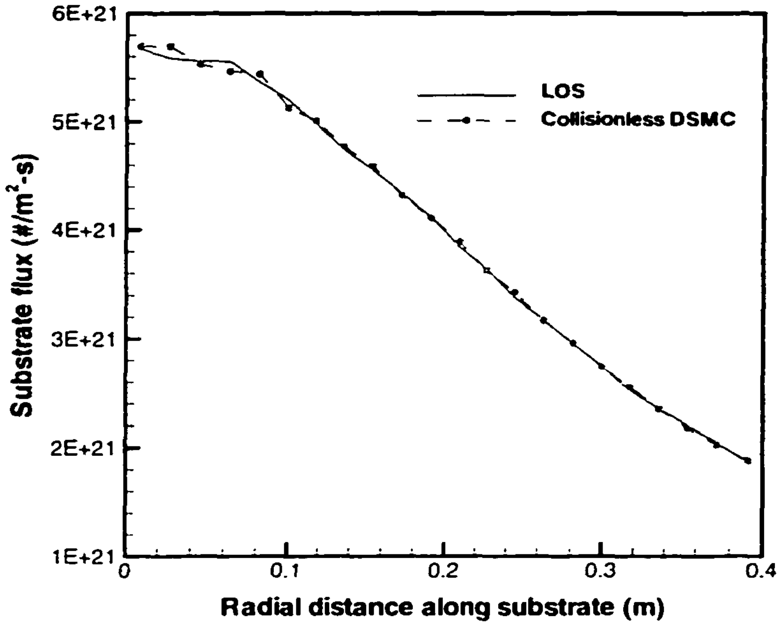

Figure 7.5. Code validation: Substrate flux comparisons ($\#/m^2s$)

7.2 The Hybrid DSMC–LOS method

The LOS method offers considerable savings in computational effort over the DSMC method. Hence it is advantageous to use it in place of a DSMC simulation, as long as the accuracy of the results is not compromised. The previous section illustrates how the LOS method offers an accurate alternative to the DSMC method for collisionless flows. However, many flow problems that are simulated using the DSMC method fall into the near-collisionless and free-molecular flow regimes. The LOS method can be used in regions of the domain where such conditions of low collisionality exist, with the DSMC method being applied to the more collisional parts of the domain. In such flows, a hybrid DSMC-LOS method would provide accurate results at a fraction of the cost. In order to obtain hybrid simulation results, it is necessary to separate the domain into collisional and collisionless parts. As mentioned earlier, the DSMC method is used on the collisional part. The resulting properties at the DSMC-LOS interface can then be used as input to the LOS simulation, where the flow is treated in a collisionless manner.

The next sub-section describes the collisionality of the ETF flow domain and the choice of the location of the interface. The following sub-section compares the results of the hybrid DSMC-LOS simulations with those of a pure DSMC simulation. The performance issues are discussed in the last sub-section.

7.2.1 Collisionality of the flow domain

As mentioned in Chapter 4, the flow in the ETF undergoes rapid expansion. The flow density drops through three orders of magnitude, the flow velocity increases and the translational temperature decreases due to the expansion. Figure 7.6 plots the collision frequency and the number density in the flow domain along the axis. The number density at the axis increases in the region immediately above the evaporating surface and then starts decreasing, because the vaporization at the axis is lower than the off-axis peak value. The collisions just above the evaporating surface scatter particles in all directions, and the particles scattered towards the axis cause the initial increase in number density. The expansion occurring beyond this region causes the rapid decrease in the number density. The collision frequency follows the same trend as the number density for the same reasons.

Figure 7.7 plots the fraction of collisions occurring upstream of an axial location in the flow domain. The ordinate is a cumulative fraction of the number of collisions in a subdomain from the evaporating source to a given axial location compared to the total number of collisions in the whole domain. This fraction increases sharply in the vicinity of the melt and then increases at a slower rate as the domain becomes

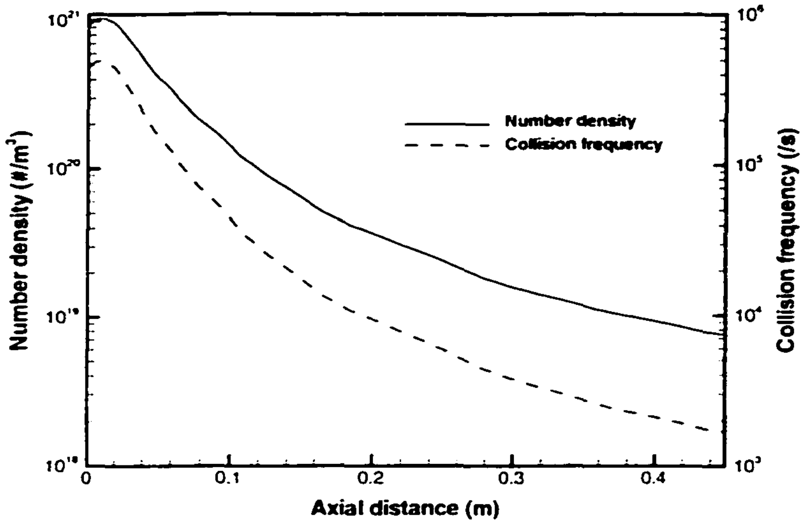

Figure 7.6. Collision frequency and number density along axis of symmetry

more and more collisionless.

The Knudsen number based on the variation in number density along the axis is shown in Figure 7.8. In this definition, the scale length used in the Knudsen number is based on the variation in number density. The relation is expressed as:

$$Kn_n = \frac{\lambda}{n/\|\frac{dn}{dx}\|} \tag{7.1}$$

The Knudsen number plot shows fluctuations due to the derivative of the number density. It is seen that this value rises sharply from the near-continuum regime value of less than 0.01 to higher values that lie in the transition regime. The plot suggests that the flow does not become entirely free-molecular. This can be seen by the fact that there are still a few collisions at the upper end of the domain, though these collisions are very few in number. Figures 7.9 and 7.10 show the variation of flow properties with the radius at the axial location of 0.3 m. It is seen from these figures, and the rest of the flow domain, that the mean free path at a certain axial location increases with increasing radius, as the number density in

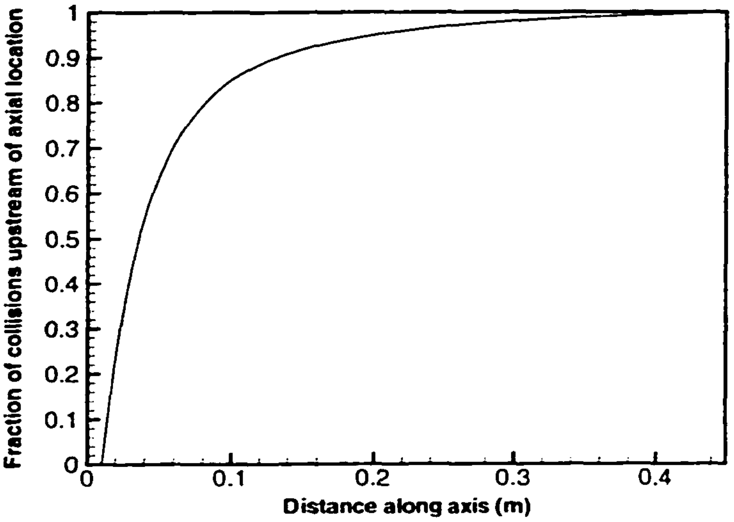

Figure 7.7. Fraction of collisions upstream of an axial location in the flow domain

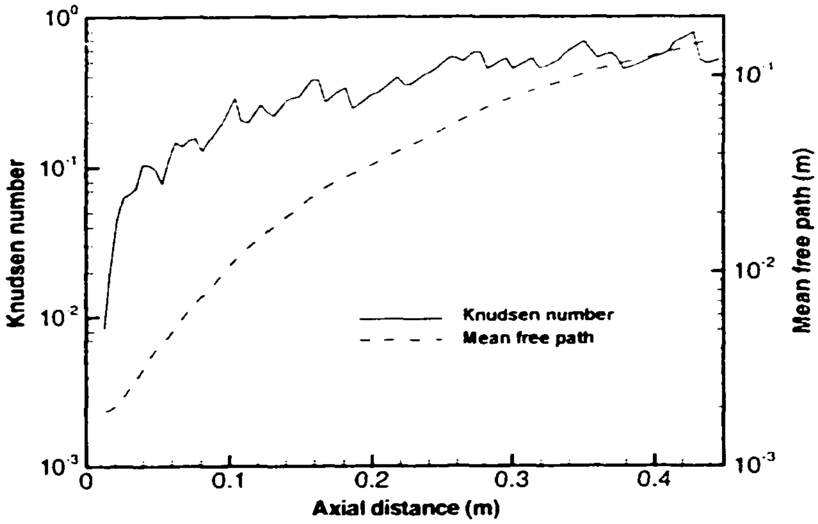

Figure 7.8. Knudsen number and mean free path along axis of symmetry

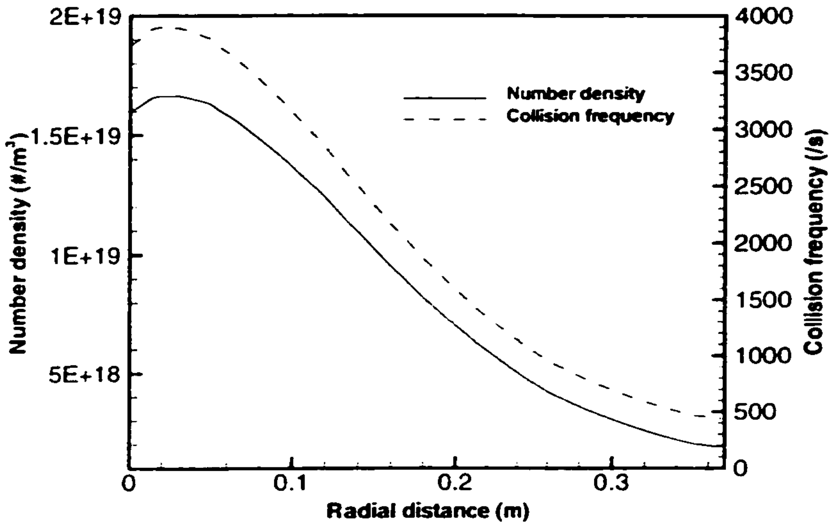

Figure 7.9. Radial variation of the number density and collision frequency at an axial location of 0.3 m

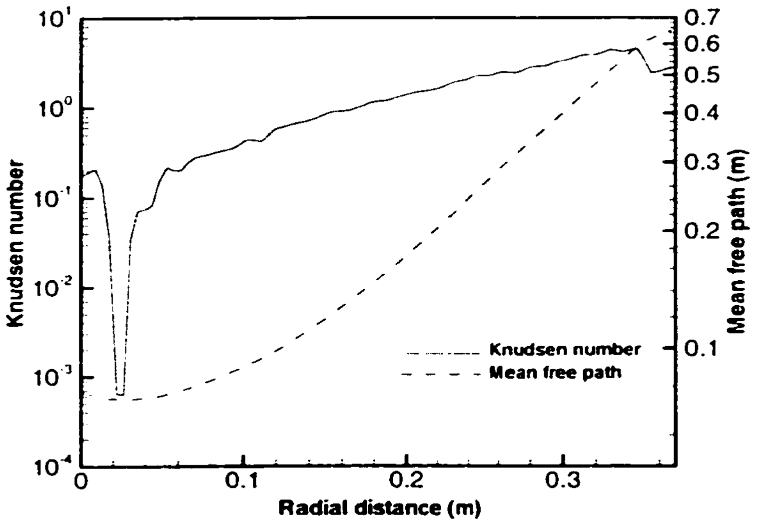

Figure 7.10. Radial variation of the Knudsen number and mean free path at an axial location of 0.3 m

Table 7.1. Collision fractions at various axial locations

Reference name	Axial location (m)	Upstream collision fraction	Mean free path (m)	Knudsen number
A	0.1	87.77 %	0.0107	0.2458
B	0.2	95.97 %	0.0355	0.3048
C	0.3	98.46 %	0.0773	0.4532

the domain decreases. The Knudsen number increases to a value of nearly 5, which indicates that the flow becomes more rarefied at the outer parts of the flow domain. The sharp drop in the Knudsen number in Figure 7.10 is due to the slight off-axis peak in the number density (Figure 7.9), which leads to very small derivatives in Equation 7.1.

For this study, four cases are considered. The first is a comparison between the DSMC simulation described in Chapter 4 and a LOS simulation of the whole domain. The next comparison is between the DSMC simulation and a hybrid DSMC-LOS simulation where the interface is located at an axial distance of 0.1 m. This simulation is referenced by the letter A for convenience. The collision fraction at this location is 0.8787, i.e. 87.87% of collisions in the flow domain occur upstream of this axial location. The third comparison has this interface located at an axial distance of 0.2 m, labeled as case B. The collision fraction at this location is 0.9597. The last comparison locates the interface at 0.3 m (case C) with a corresponding collision fraction of 0.9846. Hence, only 1.5% of all collisions in the domain occur downstream of this interface. This information for the four comparisons in summarized in Table 7.1. These comparisons provide an idea of how the collisionality of the domain affects the choice of an interface between the DSMC and LOS simulations.

7.2.2 Flowfield comparisons

The results presented in this section show comparisons between a hybrid DSMC–LOS simulation and a pure DSMC simulation. In all figures with flow contours that follow, the right half shows the results obtained through a pure DSMC simulation. The half on the left depicts the hybrid simulation under consideration.

The first case analyzed is the comparison between a pure DSMC and a pure LOS simulation. As seen in Figures 7.11 – 7.13, the flow shows a much higher degree of expansion in the DSMC simulation that includes collisions, when compared to the collisionless LOS simulation. The number density in the DSMC simulation (Figure 7.11) decreases much more than is attributable to the geometric effect of expansion, which is the mode of expansion in the LOS simulation. A closer look at Figure 7.11 shows this difference in the nature of the expansion in the two cases. The number density contours for the LOS simulation are spherical in nature, which corresponds to the collisionless, non-directed, spherical expansion from an evaporating source. On the other hand, the DSMC simulations show number density contours that are less spherical in nature. These contours indicate a directed expansion, with an axial velocity component at the source. This effect arises from the collisional region above the source, where the thermal energy of the evaporating vapor is converted to kinetic energy, with a large velocity component in the axial direction.

The region just above the evaporating source shows a much higher increase in velocity in the DSMC simulation (Figure 7.12), which is a result of the collisional

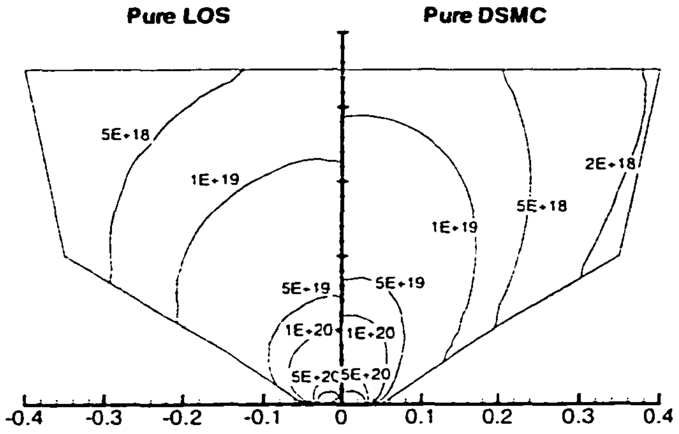

Figure 7.11. Complete LOS domain: Number density comparisons ($\#/m^3$)

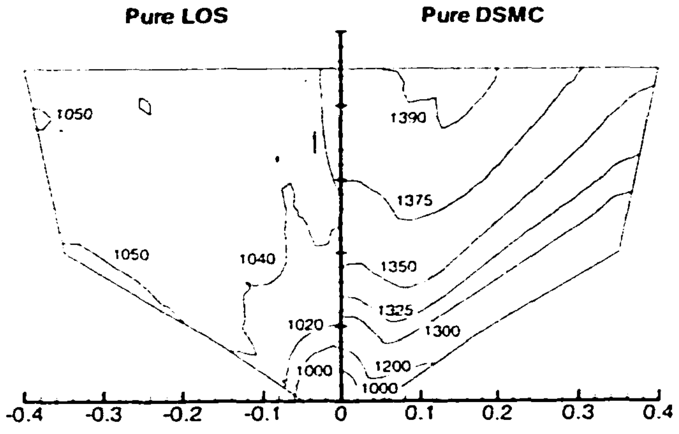

Figure 7.12. Complete LOS domain: Absolute velocity comparisons (m/s)

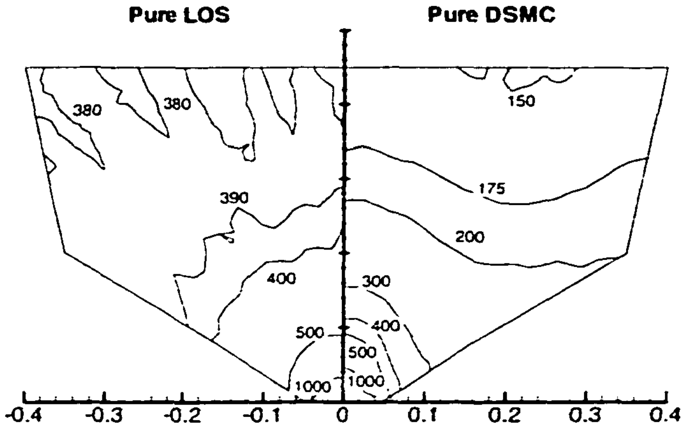

Figure 7.13. Complete LOS domain: Translational temperature comparisons (K)

interaction between particles. This factor does not contribute to the increase in velocity in the LOS simulation. As a result, the maximum velocity in the LOS simulation is more than 350 m/s (25%) lower than the corresponding maximum value in the DSMC simulation. Figure 7.13 shows how the translational temperature in the DSMC simulation is affected by the transfer of energy from the electronic mode. This energy transfer does not occur in the LOS simulation as collisions are not considered.

The substrate fluxes in the two cases (Figure 7.14) show a large discrepancy. The deposition on the substrate in the collisional DSMC simulation is nearly double that of the equivalent deposition in the LOS simulation. An analysis of the flux to the chamber walls (Figure 7.15) explains this discrepancy, as the wall flux is correspondingly lower in the DSMC simulation when compared to the LOS simulation. This difference in the calculated results arises due to the collisionality of the DSMC simulation. The collisionless, non-directed expansion in the LOS simulation allows the flow to expand more uniformly in the axial and radial directions

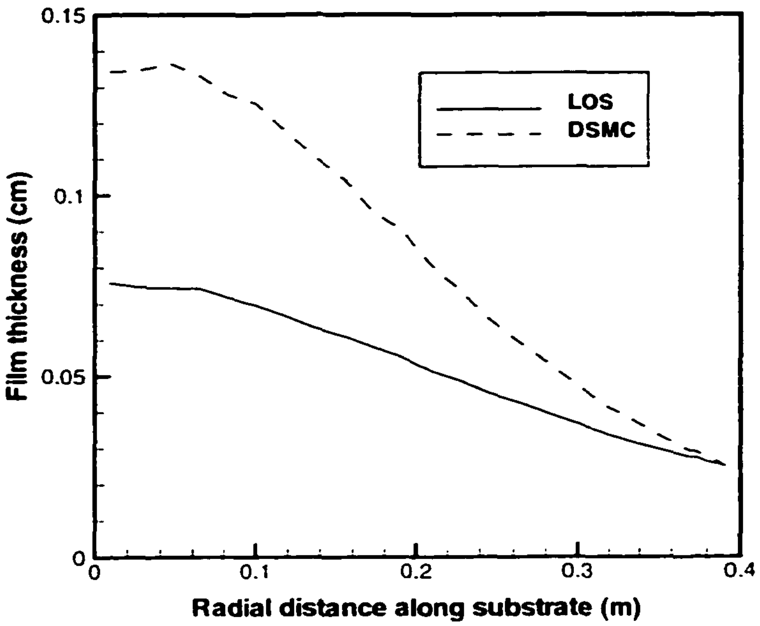

Figure 7.14. Complete LOS domain: Deposited film thickness comparisons (cm)

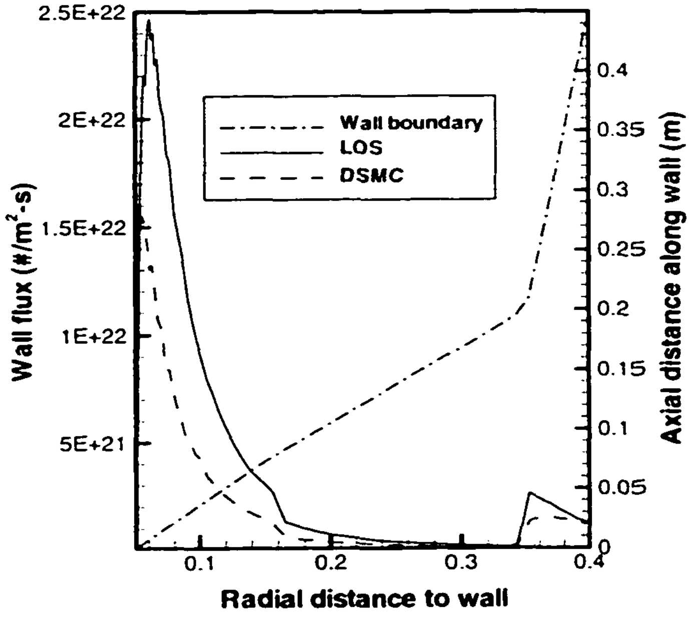

Figure 7.15. Complete LOS domain: Wall flux comparisons ($\#/m^2 - s$)

than in the DSMC simulation. This directs a larger proportion of the flow away from the axis and the substrate, thus increasing deposition on the walls. On the other hand, the collisions in the DSMC simulations direct the flow in the axial direction, thus causing a larger substrate flux.

The results presented above show that there are large differences between the collisional DSMC and collisionless LOS simulations. These variations illustrate the effect of the collisional phenomena on the expansion and deposition, and the importance of modeling the collisional interaction between the particles in the flow. Thus, a pure LOS simulation does not capture the expansion satisfactorily, and a hybrid method must be used to model the collisional region above the evaporating source.

The next case considered is the comparison of the DSMC simulation with the hybrid simulation A. As mentioned in the previous sub-section, nearly 88% of all collisions in the flow domain occur between the evaporating surface and this axial location. Hence, a significant portion of the collisional region is captured in this case through the use of the DSMC method in this region. The macroscopic flow properties calculated at the interface from the DSMC simulation are input into the LOS simulation as inflow parameters, and the LOS simulation is performed on the rest of the domain. The composite view of these simulations is presented in Figures 7.16 – 7.18.

It is seen that the flowfield properties are much closer to the corresponding values in the DSMC simulation, when compared to the results in Figures 7.11 – 7.13. The number density contours (Figure 7.16) in the hybrid simulation agree very well with their counterparts in the DSMC simulation. In this case, a directed expansion is seen in the LOS domain as the collisional phenomena are captured

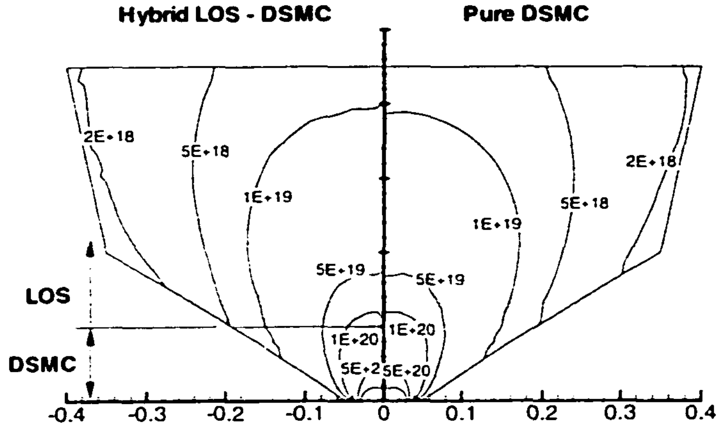

Figure 7.16. Interface at $Y = 0.1\ m$: Number density comparisons ($\#/m^3$)

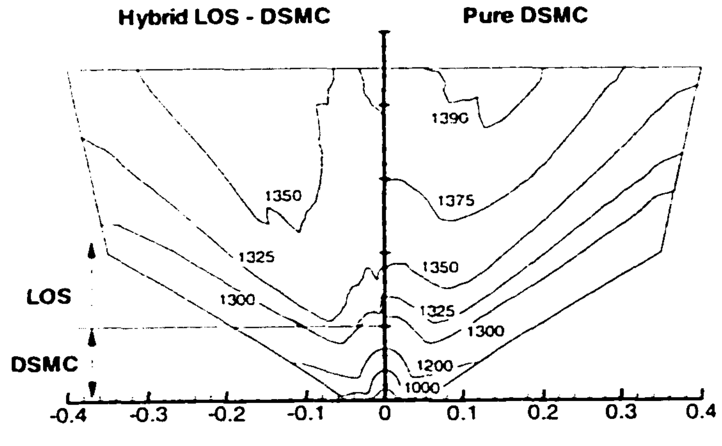

Figure 7.17. Interface at $Y = 0.1\ m$: Absolute velocity comparisons (m/s)

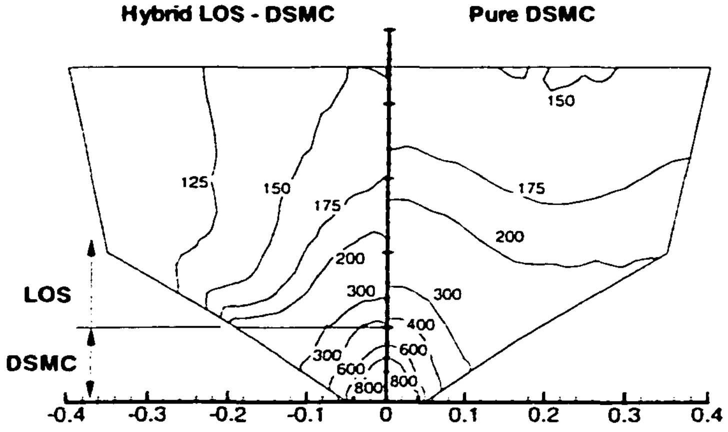

Figure 7.18. Interface at $Y = 0.1\ m$: Translational temperature comparisons (K)

to a large extent in the initial DSMC part of the hybrid simulation. The absolute velocity contours (Figure 7.12) show a slightly lower level of expansion in the LOS domain. In the pure DSMC simulation, collisional expansion continues to occur in the upper regions of the ETF, although the rate of expansion is much lower than in the region above the melt. This effect is absent in the LOS simulation. An analysis of the translational temperature contours (Figure 7.13) shows that this property decreases faster in the LOS domain than in the pure DSMC simulation. This is caused by the absence of energy transfer from the electronic to the translational energy mode in the LOS simulation. Once again, this occurs because the remainder of the collisional expansion is not captured in the LOS simulation.

The deposited thickness in the hybrid simulation shows good agreement with the pure DSMC result. There is a slight discrepancy in the two profiles though, as seen in Figure 7.19. The higher deposition in the LOS simulation is a result of the lower translational temperatures in the domain. In the pure DSMC case, the higher translational temperature is indicative of higher radial expansion, which

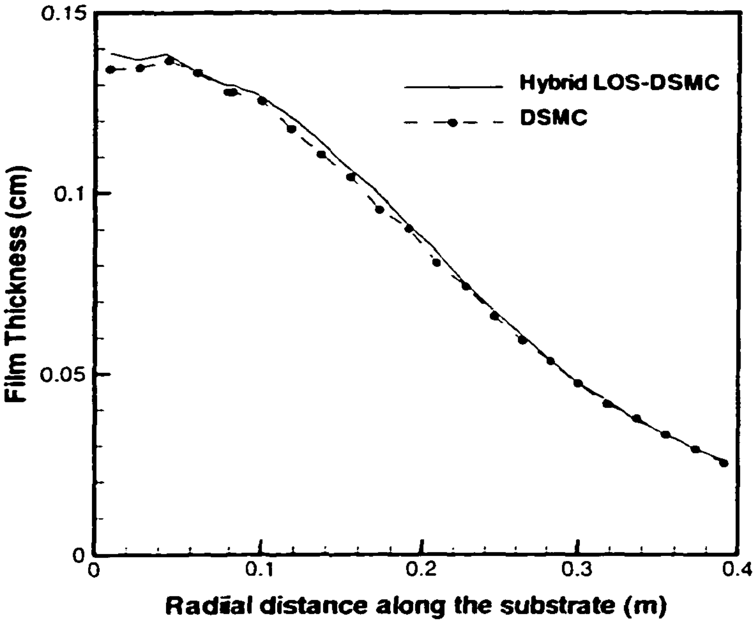

Figure 7.19. Interface at $Y = 0.1$ m: Deposited film thickness comparisons (cm)

reduces the substrate flux. The discrepancy is low because of the low values of the translational temperature in the upper part of the ETF.

The vast difference between the results from this hybrid simulation and the pure LOS simulation described earlier indicates that the modeling of the collisional region above the source is extremely important. The hybrid simulation described above captures a majority of the collisions that drive the expansion, which yields good agreement in the number density contours and deposition profiles. However, a better match for the flowfield properties can be obtained by extending the collisional DSMC domain to include a larger fraction of the collisions in the domain.

The third set of comparisons described in Figures 7.20 - 7.23 involve the hybrid simulation B, where the collisional DSMC region is extended to an axial location of 0.2 m. In this case, less than 5% of the collisions in the pure DSMC simulation are ignored in the hybrid simulation. Again, in this case, the number density

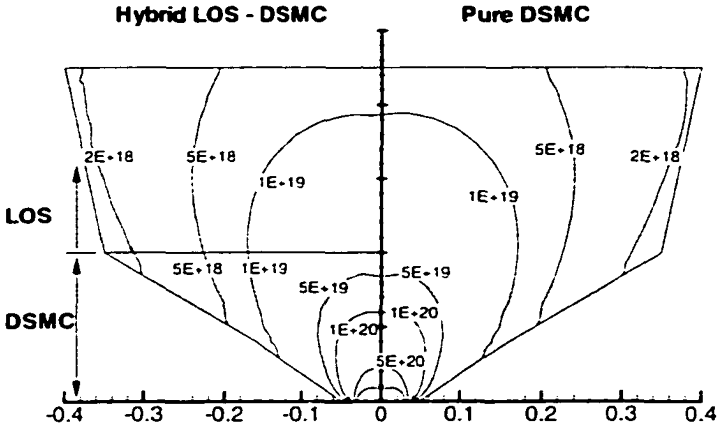

Figure 7.20. Interface at $Y = 0.2$ m: Number density comparisons ($\#/m^3$)

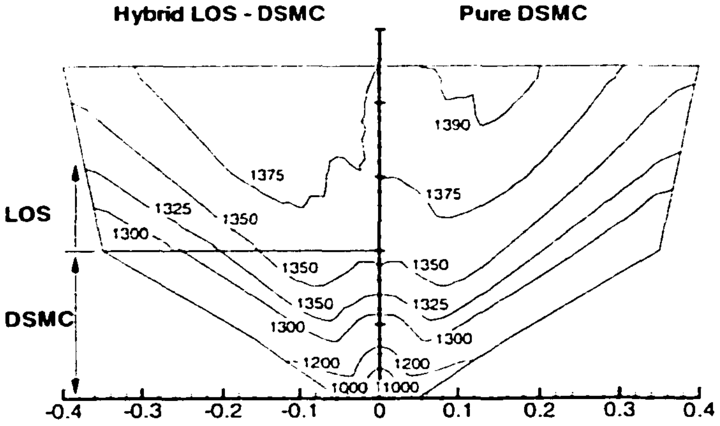

Figure 7.21. Interface at $Y = 0.2$ m: Absolute velocity comparisons (m/s)

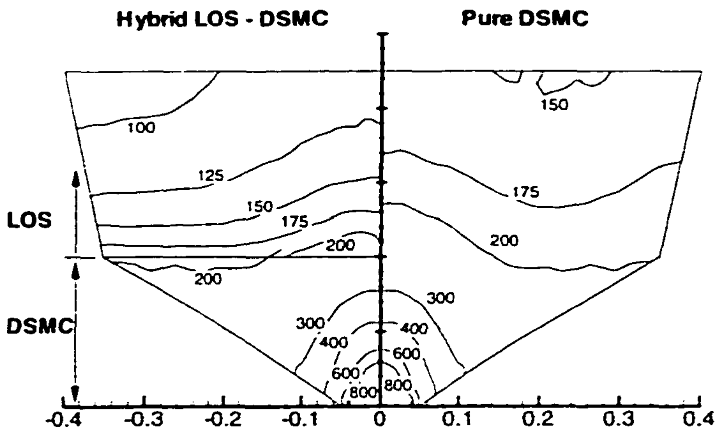

Figure 7.22. Interface at $Y = 0.2\ m$: Translational temperature comparisons (K)

contours from the hybrid simulation agree very well with the DSMC simulation (Figure 7.20). The contours indicate a directed expansion that is consistent with the collisional DSMC simulation. The number density decreases by nearly an order of magnitude in this case through the geometric effect of expansion. The absolute velocity contours (Figure 7.21) in the hybrid simulation show good agreement with their DSMC counterparts. The maximum value of the velocity in the hybrid simulation is less than 0.5% lower than the corresponding maximum value in the DSMC case, which is within an acceptable margin of error.

The translational temperatures (Figure 7.22) in the LOS domain are slightly lower than the corresponding values in the DSMC simulation. Once again, the lack of collisional energy transfer from the electronic to the translational energy mode explains this discrepancy. The results in Chapter 4 showed that the electronic temperature in this region is much higher than the translational temperature. Hence, collisions in this region result in a significant increase in the translational temperature. The collisions that have been ignored for the hybrid simulation serve this

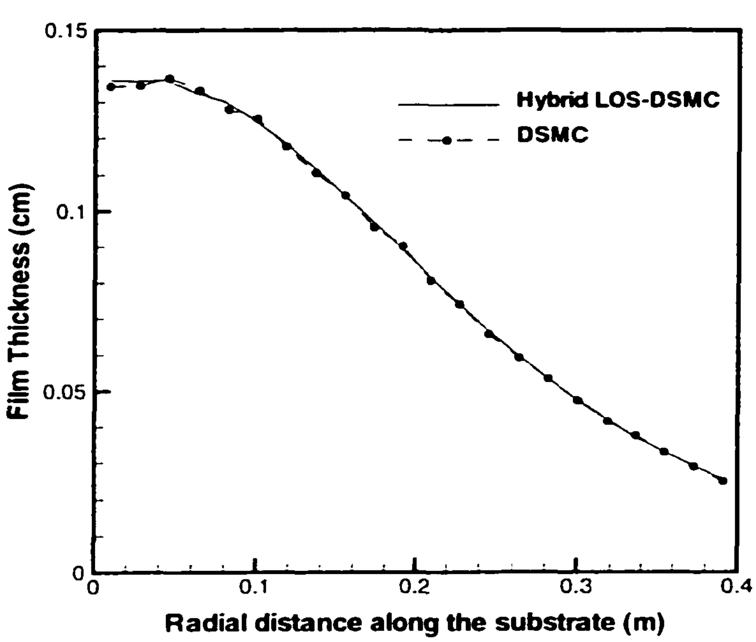

Figure 7.23. Interface at $Y = 0.2$ m: Deposited film thickness comparisons (cm)

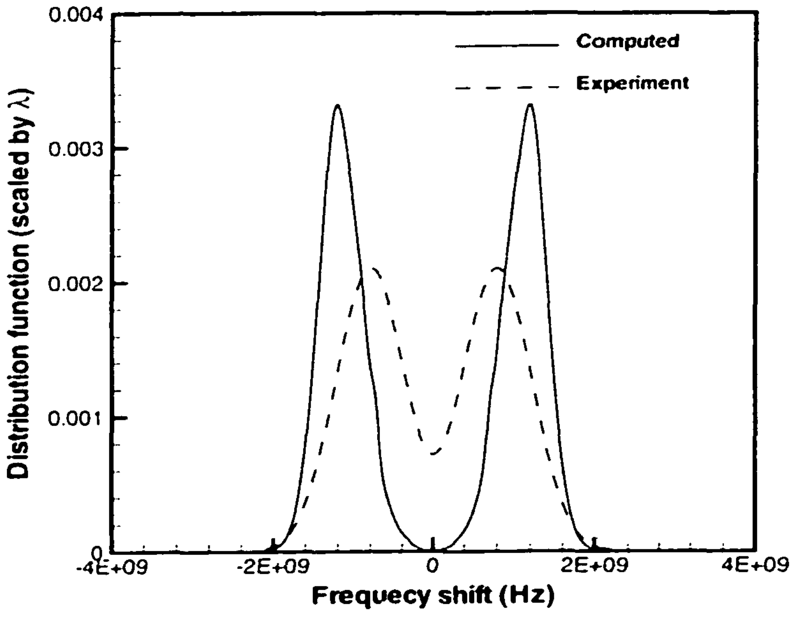

Figure 7.24. Interface at $Y = 0.2$ m: Absorption scans

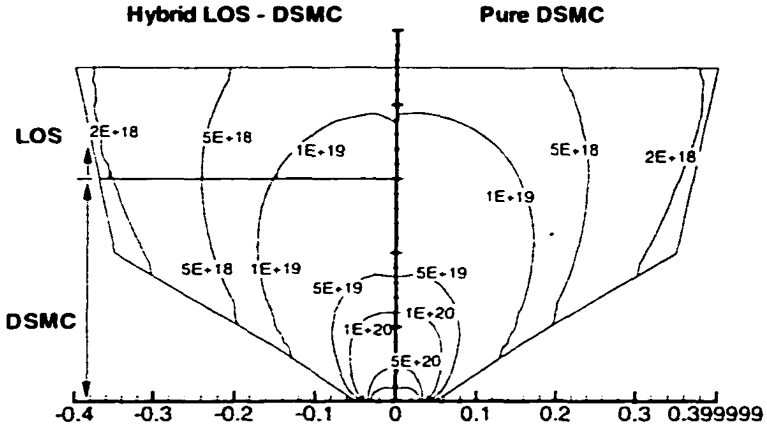

Figure 7.25. Interface at $Y' = 0.3\ m$: Number density comparisons ($\#/m^3$)

purpose. The deposited film thickness (Figure 7.23) in the hybrid simulation shows excellent agreement with the DSMC result. A comparison between the computed and experimentally measured absorption scans (Figure 7.24) shows a slight discrepancy in the perpendicular temperature and the radial velocity, but the profile is very similar to that computed using the DSMC method (Figure 5.8). These results suggest that the collisions that are modeled in the hybrid simulation capture the bulk of the expansion phenomena that contribute to the substrate flux.

Placing the interface for the hybrid simulation at this location leads to very good agreement overall between the DSMC and hybrid simulations. Since more than 95% of the collisions in the DSMC simulation are included in the LOS simulation, it is safe to say that the results reflect the collisional phenomena that are important for deposition. However, one further simulation is performed to support this argument.

The last set of results included in this section show the comparisons between the DSMC case and the hybrid simulation C. In this case, 98.5% of the collisions

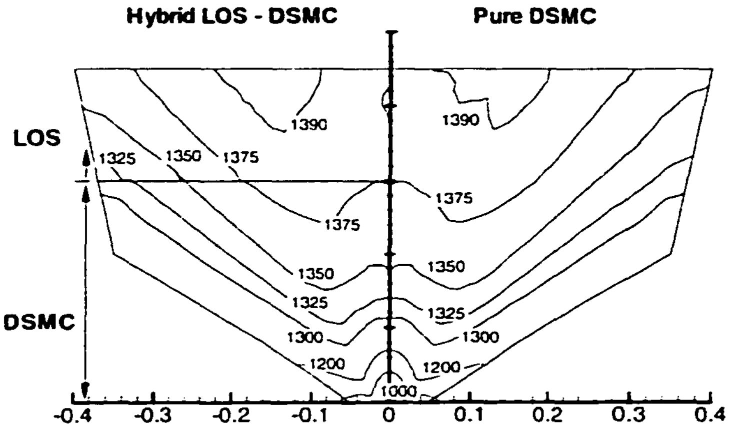

Figure 7.26. Interface at $Y = 0.3\ m$: Absolute velocity comparisons (m/s)

modeled in the DSMC simulation are included in the hybrid simulation. This is reflected in the flowfield comparisons shown in Figures 7.25 - 7.27. As in the previous set of comparisons, the number density contours calculated in the DSMC simulation are captured accurately in the LOS simulation, with the flow showing directed expansion due to the collisions modeled in the DSMC part of the hybrid simulation (Figure 7.25). The contours of absolute velocity (Figure 7.26) from the two cases show excellent agreement, and the peak values of velocity are captured accurately in the LOS domain. The translational temperature contour comparisons (Figure 7.27) still show some discrepancy. However, the comparison of the deposited film thickness on the substrate shows excellent agreement between the hybrid and DSMC simulations. Figure 7.29 shows a comparison between the computed and experimental absorption scans. The computed scan in this case shows better agreement with the experimental scan, when compared with the results from case B (Figure 7.29).

This set of results shows improvements over case B. However, the deposited film

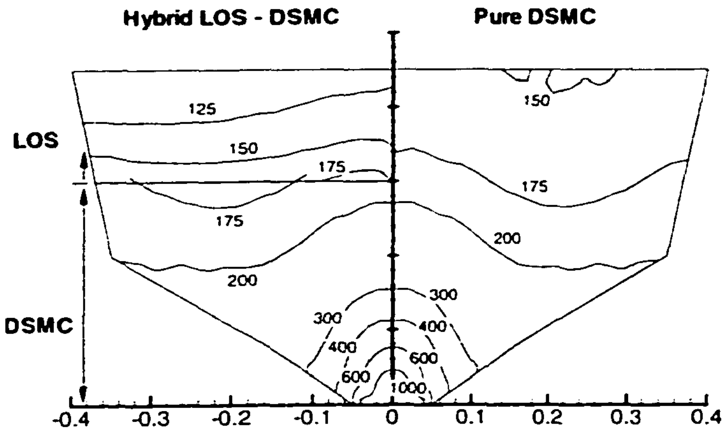

Figure 7.27. Interface at $Y = 0.3\ m$: Translational temperature comparisons (K)

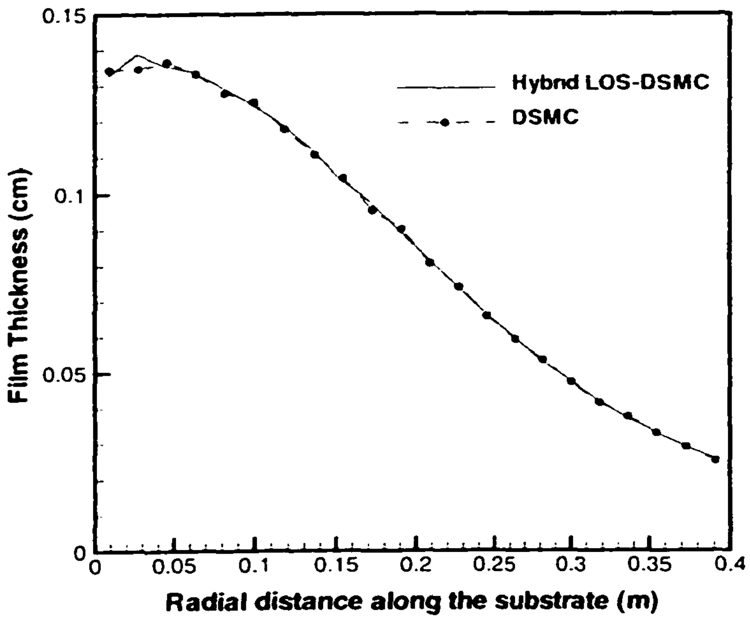

Figure 7.28. Interface at $Y = 0.3\ m$: Deposited film thickness comparisons (cm)

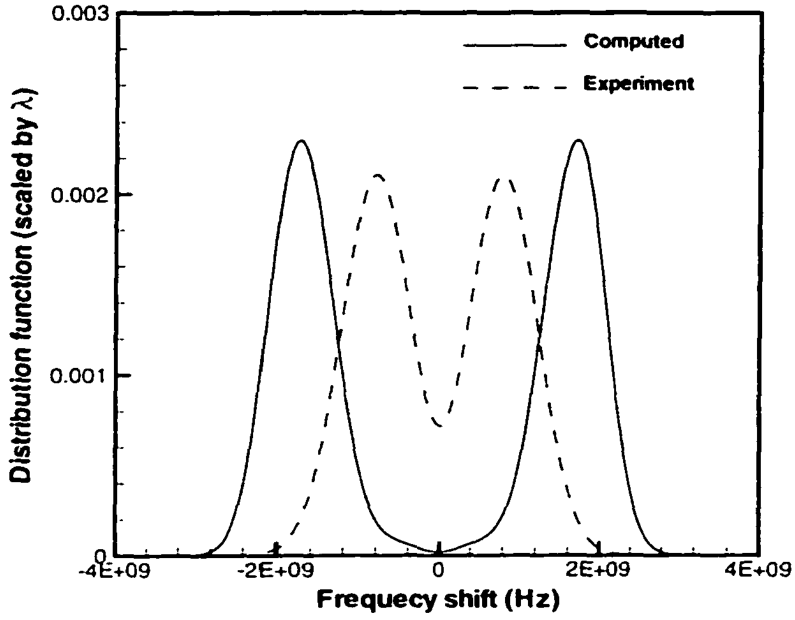

Figure 7.29. Interface at $Y = 0.3$ m: Absorption scans

thickness in the hybrid simulations B and C compare equally well with the DSMC simulation and the improvement in the flowfield properties is only marginal. This is expected as the last set of results includes only 1.5% more of all the collisions in the domain, and the important collisional phenomena driving the expansion are captured. Hence it may be advantageous to use the hybrid simulation with an interface at 0.2 m to model this system.

7.2.3 Performance comparisons

The LOS method has been developed as a cheaper and more efficient way to simulate collisionless flows, when compared to the DSMC method. In this section, the reduction in computational effort using the LOS method is quantified through comparisons with the collisionless DSMC method. It has been shown in Section 7.2.2

that simulating the ETF flow domain using the LOS method alone does not model the expansion correctly. Hence, the time savings through the use of hybrid simulations is discussed later in this section. The comparisons of computational time involved only the main loop of the LOS and DSMC algorithms, and excluded the initialization and saving of information at the end of the simulation. These routines are performed once during the simulation and the computational effort involved in their execution is minimal when compared to the main loop of the algorithm in question.

The first comparison is carried out to quantify the amount by which the LOS method outperforms a collisionless DSMC simulation. The only operations on a computational particle are the movement routines that allow the particle to translate through the flow domain. The DSMC method advances the particle through a specified time step, which often results in more than one calculation of the particle's trajectory in a specific cell during successive time steps. In contrast, the LOS method calculates the trajectory of the particle through the entire cell without the constraint of a time step. This prevents the particle from following its trajectory through a cell in a series of short hops.

The standard used to compare the performance of the LOS and DSMC movement routines is the total time taken for the computation of a single particle's trajectory in the simulation. It has been shown in Section 7.1 that the LOS and collisionless DSMC methods produce results that show very good agreement with each other. Hence, it may be assumed that the same fraction of generated particles in these simulations transit through corresponding regions of the flow domain. Therefore, the number of generated particles is a convenient parameter to use in the calculation of the standard mentioned above. This parameter has the added advantage of being easily controlled through the input data-files. In both methods, a large number of particles are generated at the inflow boundaries and are translated through the flow domain by the move routines. Assuming the time taken for all these move routines to be the total time taken for the simulation, it is possible to calculate how much time is spent, on an average, in the calculation of the move routines associated with a single particle. This is expressed as:

$$T_P = \frac{T_{TOT}}{N_P} \tag{7.2}$$

where T_P is the average time spent in the movement of a single particle through the whole simulation, T_{TOT} is the total time taken for the simulation and N_P is the total number of particles generated at the inflow.

For the LOS method, the number of particles generated is set at 1 million. The time taken for this simulation is calculated to be 977.15 seconds (16 minutes). Hence the average time spent in calculating a single particle's trajectory is 9.77×10^{-4} seconds, from Equation 7.2. The DSMC method has nearly 7.3 million particles generated through the course of the simulation, with the total simulation time being 23218.18 seconds (6 hours, 27 minutes). Hence the average time per particle in this case is 3.18×10^{-3} seconds. It is seen that in the LOS method, the calculation of a single particle's trajectory takes only 30.7% of the corresponding time in the DSMC calculation. The real time comparisons give the LOS method a savings of 96% over the DSMC method. Even if the sampling in the DSMC method is reduced by an order of magnitude the LOS simulation will be much faster than the DSMC simulation. These savings of nearly 70% of the movement calculation and an order of magnitude in the real simulation time make the LOS method extremely attractive for collisionless flows.

The next set of comparisons involves the collisional DSMC simulation of the

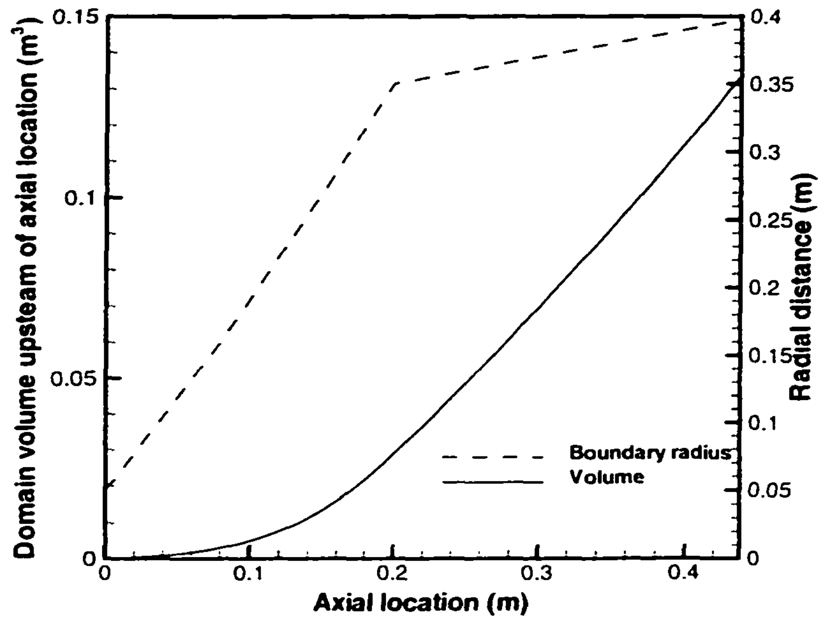

Figure 7.30. Domain volume upstream of an axial location

entire flow domain, and the three hybrid simulations described in Section 7.2. In order to compare the DSMC and hybrid simulations, the rate of particle generation at the DSMC inflow boundary is kept constant. The LOS parts of the domain also have equal numbers of generated particles. Hence, the computational savings are determined by the relative geometric parameters of the different simulations.

Two geometric parameters for the ETF are represented in Figures 7.30 and 7.31. The former shows the volume of a subdomain from the evaporating source to the axial location plotted as the ordinate. Thus, this is the volume of the DSMC part of a hybrid simulation where the interface is placed at the axial location in question. Since the domain is axisymmetric and roughly conical in nature, the upstream volume increases as the square of the radius of the chamber. The volume fractions of the DSMC parts of the three hybrid simulations are given in Table 7.2.

The cells in the domain are scaled by the mean free path of the flow. Due to the

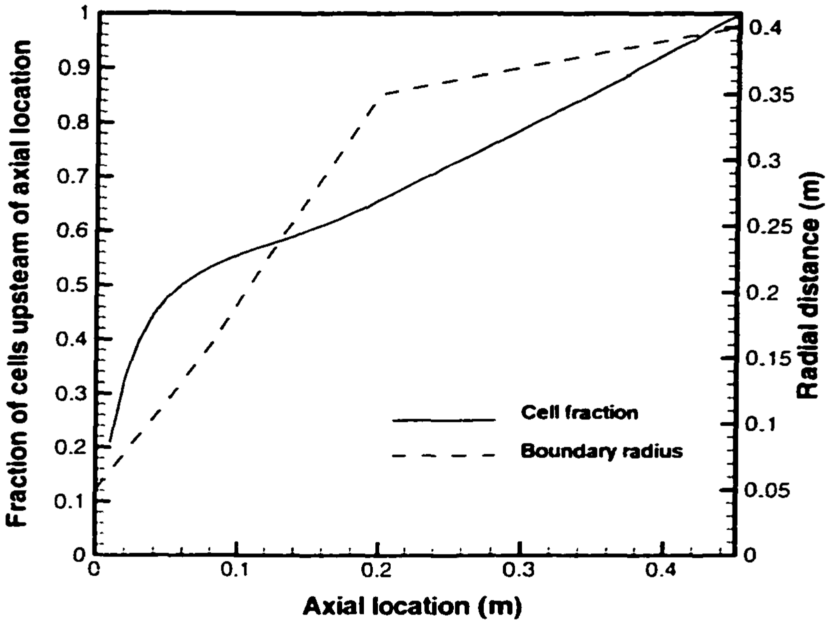

Figure 7.31. Fraction of cells upstream of an axial location

Table 7.2. Cell and volume fractions of the DSMC part of the hybrid simulations

Case	Interface location (m)	Volume fraction (%)	Cell fraction (%)
A	0.1	3.57	55.57
B	0.2	20.59	65.75
C	0.3	49.83	78.79

Table 7.3. Comparison of simulation times for the hybrid DSMC–LOS methods

	Simulation time (seconds)			Fraction of
Case	DSMC	LOS	Total	full DSMC (%)
Full DSMC	16389.37	—	16389.37	—
C	12508.01	197.64	12705.65	77.52
B	8990.22	363.09	9353.31	57.07
A	5052.35	680.67	5733.02	34.98

rapid expansion, the mean free path increases very quickly in the axial direction (Figure 7.8). Thus, the cell size also increases dramatically, as seen in the grids shown in Chapter 4 (Figures 4.1 and 4.2). The area near the evaporating source has a cluster of very small cells, while the region near the substrate has much larger cells. The number of cells upstream of an axial location in the full DSMC simulation is plotted in Figure 7.31. It is seen that the upstream cell fraction increases rapidly near the source and varies at a lower rate in the outer regions of the domain. The cell fraction data for the hybrid simulations are shown in Table 7.2.

The results of the computational time for the hybrid simulations are presented in Table 7.3. It is seen that the time taken for the LOS part of the hybrid simulation increases as the interface is placed nearer the source, as in case A. Each generated particle in this case has to pass through a larger number of cells, which increases the average time spent in the movement of each particle. This increases the overall time for the LOS simulation. However, these LOS simulation times are much smaller than the corresponding values for the DSMC simulation, which are higher by an order of magnitude. The DSMC simulation times follow the opposite trend to the LOS times for the three cases, as they simulate the complementary part of the domain. Thus, the smallest DSMC simulation, Case A, has less than one–third the simulation time of the full DSMC simulation, since it simulates roughly half the number of cells as the latter case. Case C, on the other hand has nearly 75% of the full DSMC simulation time, and it simulates particles in nearly 80% of the cells included in the full DSMC simulation. Another factor in the savings is the fact that the number of particles at any given time in the DSMC simulations decreases down the column. As particle generation rates are held constant, the number of particles in the domain is higher for larger subdomains. This does not compromise the accuracy of the smaller DSMC simulations, as the full DSMC simulation has roughly the same number of particles in the corresponding subdomain.

The total time for the hybrid simulations is dominated by the DSMC part. By comparing the simulation times for the hybrid and the full DSMC cases, it is seen that placing the interface at 0.2 m (Case B) provides the desired results 1.75 times faster than the full DSMC simulation. In real time, this translates to a savings of nearly 2 hours over the full DSMC simulation, which took more than 4.5 hours. This is a considerable savings, especially when repeated simulations are necessary. Case A produces the desired results nearly three times faster than the full DSMC simulation, corresponding to a real time savings of 3 hours over the full DSMC simulation. If the deposition profile is the only quantity that is desired, then Case A provides this result with reasonable accuracy at one–third the cost of the full DSMC simulation. Case C does not significantly improve the accuracy over Case B, and offers a speed-up of a factor of only 1.29. In this case, it is better to use configuration B when accurate flowfield predictions are required, and Case A when only the deposition profile is desired.

The hybrid simulations will have shorter execution times if a boundary based LOS method is used instead of the current grid based approach. If absorption scans are needed, a single row of cells along the laser's path could provide information on the flow properties in this region. However, the overall execution times in Table 7.3 will not change significantly as these values are dominated by the DSMC part of the simulation.

The flow in the ETF has a higher pressure than some other physical vapor deposition applications [59]. In such cases, the flow domain is even less collisional than the ETF, and the interface could be moved closer to the evaporating source without compromising accuracy. The savings in computational effort would be more dramatic in such cases than the results shown above, as the LOS part of the hybrid simulation would be quite large.

7.3 Conclusions

The Line of Sight method was developed for application to near-collisional and free molecular flow regimes. The algorithm was validated by comparing it to a collisionless DSMC simulation. The LOS results showed very good agreement with the DSMC results both for the flow field and film properties.

The flow in the ETF was investigated using a hybrid DSMC-LOS approach. A comparison of a pure LOS and a pure DSMC simulation illustrated the importance of modeling the collisional region above the evaporating source. The collisions served to convert the thermal energy of the vapor to kinetic energy, and the resulting expansion was directed axially. A pure LOS simulation did not capture this effect, and necessitated a hybrid approach.

Placing the DSMC–LOS interface at a distance of 0.1 *m* from the source captured a majority of the collisions modeled in a pure DSMC simulation. However, the remainder of the collisions caused further expansion, which was not captured adequately in this hybrid simulation. The interface was then placed at a distance of 0.2 *m* from the source. In this case, the flowfield properties compared well with the DSMC results and the substrate deposition was modeled accurately. A sufficient number of collisions were modeled to predict the expansion accurately in this case. This was verified by placing the interface at a distance of 0.3 *m* from the source. The accuracy did not improve significantly over the second hybrid simulation.

The LOS method offered a significant savings in the particle movement routine when compared to a collisionless DSMC simulation, and was faster by an order of magnitude in the simulation time. Using a hybrid DSMC–LOS method instead of a DSMC simulation offered considerable savings in computational effort. When the DSMC–LOS interface was placed 0.1 *m* from the source, the desired results were obtained nearly three times faster than the full DSMC simulation. This configuration is attractive when only the deposition profile needs to be modeled accurately. Placing the interface at 0.2 *m* increased the overall simulation speed by a factor of 1.75 without compromising the accuracy of the results. The third configuration offered an increase of a factor of 1.29 without significantly improving the accuracy over the previous case. The second configuration is thus suggested for the modeling of the flow in the ETF in a fast, accurate and efficient manner.

Chapter 8

Conclusions and Future Work

8.1 Conclusions

The physical vapor deposition of titanium was modeled in this study using the Direct Simulation Monte Carlo (DSMC) method and a collisionless Line Of Sight (LOS) technique. The electron beam evaporation of titanium from a molten pool created a source flow with a very high temperature. The relative magnitude of the translational and electronic energies at the temperatures of interest in the flow domain indicated that a significant fraction of the energy of the evaporating particles was contained in the electronic mode. Hence, a model for the consideration of electronic energy and its exchange was developed for the DSMC method, and a reduced electronic configuration of titanium was chosen for the simulation through an analysis of its energy levels. The effect of inclusion of electronic energy was studied through comparisons with simulations that did not include this mode of energy.

The evaporating flow was characterized by extremely rapid expansion. The region immediately above the evaporating surface was extremely collisional and the collisions directed the expanding vapor in the axial direction. The number density in the flow domain showed a rapid decrease through four orders of magnitude. The inclusion of electronic energy was shown to have a significant effect on the expanding flow. The energy transfer from the electronic mode increased the translational energy and the velocity of the vapor, thus increasing the expansion in the flow.

The flowfield properties showed good agreement with experimental data when electronic energy was considered. The experimental absorption spectra were modeled using the results from the DSMC simulation. Some of the discrepancy in the measured and calculated temperature was shown to arise from the presence of background argon vapor in the experimental set-up.

The expanding flow showed a high degree of non-equilibrium. The non-equilibrium behavior was studied in the Knudsen layer formed at the evaporating surface, where a finite velocity was present at the surface due to collisions in this region. The velocity and temperature along the axis of the vapor jet showed evidence of freezing, thus indicating the low collisionality of the flow away from the source.

The backscatter phenomenon was modeled in this study. This was caused by particles being scattered back into the melt through collisions. The backscatter fraction modeled was significant, and the inflow conditions were corrected by this fraction to model the experimental evaporation rate correctly. The backscatter fraction was shown to be higher when electronic energy was considered, as the additional energy of the vapor increases the collisionality of the region above the evaporating surface.

The simulations showed good agreement with the experimentally measured deposition profile. The inclusion of electronic energy caused a reduction in deposition. The translational temperature in the domain increased due to the energy transfer from the electronic mode. This in turn caused more radial expansion, thus causing more deposition on the walls and less on the substrate. The DSMC method was shown to be an important numerical tool in the modeling of vapor deposition problems, and the consideration of electronic energy in the DSMC method was shown to model the physics of the problem more accurately.

The sensitivity of the results to various parameters was investigated. The flow properties and deposition were affected significantly by changes in the collision cross section. An increase in the cross section led to an increase in the number of collisions and more radial expansion, which in turn led to reduced substrate deposition. The sticking coefficient on the walls was shown to affect the flow properties near the walls, but not the deposited film thickness. Thus, the use of a value of 1 for the sticking coefficient was validated by this study. The deformation in the surface of the molten pool was shown to have no significant effect on the expansion and the deposition.

The nature of the expanding flow led to a lot of wastage of computational effort on the near-collisionless parts of the flow. The LOS method was developed to provide a faster, cheaper and more efficient way to simulate flows with very low collisionality. This method was validated through comparisons with the results from a collisionless DSMC simulation.

A comparison of the LOS result with the DSMC simulation showed that the expansion is not captured satisfactorily using the LOS method alone. The expansion simulated in this case was spherical in nature, as opposed to the directed expansion found in the flow domain. This comparison illustrated the importance of modeling the collisional region immediately above the evaporating surface.

Hybrid DSMC-LOS simulations were modeled in order to capture the high collisionality of the initial expansion. This region was modeled using the DSMC method and the expansion in the far-field was modeled using the LOS method with input from the DSMC results. It was shown that a judicious choice of the

DSMC-LOS interface simulated the flowfield with high accuracy. The nature of the expansion was shown to be collisional near the source, and geometric in the far-field.

The LOS and hybrid simulations were compared with a pure DSMC simulation to quantify the savings in computational effort. An analysis of the particle movement routines in the LOS and collisionless DSMC simulations showed that the LOS method modeled the particle trajectory in a much more efficient manner. The use of a hybrid method decreased the computational time considerably. Thus, the vapor deposition simulations were performed in a more efficient manner without a loss of accuracy.

8.2 Future Work

The work presented in this dissertation demonstrates the modeling of the physical vapor deposition process using methods that capture the flow physics and improve the efficiency of the computation. Although the simulated results show good agreement with the experimental data, there are some discrepancies that arise in the modeling of the system. Various simplifying assumptions have been detailed in the study, and these show scope for improvement. This section outlines ways to improve the accuracy of the simulation and increase the computational efficiency of the modeling.

The collision cross section of titanium is a parameter that is not well documented in literature. Although some work has been done in this area, a considerable amount of uncertainty is present in the value of this parameter. An assumption made in this study considers the cross section of excited states to equal that of the ground state. A sensitivity analysis study has shown the simulated results to be affected considerably by the collision cross section. Hence, a useful contribution to the study of vapor deposition, and many other physical problems, would be to quantify the cross sections of the ground and excited states of titanium. This could be achieved by studying the variations of known cross sections of the ground and excited states of other elements.

The scientific community studying electron beam evaporation has long suspected that the electron beam increases the excitation of the vapor that it passed through. This effect has not been considered in the present study. Hence, a useful contribution towards understanding the process of electron beam evaporation would involve the development of a physical model for electron beam excitation. This model could use a simplistic approach towards the energy transfer from the beam to the vapor, or apply phenomenological models for energy transfer from electrons to neutral atoms through collisions.

This study does not consider spontaneous de-excitation and energy loss through photons. Hence, an extension of this study could incorporate these phenomena into the electronic energy model when the data regarding these effects are available. This study also ignores skip electrons. These electrons from the electron beam are reflected off the surface of the molten pool and typically have a lower energy than the beam. Since they undergo collisions with the vapor, they cause some excitation. Modeling the skip electrons could improve the accuracy of the simulation.

One parameter which is currently not known is the probability of energy transfer from the electronic to the translational mode. The electronic relaxation rate is also not well defined in literature. An interesting problem that arises from this would apply phenomenological modeling of these parameters to improve the accuracy of the simulated data.

The flow in the ETF shows evidence of freezing of some flow properties. Early research on the transition from a collisional to a free molecular regime has addressed the issue of freezing of the components of the translational temperature [55]. While the freezing of the parallel translational temperature occurs for a spherical flow, axisymmetric flows show a variation in this property even after the flow becomes completely collisionless [70]. The expansion in the ETF fits neither a truly axisymmetric nor a spherical model due to the off-axis nature of the source and the complexity of the domain. However, a mathematical analysis of axisymmetric freezing applied to this problem could throw some light on a parameter that could be used to decide when the flow becomes sufficiently collisionless for the LOS method to be used. In this study, a collision analysis has been performed without considering such a parameter. The development of such a parameter could provide a useful yardstick to decide where to place the interface for a hybrid DSMC-LOS simulation.

The hybrid simulations improve the efficiency of computation, but additional work can be done on improving this model. Currently, the macroscopic properties calculated from the DSMC simulation are used as input to the LOS simulation. Since the flow in the DSMC part of the hybrid domain is often in non-equilibrium, the temperature calculated has very little physical meaning. Instead of translating the particle properties in the DSMC simulation to macroscopic properties across the interface, the hybrid model could be developed to accept individual particle properties from the DSMC computations for the simulation of these particles in the LOS analysis. In the current set-up, the DSMC simulation is executed to completion, the properties are extracted and the LOS simulation is then initiated.

Although this is performed very quickly using script files, it would be a definite improvement to have the DSMC simulation feed seamlessly into the LOS simulation. A hybrid model could also be developed where the interface is adjusted adaptively during the course of the simulation, possibly through the use of the breakdown parameter mentioned earlier.

This work has extremely practical applications in the materials processing industry, with a potential for simulations with quick turn-around times. The incorporation of some of these suggestions would increase the accuracy and efficiency of the method developed in this study. This would help extend the envelope in the modeling of physical vapor deposition problems.

Bibliography

[1] Abe, T., Inelastic Collision Model for Vibrational–Translational and Vibrational–Vibrational Energy Transfer in the Direct Simulation Monte Carlo Method, *Physics of Fluids*, Vol. 6, No. 9, 1994, pp. 3175–3179.

[2] Anderson, J. B., Fenn, J. B., Velocity Distributions in Molecular Beams from Nozzle Sources, *Physics of Fluids*, Vol. 8, No. 5, 1965, pp. 780–787.

[3] Anderson, J. B., Foch, J. D., Shaw, M. J., Stern R. C., and Wu, B. J., *Proceedings of the 15th International Symposium on Rarefied Gas Dynamics*, Vol. 2, 1986, pp. 413.

[4] Andrews, D. L., ed., *Applied Laser Spectroscopy: Techniques, Instrumentation and Applications*, VCH Publishers, Inc., 1992.

[5] Asano, T., Uetake, N., and Suzuki, K., Mean Atomic Velocities of Uranium, Titanium and Copper during Electron–Beam Evaporation *Journal of Nuclear Science and Technology*, Vol. 29, No. 12, 1992, pp. 1194–1200.

[6] Ashby, M. F., and Jones, D. R. H., *Engineering Materials 1: An Introduction to their Properties and Applications*, Pergamon Press, New York, 1980.

[7] Baganoff, D. and McDonald, J. D., A Collision Selection Rule for a Particle Simulation Method Suited to Vector Computers, *Physics of Fluids*, Vol. 2, No. 7, 1990, pp. 1248–1259.

[8] Bakish, R., ed., *Introduction to Electron Beam Technology*, John Wiley & Sons, Inc., 1962.

[9] Balakrishnan, J., Boyd I. D., and Braun, D. G., Monte Carlo Simulation of Vapor Transport in Physical Vapor Deposition of Titanium, *Journal of Vacuum Science and Technology A - Vacuum Surfaces and Films*, Vol. 18, No. 3, 2000, pp. 904–916.

[10] Bartel, T. J., Low Density Gas Modeling in the Microelectronics Industry., In *Rarefied Gas Dynamics*, 1995, pp. 611.

[11] Bergemann, F. and Boyd, I. D., DSMC Simulation of Inelastic Collisions using the Borgnakke-Larsen Method Extended to Discrete Distributions of Vibrational Energy, *Progress in Astronautics and Aeronautics, AIAA*, Vol. 158, 1994, p. 174.

[12] Bhatnagar, P. L., Gross, E. P. and Krook, M., A Model for Collision Processes in Gases — *I.* Small Amplitude Processes in Charged and Neutral One-Component Systems, *Physical Review Letters*, 1954, Vol. 94, No. 3, p. 511.

[13] Bird, G. A., *Molecular Gas Dynamics*, Clarendon Press, Oxford, 1994.

[14] Bird, G. A., *Molecular Gas Dynamics and the Direct Simulation of Gas Flows*, Oxford University Press, 1994.

[15] Bird, G. A., Shock Wave Structure in a Rigid Sphere Gas, In *Rarefied Gas Dynamics*, Vol. 1, 1965, pp. 216–222.

[16] Bird, G. A., Approach to Translational Equilibrium in a Rigid Sphere Gas, *Physics of Fluids*, Vol. 6, 1963, pp. 1518–1519.

[17] Bird, G. A., Direct Simulation Monte Carlo Method — Current Status and Prospects, In *Rarefied Gas Dynamics*, Vol. 1, 1969, pp. 85–98.

[18] Bird, G. A., The Formation and Reflection of Shock Waves, In *Rarefied Gas Dynamics*, Vol. 1, 1969, pp. 301–311.

[19] Bird, G. A., The Velocity Distribution Function Within a Shock Wave, *Journal of Fluid Mechanics*, Vol. 30, Part 3, November 1967, pp. 479–487.

[20] Bird, G. A., The Structure of Rarefied Flows Past Simple Aerodynamic Shapes, *Journal of Fluid Mechanics*, Vol. 36, Part 3, May 1969, pp. 571–576.

[21] Bird, G. A., Direct Simulation and the Boltzmann Equation, *Physics of Fluids A*, Vol. 13, No. 11, 1970, pp. 2676–2681.

[22] Bird, G. A., Breakdown of Translational and Rotational Equilibrium in Gaseous Expansions, *AIAA Journal*, Vol. 8, No. 11, November 1970, pp. 1997–2003.

[23] Bird, G. A., Monte Carlo Simulation of Gas Flows., *Annual Review of Fluid Mechanics* Vol. 10, 1978, pp. 11.

[24] Bird, G. A., Monte-Carlo simulation in an engineering context, In *Rarefied Gas Dynamics*, 1980, pp. 239–255.

[25] Bird, G. A., Direct Simulation of High-Vorticity Gas Flows, *Physics of Fluids*, Vol. 30 ,No. 2, 1986, pp. 364-366.

[26] Bird, G. A., Perception of Numerical Methods in Rarefied Gas Dynamics., In *Rarefied Gas Dynamics*, 1988, pp. 211.

[27] Birdsall, C. K. and Langdon, A. B., *Plasma Physics Via Computer Simulation*, Adam Hilger, 1991.

[28] Borgnakke, C. and Larsen, P. S., Statistical Collision Model for Monte Carlo Simulation of Polyatomic Gas Mixtures, *Journal of Computational Physics*, Vol. 18, 1975, pp. 405–420.

[29] Boyd, I. D., Rotational–Translational Energy Transfer in Rarefied Nonequilibrium Flows. *Physics of Fluids A*, Vol. 2, No. 3, 1990, pp. 447–452.

[30] Boyd I. D., Analysis of Rotational Nonequilibrium in Standing Shock Waves of Nitrogen, *AIAA Journal*, Vol. 28, November 1990, pp. 1997–1998.

[31] Boyd, I. D., Analysis of Vibrational-Translational Energy Transfer Using the Direct Simulation Monte Carlo Method, *Physics of Fluids A*, Vol. 3, No. 7, 1991, pp. 1785–1791.

[32] Boyd I. D., Candler, G. V., and Levin, D. A., Dissociation Modeling in Low Density Flows of Air, *Physics of Fluids*, Vol. 7, 1995, pp. 1757–1763.

[33] Boyd I. D., Jafry, Y. and Vanden Beukel, J., Particle Simulations of Helium Microthruster Flows, *Journal of Spacecraft and Rockets*, Vol. 31, 1994, pp. 271–277.

[34] Boyd, I. D. and Gokcen, T., Computation of Axisymmetricand Ionized Hypersonic Flows Using Particle and Continuum Methods, *American Institute of Aeronautics and Astronautics Journal*, Vol. 32, No. 9, 1994, pp. 1825–1835.

[35] Boyd, I. D., Conservative Species Weighting Scheme for the Direct Simulation Monte Carlo Method, *Journal of Thermophysics and Heat Transfer*, Vol. 10, No. 4, October–December 1996, pp. 579–585.

[36] Boyd, I. D., VanGilder, D.B., and Beiting, E.J., Computational and Experimental Investigations of Rarefied Flows in Small Nozzles. *AIAA Journal*, Vol. 34 (11), 1996, pp. 2320–2326.

[37] Boyd I. D., Extensive Validation of a Monte Carlo Model for Hydrogen Arcjet Flowfields, *Journal of Propulsion and Power*, Vol. 13, 1997, pp. 775–782.

[38] Boyd, I. D., VanGilder, D.B., and Liu, X., Monte Carlo Simulation of Neutral Xenon Flows in Electric Propulsion Devices, *Journal of Propulsion and Power*, Vol. 14 (6), 1998, pp. 1009–1015.

[39] Braun, D. G., Anklam, T. M., Berzins, L. V., Blackfield, D. T., McClelland, M. A., Meier, T. C., Boyd, I. D. and Balakrishnan, J., *Electron Beam Melting and Refining Conference*, 1998.

[40] Braun, D. G., *Private Communication*

[41] Bunshah, R. F., ed. *Handbook of Deposition Technologies for Films and Coatings*, Noyes Publications, Park Ridge, NJ, 1994.

[42] Carlson, A. B. amd Hassan, H.A., Radiation Modeling with Direct Simulation Monte Carlo, *Journal of Thermophysics and Heat Transfer*, Vol. 6, No. 5, 1992, pp. 631–636.

[43] Chaleix, D., Choquet, P., Bessaudou, A., Frugier, L., and Machet, J., A Spatial Distribution Study of a Beam Vapour Emitted by Electron–Beam Heated Evaporation Sources, *Journal of Physics D – Applied Physics*, Vol. 29, No. 1, 1996, pp. 218–224.

[44] Chatain, S., Gonella, C., and Roblin, P., Experimental Results and Monte Carlo Simulations for a Gadolinium Atomic Beam Produced with a Focussed Electron Gun, *Journal of Physics D – Applied Physics*, Vol. 30, No. 3, 1997, pp. 360–367.

[45] Chen, F. F., *Introduction to Plasma Physics and Controlled Fusion*, Plenum Press, 1984.

[46] Chen, G., Boyd, I. D., Roadman, S. E., and Engstrom, J. R., Monte Carlo Analysis of a Hyperthermal Silicon Deposition Process, *Journal of Vacuum Science and Technology A – Vacuum Surfaces and Films*, Vol. 16, No. 2, 1998, pp. 689–699.

[47] Chen, G. and Boyd, I. D., Statistical Error Analysis for the Direct Simulation Monte Carlo Technique, *Journal of Computational Physics*, Vol. 126, No. 2, 1996, pp. 434–448.

[48] Chen, G., Direct Simulation Monte Carlo Modeling of Silicon Thin Film Deposition using Supersonic Beams, Ph. D. thesis, Cornell University, May 1998.

[49] Clyne, T. W., and Withers, P. J., *An Introduction to Metal Matrix Composites*, Cambridge University Press, 1993.

[50] Coronell, D. G. and Jensen, K. F., Analysis of Transition Regime Flows in Low Pressure Chemical Vapor Deposition Reactors Using the Direct Simulation Monte Carlo Method., *Journal of the Electrochemical Society*, Vol. 139, No. 8, 1992, pp. 2264-2273.

[51] Dietrich, S. and Boyd I. D., Scalar and Parallel Optimized Implementation of the Direct Simulation Monte Carlo Method, *Journal of Computational Physics*, Vol. 126, 1996, pp. 328–342.

[52] Dietrich, S. and Boyd, I. D., Loadbalancing for the DSMC Method on Parallel Computers, *Proceedings of the 19th International Symposium on Rarefied Gas Dynamics*, Oxford University Press, 1995.

[53] Economou, D. J., Bartel, T. J., Wise, R. S. and Lymberopoulos, D. P., Two-Dimensional Direct Simulation Monte Carlo (DSMC) of Reactive Neutral and Ion Flow in a High Density Plasma Reactor., *IEEE Transactions on Plasma Science*, Vol. 23, No. 4, 1995, pp. 581-591.

[54] Economou, D. J. and Bartel, T. J., Direct Simulation Monte Carlo (DSMC) of Rarefied Gas Flow during Etching of Large Diameter (300-mm) Wafers, *IEEE Transactions on Plasma Science*, Vol. 24, No. 1, 1996, pp. 131.

[55] Edwards, R. H., and Cheng, H. K., Steady Expansion of a Gas into a Vacuum *AIAA Journal*, Vol. 4, No. 3, 1966, pp. 558-561.

[56] El-Kerah, B., *Fundamentals of Semiconductor Processing Technology*, Kluwer Academic Publishers, Boston, 1995.

[57] Erikson, E. D., Thickness Distribution of a Metal Alloy from a High Rate Electron Beam Source, *Journal of Vacuum Science and Technology*, Vol. 11, No. 1, 1974, pp. 366-370.

[58] Fallavollita, M. A., Baganoff, D. and McDonald, J. D., Reduction of Simulation Cost and Error for Particle Simulations of Rarefied Flows. *Journal of Computational Physics*, Vol. 109, 1993, pp. 30-36.

[59] Fan, J., Cai, C. P. and Boyd, I. D., Direct Simulation Methods for Low-Speed Micro-Channel FLows, AIAA Paper 99-3801, June 1999.

[60] Fan, J., Boyd, I. D., and Sheldon, C., Monte Carlo Modeling of Electron Beam Physical Vapor Deposition of Yttrium, *Journal of Vacuum Science and Technology A - Vacuum Surfaces and Films*, Vol. 18, No. 6, 2000.

[61] Fleche, J. L , Gonella, C., Blumenfeld, L., Morin, M. and Gaveau, M. A., Measurement and Interpretation of the Atomic Vapor Velocities Produced by Electron Bombardment, *Proceedings of the 18th International Symposium on Rarefied Gas Dynamics*, 1992, pp. 67-76.

[62] Fleche, J. L , and Gonella, C., DSMC Simulation of Overheating through Atomic Inelastic Collisions in a Metal Vapour Jet Expansion, *Proceedings of the 19th International Symposium on Rarefied Gas Dynamics*, 1994, pp. 542-548.

[63] Fleche, J. L ,Saunois, P., and Guilbaud, D, Effect of the Backscattered Vapor Pressure on the Temperature Field of a Metal Heated by an Electron Beam, *Proceedings of the 21st International Symposium on Rarefied Gas Dynamics*, 1998, pp. 453-460.

[64] Font, G. I. and Boyd I. D., Numerical Study of the Effects of Reactor Geometry on a Chlorine Helicon Etch Reactor, AIAA Paper 96-0591, January 1996.

[65] Font, G. I., Boyd I. D. and Balakrishnan, J., Effects of Wall Recombination on the Etch Rate and Plasma Composition of an Etch Reactor, *Journal of Vacuum Science and Technology A-Vacuum Surfaces and Films*, Vol. 16, No. 4, 1998, pp. 2057–2064.

[66] Greenland, P. T., Laser Isotope Separation, *Contemporary Physics*, Vol. 31, No. 6, 1990, pp. 405–424.

[67] Groves, J. F., Directed Vapor Deposition, Ph. D. thesis, University of Virginia, 1998.

[68] Halpern, B. L., and Schmitt, J. J., Multiple Jets and Moving Substrates: Jet Vapor Deposition of Multicomponent Thin Films, *Journal of Vacuum Science and Technology A*, Vol. 12, No. 4, 1994, pp. 1623-1627.

[69] Hamel, B. B., A Model for the Transition Regime in Hypersonic Rarefied Gasdynamics, *AIAA Journal*, Vol. 2, No. 6, June 1964, pp. 1047–1054.

[70] Hamel, B. B., Kinetic Theory of Source Flow Expansion with Application to the Free Jet, *Physics of Fluids*, Vol. 9, No. 5, 1966, pp. 829-841.

[71] Hargus, W. A. and Cappelli, M. A., The Structure of an Expanding Hydrogen Arcjet Plasma, *Physics of Plasmas*, Vol. 5, No. 12, 1998, pp. 4488-4497.

[72] Hassan, H. A. and Hash, D. B., A Generalized Hard-Sphere Model for Monte Carlo Simulation., *Physics of Fluids A*, Vol. 5, No. 3, 1993, pp. 738-744

[73] Herzberg, G., *Atomic Spectra and Atomic Structure*, Dover Publications, 1945.

[74] Hill, R. J., ed. *Physical Vapor Deposition*, The BOC Group, Inc., Berkeley, CA, 1986.

[75] Hughes, J. L., Making Alloy Foils by Electron Beam Evaporation, *Metals Engineering Quarterly*, Vol. 1, 1974.

[76] James, A. S., Robinson, P. A., and Matthews ,A., A Practical Model to Enable the Prediction of Coating Thickness Variations across a Flat Surface, *Surface and Coatings Technology*, Vol. 59, No. 1-3, 1993, pp. 48-53.

[77] Kannenberg, K., Computational Methods for the Direct Simulation Monte Carlo Technique with Application to Plume Impingement, Ph. D. thesis, Cornell University, May 1998.

[78] Karipides, D. P., Detailed Investigation of Spacecraft Glow, Ph. D. thesis, Cornell University, May 1999.

[79] Keidar, M. and Boyd, I. D., Effects of a Magnetic Field on the Plasma Plume from Hall Thrusters, *Journal of Applied Physics*, Vol. 86, No. 9, 1999, pp. 4786–4791.

[80] Knight, C. J., Evaporation from a Cylindrical Surface into Vacuum, *Journal of Fluid Mechanics*, Vol. 75, Part 3, 1976, pp. 469–486.

[81] Knight, C. J., Theoretical Modeling of Rapid Surface Vaporization with Back Pressure, *AIAA Journal*, Vol. 17, No. 5, 1979, pp. 519–523.

[82] Koura, K. and Matsumoto, H., Variable Soft Sphere Molecular Model for Inverse–Power–Law or Lennard–Jones Potential, *Physics of Fluids A*, Vol. 3, No. 10, May 1991, pp. 2459–2465.

[83] Koura, K. and Matsumoto, H., Variable Soft Sphere Molecular Model for Air Species, *Physics of Fluids A*, Vol. 4, No. 5, May 1992, pp. 1083–1085.

[84] Kusamichi, T., Kanayama, H., and Onoye, T., Temperature Measurement of Molten Metal Surface in Electron Beam Melting of Titanium Alloys, *ISIJ International*, Vol. 32, No. 5, 1992, pp. 593–599.

[85] Laemmerman, H., and Kienel, G., PVD Coatings for Aircraft Turbine Blades, Advanced Materials and Processes, Vol 12, 1991, pp. 18.

[86] Lieberman, M. A., and Lichtenberg, A. J., *Principles of Plasma Discharges and Materials Processing*, John Wiley & Sons, Inc., 1994.

[87] Lohner, R., An Adaptive Finite Element Scheme for Transient Problems in CFD (Computational Fluid Dynamics) *Computer Methods in Applied Mechanics and Engineering*, Vol. 61, No. 3, 1987, pp. 323–338.

[88] Maissel, L. I., and Glang, R., *Handbook of Thin Film Technology*, McGraw Hill Book Company, New York, 1970.

[89] Matsumoto, H., Test of Efficiency of Variable Soft Sphere and Variable Hard Sphere Molecular Modelsin the Direct Simulation Monte Carlo Method, *JSME International Journal*, Series B, Vol. 40, No. 4, May 1997, pp. 529–535.

[90] McCullogh, C., Storer, J., and Berzins, L. V., Manufacture of Orthorhombic Titanium Aluminide Composites by PVD Methods, *Recent Advances in Titanium Metal Matrix Composites* ed. Froes, F. H., and Storer, J., Warrendale, PA, 1995, pp. 259.

[91] Meiburg, E., Comparison of Molecular Dynamics Method and teh Direct SImulation Monte Carlo Technique for Flows around Simple Geometries *Physics of Fluids*, Vol. 29, No. 10, 1986, pp. 3107–3113.

[92] Meier, S. M., and Gupta, D. K., The Evolution of Thermal Barrier Coatings in Gas Turbine Engine Applications, *Transactions of the ASME*, Vol. 116, 1994, pp. 250.

[93] Menzel. E. R., *Laser Spectroscopy Techniques and Applications*, Marcel Dekker, Inc., 1995.

[94] Moore, C. E., *Atomic Energy Levels As Derived From the Analyses of Optical Spectra*, Vol. 1–3, Circular of the National Bureau of Standards 467, 1949, 1952, 1958.

[95] Muller, J.-D., Roe, P. L., and Deconinck, H., A Frontal Approach for Internal Node Generation in Delaunay Triangulations, *International Journal for Numerical Methods in Fluids*, vol. 17, No. 3, 1993, pp. 241-255.

[96] Nance,R. P., Hash. D. B. and Hassan, H. A., Role of boundary conditions in Monte Carlo simulation of mems devices, AIAA Paper 97–0375, January 1997.

[97] Nishimura, A., Ohba, H., and Shibata, T., Velocity distributions in High Density Gadolinium Atomic Beam Produced with Axial Electron-Beam Gun, *Journal of Nuclear Science and Technology*, Vol. 29, No. 11, 1992, pp. 1054–1060.

[98] Nishimura, A., Kaburaki, H., Ohba. H., and Shibata, T., Angular distribution of Gadolinium Vapor Produced by Electron-Beam Heating, *Journal of Nuclear Science and Technology*, Vol. 30, No. 3, 1993, pp. 270–273.

[99] Nishimura, A., Arisawa, T., Ohba, H., and Shibata, T., Metastable Population Densities in Gadolinium Atomic Beam at High Rate evaporation by Electron-Beam Heating, *Journal of Vacuum Science and Technology A*, Vol. 11, No. 4, 1993, pp. 1516-1521.

[100] Nishimura, A., and Shibata, T., Numerical Simulation for Metastable States Deexcitation in Electron-Beam Evaporation Process, *Journal of Nuclear Science and Technology*, Vol. 32, No. 9, 1995, pp. 905-911.

[101] Nishio, R, Tuchida, K., Tooma, M., and Suzuki, K., Origins of Charged Particles in Vapor Generated by Electron-Beam Evaporation. *Journal of Applied Physics*, Vol. 72, No. 10, 1992, pp. 4548-4555.

[102] Oh, C. K., Oran, E. S., and Cybyk, Z. B., Microchannel Flow Computed with the DSMC-MLG, AIAA Paper 95-2090, June 1995.

[103] Oh, D. and Hastings, D. E., Three Dimensional PIC–DSMC Simulations of Hall Thruster Plumes and Analysis for Realistic Spacecraft Configurations. AIAA Paper 96-3299, July 1996.

[104] Oh, D. and Hastings, D. E., Axisymmetric PIC–DSMC Simulations of SPT Plumes, IEPC Paper 95–160, September 1995.

[105] Ohring, M., *The Materials Science of Thin Films*, Academic Press, Inc., New York, 1992.

[106] Oran, E. S., Oh, C. K., and Cybyk, Z. C., Direct Simulation Monte Carlo: Recent Advances and Applications, *Annual Review of Fluid Mechanics*, Vol. 30, 1998, pp. 403–441.

[107] Ota, M. and Stafanov, S., Monte Carlo Simulation of a Low Pressure Chemical Vapour Deposition Flow., In *Rarefied Gas Dynamics*, 1996, pp. 624.

[108] Pan, L. S., Liu, G. R., and Lam, K. Y., Determination of slip coefficient for rarefied gas flows using direct simulation Monte Carlo, *Journal of Micromechanics and Microengineering*, Vol. 9, 1999, pp. 89-96.

[109] Peraire, J., Vahdati, M., Morgan, K., and Zienkiewicz, O. C., Adaptive Remeshing for Compressible Flow Computations, *Journal of Computational Physics*, Vol. 72, No. 2, 1987, pp. 449-466.

[110] Piekos, E. S., and Breuer, K. S., Numerical Modeling of Micromechanical Devices Using the Direct Simulation Monte Carlo Method, *ASME Journal of Fluids Engineering*, Vol. 118, 1996, pp. 464-469.

[111] Pimpinelli, A., and Peyla, P., Deposition and Growth with Desorption in Molecular-Beam Expitaxy, *Journal of Crystal Growth*, Vol. 183, No. 3, 1998, pp. 311–322.

[112] Piot, O., Malaurie, A., and Machet, J., Experimental and Theoretical Studies of Coating Thickness Distributions obtained from High Rate Electron Beam Evaporation Sources, *Thin Solid Films*, Vol. 293, No. 1–2, 1997, pp. 124–132.

[113] Powell, A., Van den Avyle, J., Damkroger, B., Szekely, J., and Pal, U., Analysis of Multicomponent Evaporation in Electron Beam melting and Refining of Titanium Alloys, *Metallurgical and Materials Transactions B – Process Metallurgy and Materials Processing Science*, Vol. 28, No. 6, 1997, pp. 1227–1239.

[114] Powell, C. F., Oxley, J. H., and Blocher, Jr., J. M., ed., *Vapor Deposition*, John Wiley & Sons, Inc., 1966.

[115] Radziemski, L. J., Solarz, R. W., and Paisner, J. A., ed., *Laser Spectroscopy and its Applications*, Marcel Drekker, Inc., 1987.

[116] Rebrov, A. K., and Skovorodko, P. A., An Improved Sampling Procedure in the DSMC Method, *Proceedings of the 20th International Symposium on Rarefied Gas Dynamics*, 1996.

[117] Ruyten, W. M., Density-Conserving Shape Factors for Particle Simulations in Cylindrical and Spherical Coordinates, *Journal of Computational Physics*, Vol. 105, 1993, pp. 224–232.

[118] Schiller, S., Heisig, U. and Panzer, S., *Electron Beam Technology*, John Wiley & Sons, Inc., 1982.

[119] Smith, Jr., H. R., Kennedy, K., and Boericke, F. S., Metallurgical Characteristics of Titanium Alloy Foil Prepared by Electron Beam Evaporation, *Journal of Vacuum Science and Technology*, Vol. 7, No. 6, 1970, pp. 48–51.

[120] Sugar, J., and Corliss, C., newblock *Journal of Physical Chemistry Reference Data*, Vol. 14, Suppl. 2, 1985.

[121] Sytsko, Y. I., and Yakovlenko, S. I., Simulation of Electron–Beam Heating of a Metal for Laser Isotope Separation, *Laser Physics*, Vol. 6, No. 5, 1996, pp. 989–996.

[122] Thompson, J. F., National grid project, Computing Systems in Engineering, 3, No. 1–4, 1992.

[123] Tooma, M., Ueno, M., Kobayashi, K., Tsuchida, K., and Suzuki, K., Reduction of Charge Transfer Loss in Atomic Laser Isotope Separation by Production of Excited Ions through Autoionization Levels, *Journal of Nuclear Science and Technology*, Vol. 33, No. 7, 1996, pp. 582–591.

[124] Uetake, N., Asano, T., and Suzuki, K., Measurement of Vaporized Atom Flux and Velocity in a aVacuum Using a Microbalance, *Review of Scientific Instruments*, Vol. 62, No. 8, 1991, pp. 1942–1946.

[125] VanGilder, D. B. Numeric Simulations of the Plumes of Electric Propulsion Thrusters, Ph. D. thesis, Cornell University, January 2000.

[126] VanGilder, D. B., Font, G. I., and Boyd, I. D., Hybrid Monte Carlo–Particle-in-Cell Simulation of an Ion Thruster Plume, *Journal of Propulsion and Power*, Vol. 15, No. 4, 1999, pp. 530–538.

[127] Vincenti, W. G., Kruger, Jr., C. H., *Introduction to Physical Gas Dynamics*, John Wiley & Sons, Inc., 1965.

[128] Vogenitz, F. W., Bird, G. A., Broadwell, J. E. and Rungaldier, H., Theoretical and Experimental Study of Rarefied Supersonic Flows about Several Simple Shapes, *AIAA Journal*, Vol. 6, No. 12, pp. 2388–2394.

[129] Vossen, J. L., and Kern, W., ed. *Thin Film Processes*, Academic Press, New York, 1978.

[130] Vossen, J. L., and Kern, W., ed. *Thin Film Processes II*, Academic Press, San Diego, 1991.

[131] Walther, H., ed. *Laser Spectroscopy of Atoms and Molecules*, Springer-Verlag, 1976.

[132] Wang, W., Hammond, R. H., Fejer, M. M., and Beasley, M. R., Atomic Flux Measurement by Diode–Laser-Based Atomic Absorption Spectroscopy, *Journal of Vacuum Science and Technology A*, Vol. 17, No. 5, pp. 2676–2684.

[133] Williams, F., On Vaporization of Mists by Radiation, *International Journal of Heat and Mass Transfer*, Vol. 8, 1965, pp. 575-587.

[134] Wolf, S., and Tauber, R. N., *Silicon Processing for the VLSI Era, Vol. 1 – Process Technology*, Lattice Press, Sunset Beach, CA, 1986.

[135] Yang, Y., Johnson, R. A., and Wadley, H. N. G., A Monte Carlo Simulation of the Physical Vapor Deposition of Nickel, *Acta. mater.*, Vol. 45, No. 4, 1997, pp. 1455.

[136] Zhou, X. W., Johnson, R. A., and Wadley, H. N. G., A Molecular Dynamics Study of Nickel Vapor Deposition, *Acta. mater.*, Vol. 45, No. 4, 1997, pp. 1513.